Universidad de Oviedo

Programa de Doctorado en Biomedicina y Oncología Molecular

Geroprotective and antineoplastic functions of protein homeostasis

Doctoral Thesis

Daniel Maeso Miguel

November, 2023

Universidad de Oviedo

Programa de Doctorado en Biomedicina y Oncología Molecular

Funciones geroprotectoras y antineoplásicas de la homeostasis proteica

Tesis Doctoral

Daniel Maeso Miguel

Noviembre, 2023

Universidad de Oviedo

RESUMEN DEL CONTENIDO DE TESIS DOCTORAL

1.- Título de la Tesis	
Español/Otro Idioma: Funciones geroprotectoras y antineoplásicas de la homeostasis proteica	**Inglés:** Geroprotective and antineoplastic functions of protein homeostasis

2.- Autor	
Nombre: Daniel Maeso Miguel	**DNI/Pasaporte/NIE:**
Programa de Doctorado: Programa Oficial de Doctorado en Biomedicina y Oncología Molecular	
Órgano responsable: Centro Internacional de Postgrado	

RESUMEN (en español)

La homeostasis proteica, o proteostasis, comprende una compleja red molecular encargada de mantener la estabilidad del proteoma, controlando la conformación, localización y concentración de proteínas dentro de las células. Su alteración afecta al correcto funcionamiento de las células y está vinculada a diversos procesos fisiológicos y patológicos, como el cáncer. Su relevancia es tal que se ha identificado como uno de los nueve *hallmarks* del envejecimiento, así como un *hallmark* de la salud. En la presente Tesis Doctoral, hemos explorado las funciones geroprotectoras y antineoplásicas de la homeostasis proteica mediante la generación de dos nuevos modelos animales.

El primer modelo animal es deficiente en dos factores de proteostasis asociados con la degradación de proteínas a través del proteasoma: AIRAPL y AIRAP. Se sabe que los ratones deficientes en AIRAPL desarrollan neoplasias mieloproliferativas debido a la desregulación de la vía de señalización de la insulina/IGF-1. Sin embargo, la deficiencia en AIRAP por sí sola no parece producir ningún fenotipo aparente. En este trabajo hemos generado un nuevo modelo murino deficiente en ambos factores, AIRAPL y AIRAP, lo que ha llevado al descubrimiento de que la pérdida simultánea de AIRAPL y AIRAP exacerba el proceso de neoplasia mieloide.

El segundo modelo animal desarrollado es deficiente en la principal proteína descrita como encargada del transporte de ARNs de transferencia (ARNt) desde el núcleo hasta el citoplasma: Exportina-t (XPOT). Mientras que la ausencia de su gen ortólogo, Losp1, en *Saccharomyces cerevisiae* extiende de manera significativa su esperanza de vida mediante la acumulación de ARNts dentro del núcleo, sorprendentemente, en nuestro modelo hemos observado todo lo contrario. Los ratones deficientes en *Xpot* presentan una reducción considerable de su esperanza de vida, y no hemos encontrado retención de ARNts en los núcleos de sus células. A pesar de ser fértiles en heterocigosis, el porcentaje de ratones que llegan a nacer con la deficiencia completa de *Xpot* es mucho menor de lo esperado. Este modelo de ratón se caracteriza por presentar un fenotipo más débil, que incluye un desarrollo anormal de la hematopoyesis tanto en la etapa adulta como embrionaria, además de ciertas alteraciones metabólicas. Nuestros resultados cuestionan el papel de Xpot en el transporte núcleo –citoplama de tRNAs y ponen de manifiesto su importancia en el correcto desarrollo del organismo, especialmente del compartimento hematopoyético, y su posible papel en cáncer y el envejecimiento.

RESUMEN (en Inglés)

Universidad de Oviedo

Protein homeostasis, or proteostasis, is a complex cellular self-regulation network that maintains the stability of the proteome, controlling the conformation, localization, and concentration of proteins within cells. Disruption of proteostasis impairs proper cellular function and is implicated in various physiological and pathological processes including cancer. Its significance is further emphasized as one of the nine hallmarks of aging and as a hallmark of health. In the Doctoral Thesis, we have undertaken an exploration of the geroprotective and antineoplastic functions of protein homeostasis trough the generation of two new animal models.

The first animal model under study is deficient in two proteostasis factors associated with protein degradation through the proteasome: AIRAPL and AIRAP. It is known that AIRAPL deficient mice develop myeloproliferative neoplastic processes due to dysregulation of the insulin/IGF-1 signaling pathway. However, the deficiency in AIRAP alone does not appear to produce any noticeable phenotype. In this work we have generated a mouse model deficient in both AIRAPL and AIRAP, leading to the discovery of an exacerbated myeloid neoplastic process when both proteostasis factors are lacking.

The second animal model under investigation is deficient in the principal protein responsible for translocating transfer RNAs (tRNAs) from the nucleus to the cytoplasm, Exportin-t (XPOT). While the absence of the orthologous gene, Losp1, in *Saccharomyces cerevisiae* significantly extends its lifespan through an accumulation of tRNAs within the nucleus, intriguingly, we found the opposite effect in mice. XPOT deficient mice exhibit a significantly shorter lifespan, and no tRNA retention in cell nuclei was found. Despite being fertile in heterozygosis, the percentage of born *Xpot* null mice is much lower than expected. This mouse model exhibits a milder phenotype, marked by abnormal hematopoiesis development in both adult and embryonic stages, along with specific metabolic alterations. Our findings raise questions about the role of Xpot in nucleo-cytoplasmic tRNA transport and emphasizes its significance in proper organismal development, particularly on the hematopoietic compartment. Finally, in this thesis, we have explored the impact of Xpot loss within the contexts of both cancer and aging.

SR. PRESIDENTE DE LA COMISIÓN ACADÉMICA DEL PROGRAMA DE DOCTORADO EN BIOMEDICINA Y ONCOLOGÍA MOLECULAR

ABBREVIATIONS

AARS	aminoacyl tRNA synthetase
aa-tRNAs	aminoacylated tRNA
AIP-1	arsenite-inducible protein 1
AIRAP	arsenic-inducible proteasomal 19s regulatory particle-associated protein
AIRAPL	AIRAP-like
ALS	amyotrophic lateral sclerosis
AML	acute myeloid leukemia
ARE	AU-rich elements
ATF6 α	activating transcription factor 6
c-Cbl	casitas B-cell lymphoma
CDK	cyclin-dependent kinase
CEL-NOS	chronic eosinophilic leukemia
CLP	common lymphoid progenitor
CMA	chaperone-mediated autophagy
CML	chronic myeloid leukemia
CMoP	common monocyte progenitor
CMP	common myeloid progenitor
CNL	chronic neutrophilic leukemia
CRM1	chromosomal region maintenance 1
E1	enzyme cascade involving ubiquitin-activating enzyme
E2	ubiquitin-conjugating enzyme
E3	ubiquitin ligase enzyme
EF1A	elongation factor 1a
ER	endoplasmatic reticulum
ERAD	ER-associated degradation
ET	essential thrombocythemia
FG	phenylalanine-glycine
FG-Nup	phenylalanine-glycine nucleoporin
FSC	forward side scatter
GDP	guanosine diphosphate
GMP	granulocyte-monocyte progenitor
GTP	guanosine triphosphate
HSC	hematopoietic stem cell
HSP	heat-shock protein
IGF-1R	insulin growth factor–1 receptor

INM	inner nuclear membrane
IRE1 α	inositol-requiring enzyme 1
Kap	karyopherin
kDa	kilodalton
LSK	Lin^{-} $Sca1^{+}$ $cKit^{+}$
LT-HSCs	long-term repopulating HSCs
MDa	megadalton
MDP	macrophage and dendritic cell progenitor
MEP	megakaryocyte-erythrocyte progenitor
miRNA	microRNA
MK	megakaryocite
MPN	myeloproliferative neoplasm
MPN-U	MPN unclasificable
MPP	multipotent progenitor
mRNA	messenger RNA
mRNP	ribonucleoprotein complexes
NE	nuclear envelope
NES	nuclear export signal
NK	natural killer
NK cells	natural killer cells
NLS	nuclear localization signal
NPC	nuclear pore complex
nt	nucleotide
NTR	nuclear transport receptor
Nup	nucleoporin
ONM	outer nuclear membrane
PERK	protein kinase R-like endoplasmic reticulum kinase
PMF	primary myelofibrosis
pol	polymerase
pre-miRNA	precursor of miRNA
pre-mRNA	precursor of mRNA
pre-rRNA	precursor of rRNA
pre-snRNA	precursor of snRNA
pre-tRNA	precursor of tRNA
PV	polycythemia vera
RANBP1	Ran-binding protein
RANGAP	RAN-GTPase activating protein
RLS	replicative lifespan
rRNA	ribosomal RNA
RT-qPCR	real time quantitative PCR
snRNA	spliceosomal small nuclear RNA
SSC	side scatter
ST-HSCs	short-term repopulating HSCs
TAP	transporter associated with antigen processing

TPR	translocated protein region
TREX	transcription-export complex
Trn	transportin
tRNA	transfer RNA
TSEN	tRNA splicing endonuclease
UIM	ubiquitin-interacting motifs
UPR	unfolded protein response
UPS	ubiquitin proetasome system
UTR	untranslated regions
WHO	World Health Organization

CONTENTS

INTRODUCTION

"The coordinated physiological processes which maintain most of the steady states in the organism are so complex and so peculiar to living beings […], that I have suggested a special designation for these states, homeostasis. The word does not imply something set and immobile, a stagnation. It means a condition – a condition which may vary, but which is relatively constant".

This is how in 1926, the physiologist Walter Bradford Cannon, combining two words from ancient Greek (hómos, "similar") and (stásis, "stability") coined the term "*homeostasis"*. Cannon extended the concept of *milieu intérieur* from Claude Bernard [1], who is considered the father of modern experimental physiology, and popularized it in his highly successful and persuasive book, "*The Wisdom of the body"* [2].

Homeostasis and health

The numerous functions of the human body, beginning at the cellular level, operate harmoniously to maintain a delicate internal equilibrium. This dynamic balance ensures stability and is orchestrated in a hierarchical manner, extending from the smallest cellular molecules to tissues, organs, and systems. As a result, it maintains the stability and health of the human body. Homeostasis would not be possible without set points, feedback, and regulation. The human body comprises thousands of control systems to detect alterations induced by external disruptors and activate effectors to mediate those changes. Our organism's inherent ability to acclimate to a constantly changing environment is referred to as allostasis. Deterioration of any of these regulatory systems compromises stability, which, in turn, can lead to health issues and diseases [3].

The concept of health and disease is a complex notion that, throughout history, has undergone a nuanced evolution, intertwining cultural, philosophical, and medical dimensions. In antiquity, various civilizations, including the Greeks, Romans, Chinese, and Hindus, elucidated health as equilibrium and well-being, while considering disease as its opposite. The Greek physician Hippocrates of Cos (460 – 377 ca.), renowned as the father of Western medicine, considered health as the balance of four bodily fluids, known as humors, with disease arising from their imbalance. During the Renaissance, the physician Paracelsus (1493-1541) linked health to the harmonious relationship between the human microcosm and the universal macrocosm, attributing disease to diverse entities. In the Enlightenment, clinician Giovanni Battista Morgagni (1682-1771) emphasized clinical-anatomical integrity for health and anatomical changes for disease. Claude Bernard viewed health and disease as interconnected on a spectrum in the 19th century, and the 20th century witnessed a molecular shift in medicine. This shift was coupled with a renewed global focus on human beings, both healthy and sick, resulting in the emergence of a synergistic and multi-faceted definition of health [4].

Nowadays, according to the first principle of the constitution of the World Health Organization (WHO), we can define health as *a state of complete physical, mental, and social well-being, and not merely the absence of disease or infirmity* [5]. This classical definition of health is considered a historical and fundamental milestone in Western medicine, aligning with the definition proposed by the Hippocratic School. However, in an endeavor to gain deeper insight into the intricate array of events and pathways working collectively to preserve the delicate equilibrium intrinsic to the human body's homeostasis, and with the aim of explaining the concept of health in positive terms, eight Hallmarks of Health have been proposed [6]. These hallmarks define health as a compendium of organizational and dynamic features that maintain physiology. Following the preceding hallmarks of cancer and aging [7,8], the hallmarks of health are not merely indicators of vigor but are actively implicated in the preservation of its homeostatic maintenance. These biological causes are divided into three categories: spatial compartmentalization, maintenance of homeostasis, and responses to stress.

The first category involves ensuring the *integrity of barriers* that delimit cells and enable proper interconnections between systems, preventing the spread of disruptions to higher levels. The second category, related to the maintenance of homeostasis, includes: the *recycling and turnover* of proteins to maintain protein homeostasis; the *integration of circuits* within and between levels of organization; and the *rhythmic oscillations*, such as the control of the circadian clock, stem cell regulation, and the management of mitochondria, the immune system, and microbiota. In the third group, we find the hallmark of *homeostatic resilience*, which pertains to the control of various biological parameters such as blood pH, serum osmolarity, and body temperature. Additionally, *hormetic regulation* manages toxin concentrations, where low doses are protective while higher doses have adverse effects. The final hallmark, *repair and regeneration*, encompasses all the pathways involved in cellular reconstitution and integration, facilitating the repair of potential damages.

During aging, these biological processes progressively deteriorate. Spatial compartmentalization ability decreases, compromising the integrity of internal and external barriers. The capacity to contain disruptions within these barriers diminishes both in space and time. Maintaining homeostasis over time becomes less efficient, leading to reduced recycling and turnover, inefficient coordination among different systems via integrated circuits, and desynchronization of circadian, ultradian, or infradian rhythms. The ability to respond effectively to stress also declines with age, resulting in reduced homeostatic resilience, hormetic regulation, and the pathways for repair and regeneration. The disruption of one or more of the hallmarks of health results in the loss of health and the onset of disease. Typically, they do not deteriorate one by one; instead, their decline occurs in a domino-like cascade, where the decay of one lead to the collapse of others. During tumor development, these hallmarks are compromised. For instance, maintaining homeostasis is disrupted due to the aberrant proliferative capacity of cancer cells, resulting in excessive protein synthesis, which impairs proteostasis. In several cancer types, the responses to repair and regenerate damaged cells are also altered.

Proteostasis as a determinant of health

The importance of protein homeostasis

Protein homeostasis, or proteostasis, is a complex cellular self-regulation network that maintains the stability of the proteome, controlling the conformation, localization, and concentration of proteins within cells. Disruption of proteostasis impairs proper cellular function and is implicated in multiple physiological and pathological processes. Its importance is highlighted as one of the nine hallmarks of aging and as a hallmark of health. Molecular perturbations in proteostasis have been identified in the pathogenesis of notable conditions such as Alzheimer's disease, Parkinson's disease, and several tumors [6,8]. The extensive proteostasis network, consisting of around 800 proteins, comprises three main components: molecular chaperones and two proteolytic systems—the ubiquitin-proteasome and the lysosome-autophagy systems. These components determine the fate of unfolded proteins, deciding whether they will refold into their original stable conformation or be eliminated from the cell through proteolysis [9]. Besides these systems, certain organelles exhibit different responses to the loss of proteostasis, with the endoplasmic reticulum (ER) playing an important role. Moreover, various studies indicate the existence of well-regulated systemic proteostasis networks beyond the cell-autonomous ones already established [10–12].

Chaperones

Chaperones assist proteins through various conformational changes in their lifetime, including *de novo* folding, assembly and disassembly, membrane transport, and targeting for degradation. The need for chaperones arises from the crowded environment in both the cytoplasm and organelle lumens. These assistant molecules integrate multiple cellular signals to determine whether a misfolded protein is refolded or degraded based on feasibility and cellular conditions [13].

Chaperones are categorized into various groups that work together in coordinated pathways, with many being denominated as heat-shock proteins (HSPs) due to their upregulation under stress conditions. Age-related changes impact chaperone activity, contributing to the loss of proteostasis during aging. Deficiencies in chaperone molecules have been associated with several age-related disorders, particularly neurodegenerative pathologies [14]. Besides, studies in different model organisms have shown that an elevation in chaperone activity can lead to an extension in longevity. For instance, overexpression of HSP16 has been found to increase lifespan and improve stress resistance in *Caenorhabditis elegans* [15]. Chaperones also play a pivotal role in tumor development [16]. Numerous HSPs, such as HSP60, HSP70, and HSP90, have been reported to be overexpressed in various cancers, associated to poor patient prognosis [17,18].

Autophagy-lysosomal system

The primary function of autophagy is to provide nutrients for vital cellular functions during fasting and other forms of stress. More recently, autophagy has been shown to selectively eliminate undesired, potentially harmful cytosolic material, including damaged organelles, misfolded proteins, or aggregates. In this way, the autophagy-lysosomal system plays a critical role in maintaining proteostasis. There are three types of autophagy based on the mechanism of identifying and transporting proteins to lysosomes: *microautophagy*, where components are degraded by the invagination of the lysosome membrane; *macroautophagy*, where autophagosomes (including large portions of cytoplasm surrounding the substrate for degradation) fuse with lysosomes; and *chaperone-mediated autophagy* (CMA), which selectively degrades specific proteins recognized by the molecular chaperone HSC70 and then translocate them to the lysosome through the membrane receptor LAMP2A [19,20].

During aging, autophagy tends to decline, disrupting proteostasis. Its promotion has been associated with increased longevity in humans and mice [21]. As a proteolytic system, autophagy is tightly linked to cancer development and progression. On one hand, it plays a role in promoting cancer cell survival and growth in advanced stages by providing substrates such as amino acids for metabolism through the intracellular recycling of damaged proteins. Furthermore, it contributes to reducing the levels of certain proteins with tumor-suppressing functions [16,22]. On the other hand, autophagy is also considered a tumor suppressor mechanism in the early stages of tumorigenesis, as it can inhibit tumors by removing oncogenic protein substrates, toxic unfolded proteins, and damaged organelles, thereby maintaining protein homeostasis and genomic stability[23].

Ubiquitin proteasome system

The Ubiquitin Proteasome System (UPS) serves as the primary cellular mechanism for protein degradation, playing a vital role in maintaining proteostasis. Approximately 80% of cellular proteins can be degraded by the UPS [24]. This degradation system requires the conjugation of ubiquitin, a small and highly conserved protein consisting of 76 amino acids. This conjugation is mediated by an enzyme cascade involving a ubiquitin-activating enzyme (E1), a ubiquitin-conjugating enzyme (E2), and a ubiquitin ligase (E3), which sequentially transfer ubiquitin molecules to cellular targets [25]. Subsequently, the proteolytic core of the proteasome degrades the tagged proteins in an ATP-dependent manner, recycling the resulting amino acids for *de novo* protein synthesis.

The proteasome is a cylindrical protein complex consisting of multiple subunits. These subunits are often referred to by their Svedberg sedimentation coefficient, with the mammal's proteasome known as the 26S proteasome. The core of this structure, known as the 20S subunit, is composed of several proteases that cleave proteins into smaller fragments. The two ends of the cylinder, the 19S regulatory subunits, contain multiple

ATPase active sites and ubiquitin binding sites that recognize polyubiquitinated proteins and transfer them to the catalytic core [26].

The UPS does not solely target aggregated, misfolded, or damaged proteins. This system also controls the levels of non-defective proteins, regulating a wide variety of cellular processes. For example, it plays a role in the processing of antigens for presentation to the immune system. As a result, alterations in the UPS have been associated with multiple disorders [24,27,28]. During aging, the function of the UPS diminishes, leading to an increased accumulation of misfolded proteins in different tissues [29]. In the case of cancer cells, the UPS plays a crucial role. Due to their exacerbated proliferative capacity, these cells undergo extensive protein synthesis, resulting in a significant accumulation of newly synthesized defective proteins that are targeted for elimination by the UPS. The massive accumulation of misfolded proteins triggers cell death through apoptosis. As a result, proteasome inhibitors are being used in the treatment of various types of tumors. For example, carfilzomib and bortezomib are being used in the treatment of multiple myeloma [30,31].

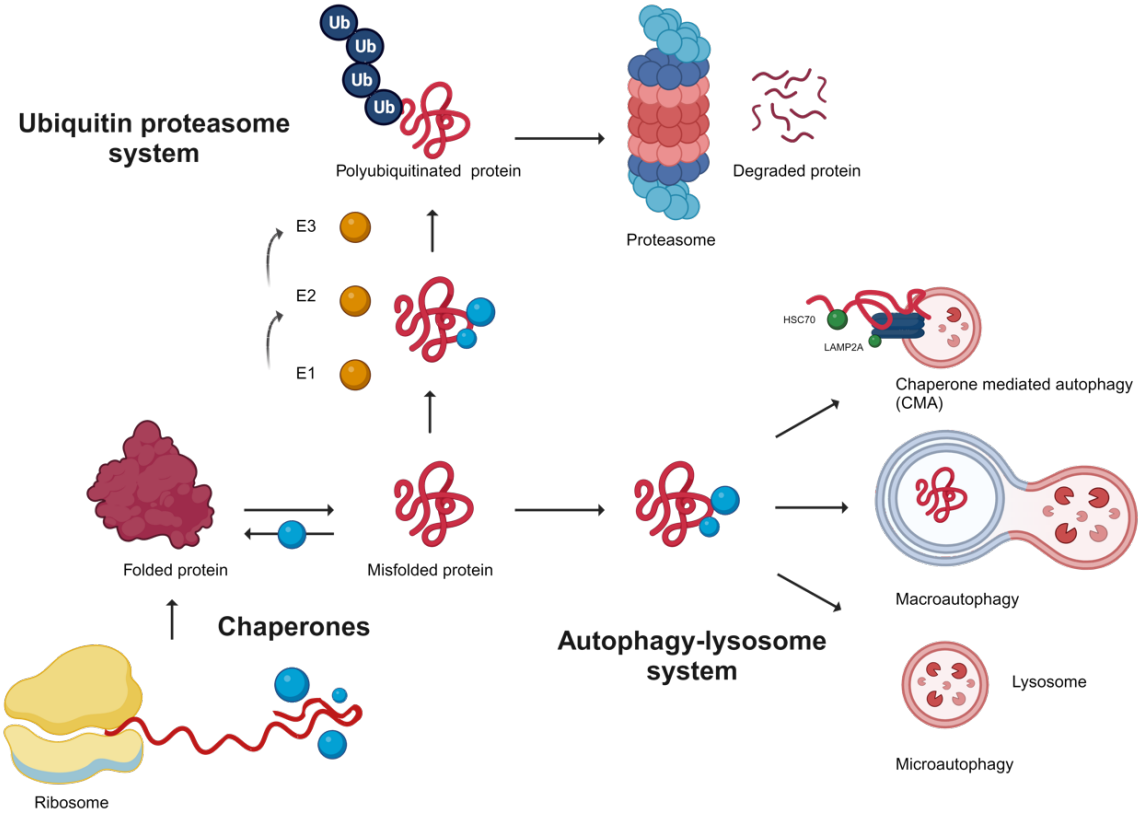

Figure 1. Foundations of proteostasis. Chaperones (blue balls), autophagy-lysosome system and ubiquitin-proteasome system as responsible for the maintenance of proteostasis are represented.

Proteostasis in the Endoplasmic Reticulum

In addition to playing a pivotal role in protein synthesis, the ER also plays crucial roles in protein homeostasis by controlling the processing and folding of secreted and membrane proteins. Disruption of the ER's protein-folding capacity leads to the accumulation of unfolded and misfolded proteins, causing perturbations in ER homeostasis referred to as ER stress [32]. Adaptive mechanisms, including the unfolded protein response (UPR), ER-associated degradation (ERAD), and reticulophagy (a specific type of autophagy), are activated to counteract elevated ER stress [33].

The UPR signaling pathway attempts to restore proteostasis through three ER transmembrane proteins, commonly referred to as UPR branches or sensors: protein kinase R-like endoplasmic reticulum kinase (PERK), inositol-requiring enzyme 1 (IRE1α), and activating transcription factor 6 (ATF6α), linked to the BiP chaperone. These sensors initiate a cascade of molecular interactions that culminate in increasing the folding capacity by inducing transcriptional changes [34,35].

The ERAD system is responsible for clearing misfolded proteins from the ER lumen for cytosolic proteasomal degradation when the UPR pathway fails [36]. Additionally, the network of sacs and cisterns that make up the endoplasmic reticulum can undergo remodeling and selective recycling through a specific form of autophagy known as reticulophagy. This process helps to reduce the levels of newly synthesized proteins during ER stress situations. Prolonged ER stress can lead to inflammatory signaling, while unmitigated and excessive stress can result in apoptosis[37]. During aging, there is a tendency to develop persistent ER stress, often accompanied by an altered response to unfolded proteins. The UPR has been implicated in abnormal protein processing and neuronal death in age-associated diseases, playing a triggering role in neurodegenerative diseases. Additionally, conditions such as atherosclerosis and type II diabetes highlight the important role of ER stress.

In the field of cancer, ER stress and the UPR are robustly upregulated in various tumor types and are closely associated with cancer cell survival and their resistance to anti-cancer treatments. In several tumor types, a combination of oncogenic, transcriptional, and metabolic abnormalities collaboratively creates hostile microenvironments, disrupting ER homeostasis in both malignant and stromal cells. These alterations induce a prolonged state of ER stress, which has been demonstrated to govern multiple pro-tumoral characteristics in cancer cells. Interestingly, moderate levels of ER stress enhance the aggressiveness, metastatic potential, and drug resistance of tumors, suggesting that the ER could be a potential target for cancer therapy [38].

AIRAP and AIRAPL as ER proteostasis factors

Given the paramount importance of maintaining proteostasis throughout the aging process and the subsequent disruption of this balance over an individual's lifetime, numerous studies have been conducted to identify regulatory factors linked to proteostasis and aging. An example of this is the characterization of arsenite-inducible protein 1 (AIP-1) as a novel proteostasis factor essential for maintaining protein homeostasis in *C. elegans*. AIP-1 is a protein localized in the endoplasmic reticulum that interacts with the proteasome under stress conditions. AIP-1-deficient nematodes exhibit a reduced lifespan due to challenges in dealing with misfolded proteins when compared to wild-type worms [39].

Two orthologs of AIP-1 have been identified in mammals: arsenic-inducible proteasomal 19s regulatory particle-associated protein (AIRAP) and AIRAP-like (AIRAPL). The discovery of the first ortholog, AIRAP, was made in 2001 by Professor David Ron while studying the molecular pathways activated by exposure to arsenicals in cells [40]. This finding not only provided the name for AIP-1 in *C. elegans* but also led to the identification of its ortholog, AIRAPL, by his research group seven years later[39].

Both proteins, AIRAP (encoded by *ZFAND2A*) and AIRAPL (encoded by *ZFAND2B*), are involved in maintaining proteostasis through the UPS by promoting substrate access to the 26S proteasome, thanks to their affinity with the 19S subunit [41]. However, they differ in their regulation mechanisms. Whereas AIRAP is up-regulated transcriptionally by different stressors (e.g., arsenite exposure), AIRAPL is constitutively expressed, and its association with proteasomes is regulated posttranslationally. Structurally, they show a 60% identity in their proteasome-binding N-terminal domain but diverge at the C-terminal domain. Both mammalian AIRAPL and worm AIP-1 have conserved, functional ubiquitin-interacting motifs (UIMs), and both proteins possess a conserved CaaX motif for farnesylation. These features are missing in AIRAP and may be key to preserving lifespan [39].

Interestingly, recent studies conducted in our laboratory have established AIRAPL as a significant proteostasis factor implicated in the development of myeloproliferative neoplasms (MPN) [42]. Mice deficient in *AIRAPL* develop cell-autonomous alterations in the hematopoietic stem cell (HSC) compartment, ultimately culminating in a myeloproliferative neoplastic process. Proteomic analysis from this new animal model has determined that AIRAPL interacts with the newly synthesized insulin growth factor-1 receptor (IGF1R) in the endoplasmic reticulum, leading to its degradation via the UPS (**Figure 2)** [43]. Pharmacological and genetic inhibition of this receptor in *AIRAPL*-deficient mice rescues the malignant phenotype in HSC. Furthermore, AIRAPL was found to be downregulated in patients with myeloproliferative syndromes as a result of microRNA miR-125a-3p overexpression. In contrast, mice deficient in *AIRAP* apparently do not develop any hematological phenotype, possibly due to the presence of its ortholog,

AIRAPL. The development of a mouse model deficient in both proteostasis factors is a subject of study in the present doctoral thesis.

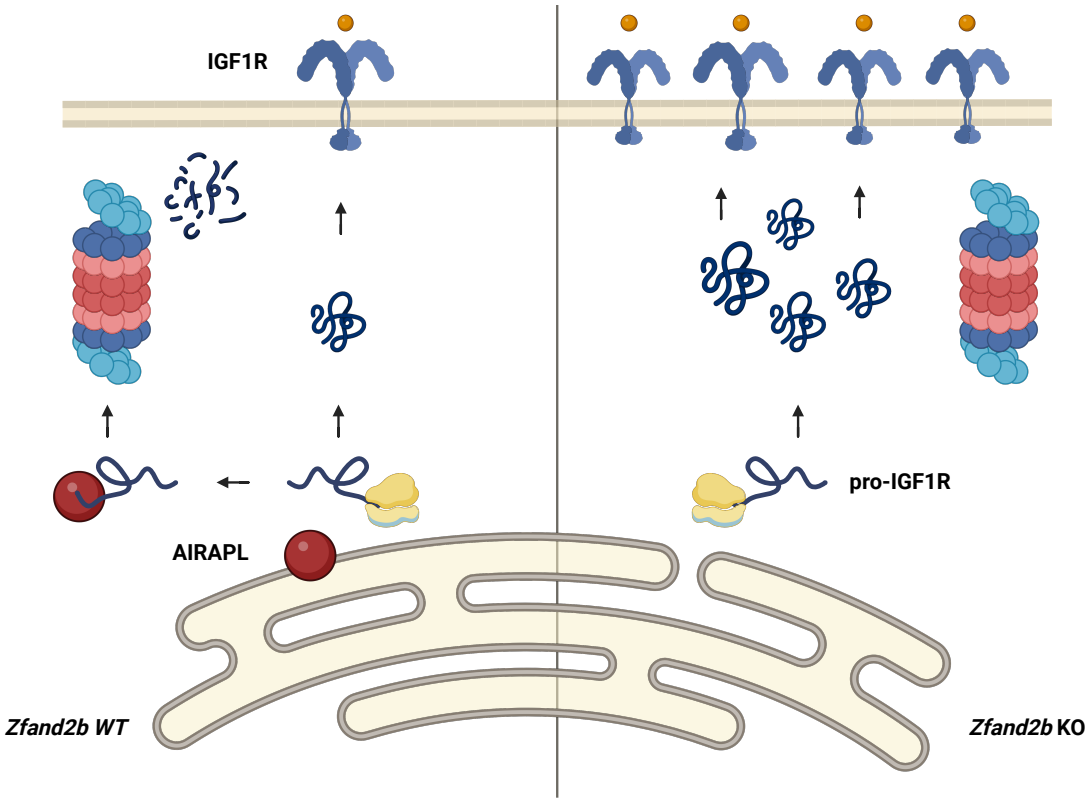

Figure 2. IGF1R in a *Zfand2b* wild type cell and *Zfand2b* KO cell. AIRAPL interacts with newly synthesized pro-IGF1R polypeptides at the ER (left part of the figure), inducing their ubiquitination and proteasome-mediated degradation. In the absence of AIRAPL (right part of the figure), the lack of this regulatory mechanisms increases IGF1R steady-state levels, promoting insulin/IGF1 signaling deregulation. ER is represented in yellow in the bottom part of the figure and the lipid membrane is represented in the top. Figure adapted from [43]

Importance of proteostasis in hematological development

The critical significance of maintaining proteostasis is particularly evident in hematopoietic cells, which undergo a rapid and profound functional remodeling during differentiation. HSC give rise to many thousands of mature blood cells while also self-renewing to maintain the HSC pool. During differentiation, a lineage divergence occurs between two common progenitors: myeloid and lymphoid. On one hand, the primitive myeloid progenitor is responsible for the production of erythrocytes, megakaryocytes (which give rise to platelets), granulocytes (eosinophils, basophils, and neutrophils), monocytes/macrophages and dendritic cells. On the other hand, the primitive lymphoid progenitor is responsible for the production of lymphocytes, including B cells, T cells and natural killer (NK) cells.

To finally result in all these different cell types, the complex network that maintains protein homeostasis must be finely controlled and regulated. Malignancies within the

hematopoietic system often arise due to the loss of HSC proteostasis [44]. One example is the deletion of the Casitas B-cell Lymphoma (*c-Cbl*) gene in mice, which encodes an E3 ubiquitin ligase. The deficiency in this gene leads to abnormal hematopoiesis, with an increase in HSCs but no elevation in mature cell output [45]. The maintenance of protein homeostasis is of such critical importance in immune cells that the loss of proteostasis has recently been recognized as a hallmark of T cell aging [46].

As previously mentioned, the loss of the proteostatis factor AIRAPL has been associated with the development of MPNs. Likewise, the ER chaperone calreticulin, which functions as a calcium sensor and modulator of protein folding quality control pathways, plays an important role also in the generation of these myeloid tumors. MPNs comprise a group of chronic myeloid tumors characterized by the overproduction of mature blood cells through transformation of a multipotent hematopoietic progenitor[47]. This type of neoplasms enlists several subcategories, including essential thrombocythemia (ET), polycythemia vera (PV), primary myelofibrosis (PMF), MPN unclassifiable (MPN-U), chronic myeloid leukemia (CML), chronic neutrophilic leukemia (CNL) and chronic eosinophilic leukemia not otherwise specified (CEL-NOS) In the long term, all of them may evolve into acute myeloid leukemia (AML), a severe complication of these disorders [48].

Physiologic and pathologic implications of nucleocytoplasmatic transport

According to the Central Dogma of molecular biology, genetic information flows from DNA to messenger RNA molecules, ultimately leading to the synthesis of a protein in the ribosomes. This transmission of information starts within the nucleus, where DNA is safeguarded from the rest of the cell by the double membrane forming the nuclear envelope. It then proceeds to the cytoplasm, where ribosomes carry out protein synthesis. This seemingly simple process involves multiple sets of proteins and RNAs. Overseeing and controlling every step, from DNA replication to the elongation and conformation of the polypeptide chain within the major subunit of the ribosomes, is as complex as it is important. If any of these components were to deteriorate, homeostasis would be compromised, leading to the activation of additional checkpoints to restore it.

Here, we will discuss the significance of the traffic between nucleoplasm and cytoplasm, with particular attention given to the molecules responsible for decoding the genetic code, the transfer RNAs (tRNAs), and their principal transporter, exportin-t (XPOT).

The nuclear membrane as a barrier between the nucleus and the cytoplasm

Due to its significant size, the nucleus was the first organelle to be discovered. Antonie Van Leeuwenhoek (1632-1723) was the first to observe the presence of a rounded structure inside salmon erythrocytes under the microscope. However, it was not until 1831 that it was officially named the "nucleus" by Robert Brown. It was only during the twentieth century that electron microscopy allowed for a precise description of the nuclear envelope (NE) [49,50].

The NE is composed of inner and outer membranes (INM and ONM, respectively) separated by a 20-50 nm wide perinuclear space. More than just an inert separation between the inside and outside of the nucleus, the NE plays an active role, serving as a hub for a diversity of genomic processes, such as transcription, DNA repair, and chromatin dynamics[51]. The communication between the inside and the outside of the nucleus is facilitated by Nuclear Pore Complexes (NPCs) that traverse both membranes, serving as channels for the import or export of proteins and nucleic acids. The number of NPCs around the envelope varies, with approximately 100 in yeast and up to 2000 in human nuclei. This number is cell cycle-regulated by cyclin-dependent kinases (CDKs) [52]. NPCs have a conserved structure consisting of several elements (**Figure 3**): The inner pore ring, located at the fused inner and outer nuclear membranes; the nuclear and cytoplasmic rings, anchored by the pore ring; and the nuclear basket and the cytosolic

filaments, which are peripheral elements emanating from the nuclear and cytoplasmic rings [53].

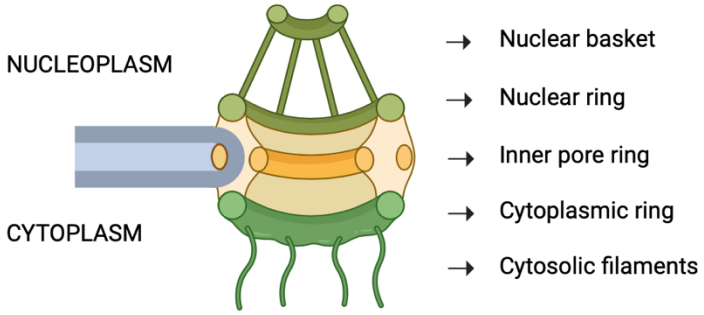

Figure 3. Nuclear Pore Complex Structure. NPC is represented anchored into the NE. Nuclear basket and nuclear ring belongs to the nucleoplasm part of the cell and the cytoplasmic rings and cytosolic filaments to the cytoplasm. Troughing the NE the inner pore ring in yellow is represented.

In higher eukaryotes, this transmembrane complex boasts an impressive size of approximately 120 Megadaltons (MDa), in stark contrast to, for example, ribosomes with a molecular mass of around 3.5 MDa. NPCs are assembled from multiple copies, ranging from 8 to 64 of around 30 different nuclear pore proteins known as nucleoporins (Nups). Determining the structure and number of copies of nucleoporins per NPC remains an active area of research [54]. Some Nups located within the channel possess a distinctive domain characterized by a random secondary structure, known as the phenylalanine-glycine (FG) repeat domain. FG Nups create a permeability barrier for nuclear transport, essentially acting as a checkpoint. They allow free passage for small proteins (< 40 kDa) while selectively restricting larger cargos, which require an active transport mechanism[55].

The disruption of NPCs involved in nucleocytoplasmic transport has been associated with aging and a wide spectrum of diseases, particularly neurodegenerative disorders. For example, the deficiency of the cytoplasmic filamentous protein Nup358, or Ranbp2, known for its role in oxidative stress response, leads to an amyotrophic lateral sclerosis (ALS) phenotype when absent in the motor neurons of homozygous mice [56]. Furthermore, its ubiquitous deficiency in heterozygosis exacerbates the severity of Parkinson's Disease when exposed to neurotoxins [57]. Interestingly, most Nup homozygous knockout mice reported so far either die during embryogenesis or shortly after birth. Among the few specific nucleoporin-null mice that do survive early development, some are sterile, while others exhibit phenotypes that lead to a shortened lifespan. Even mice with reduced levels of nuclear pore components often have serious health problems [58].

Trafficking between the nuclear membrane

Short after the discovery of NPCs, it was believed that they were passive structures that allowed the diffusion of molecules between the cytoplasm and nucleus, with a constant nucleoporin composition across cells [59,60]. Nowadays, it is known that these highly complex structures are diverse and play a role not only in passive transport but also in active, energy-dependent trafficking [61,62]

The general paradigm for nucleocytoplasmic transport was established through the analysis of protein import into and export from the nucleus. These studies revealed that active transport through NPCs requires a family of conserved soluble nuclear transport receptors (NTR) known as Karyopherins (Kaps), or importin-β family members[63]. The Kap family mediates most of the macromolecule transport, especially of proteins, across the NPC. Depending on the cargo's destination, it is possible to differentiate between exportins (out of the nucleus), importins (into the nucleus), or biportins (both directions). Although the exact number of Kap family members varies in different organisms, the majority are identifiable and conserved across eukaryotes, suggesting a strong conservation of function throughout the eukaryotic kingdom [64,65].

The way NTRs perform their work is relatively simple. First, they bind their cargo on one side of the NE, then translocate to the other side through the NPC, and finally release it in the proper destination before returning to the original compartment to mediate the next round of transport. To carry out this cycle, the differential concentration of guanosine triphosphate (GTP) and guanosine diphosphate (GDP) is essential. Kaps are Ran-GTP binding proteins, which means they require the assistance of the adapter Ran, a Ras-related small GTPase that switches between a GDP-bound and GTP-bound form, to function properly [66]. Ran-GTP and Ran-GDP are asymmetrically localized between the nucleus and the cytoplasm. In the nucleus, Ran is mostly bound to GTP because a guanine nucleotide exchange factor called RCC1, which is bound to chromatin, generates Ran-GTP on this side of the NE. Meanwhile, on the other side, cytoplasmic Ran-GTPase activating protein (RANGAP) and Ran-binding protein (RANBP1) activate GTP hydrolysis, maintaining cytosolic Ran in a GDP-bound state (**Figure 4A**).

Kaps bind export cargoes and Ran-GTP cooperatively, while import cargoes and Ran-GTP are handled in a mutually exclusive manner. Thus, exportins form ternary complexes with export cargoes and Ran-GTP in the nucleus. They then translocate across NPCs to the cytosol, where they disassemble upon GTP hydrolysis (**Figure 4B**). Conversely, importins bind cargoes in the cytoplasm due to the lower GTP concentration and translocate across NPCs to the nucleus. In the nucleus, they bind Ran-GTP and release the cargoes [67] (**Figure 4C**). Both importins and exportins, while passing through

the NPC, interact with the FG-repeat domains of FG-Nups through low-affinity interactions, which allow their movement inside the pore [68].

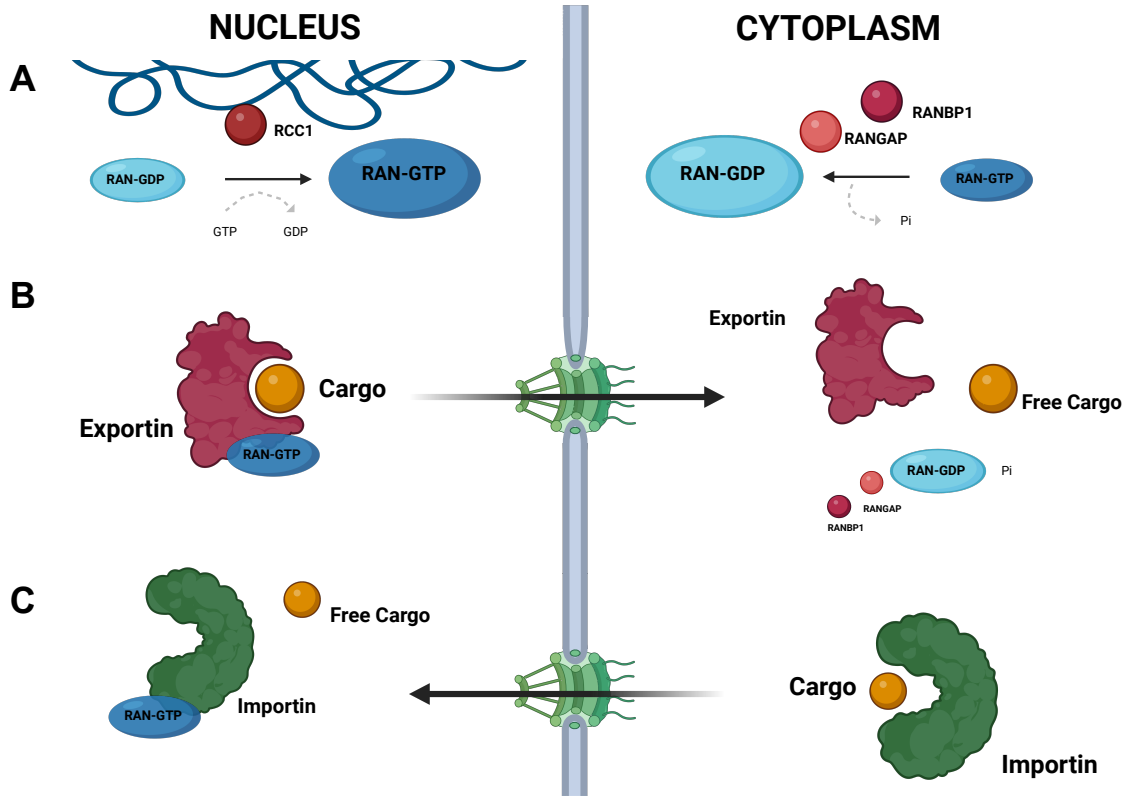

Figure 4. Trafficking of cargoes according to Ran-GTP and Ran-GDP concentrations. Left part of the figure represents the nucleus, and the right part the cytoplasm, separated by the NE. Two NPC are represented in green. **(A)** Ran-GTP concentration in the nucleus is higher due to RCC1. The large size of the RAN-GTP representation indicates its concentration is higher. Ran-GDP concentration in the cytoplasm is higher due to RANGAP and RANBP1. **(B)** Ternary complex of exportin, Ran-GTP and Cargo passing through the NPC and dissociating due to the action of RANBP1 and RANGAP. Ran-GDP and Pi are formed due to the hydrolysis of Ran-GTP. **(C)** Importin binds its import cargo in the cytoplasm and passes through the NPC to arrive to the nucleoplasm, where it will bind to Ran-GTP, releasing its cargo.

In order to be recognized, protein cargoes commonly use short linear amino acid sequences known as nuclear localization signals (NLSs) or nuclear export signals (NESs), for import and export, respectively. Only four classes of NLSs and one class of NESs have been defined, each one for a specific Kap, and targeting signals for many Kaps remain unknown. Each NLS/NES class has distinct sequence patterns and binds to different sites on its designed Kap. Additionally, the three-dimensional conformation of the cargo, as well as various folded domains, play a role in Kap-cargo recognition [64]. Most of the NTRs interact with proteins, but some of them also transport RNA cargoes. In this case, Kaps wrap around the double stranded conformation of the RNA molecule, making electrostatic interactions with the negatively charged RNA backbones and their overhangs [69]. However, some RNA cargoes do not bind directly to their Kaps, but do it via adaptor proteins that drive the transport via their NLS/NESs [64].

20 Kaps have been identified in human cells, including 10 importins, 5 exportins, 3 biportins, and 2 Kaps whose functions remain unknown. These transporters vary in terms of structure and function, playing critical roles in various eukaryotic cellular

processes such as response to the environment, signal transduction, regulation, and maintenance of the cell cycle. An overview of all human Kaps is provided in **Table 1.** Given the diverse roles of Kap family members in the organism, it is not surprising that disruptions of Kap functions contribute to a wide range of diseases, including neurodegeneration, cancer, inflammation, and viral infections.

Kap	Abbreviation	Isoform	Yeast homologue	Functios of putatives cargoes
Exportins				
Chromatin Region Maintenance 1/ Exportin 1	CRM1/XPO1	1	CRM1	Broadly functioning protein cargoes, and various RNA via adaptors
Cellular Apoptosis Susceptibility / Exportin 2	CAS/XPO2	4	CSE1	Importins and possibly, more proteins
Exportin 5	XPO5	1	MSN5	Pre-miRNAs and other RNAs (tRNAs)
Exportin 6	XPO6	2	N.A.	Actin-profilin
Exportin t	XPOT	1	Los1	tRNAs
Importins				
Importin-β	IMPβ	2	KAP95	Broad functions in gene expression and cell cycle regulation, inner nuclear membrane proteins, spliceosomal small nuclear ribonucleoproteins via adaptors
Transportin	TRN1	3	KAP104	mRNA processing
Transportin 2	TRN2	2	N.A.	Trafficking of some mRNAs
Transportin 3	TRN3	4	MTR10	mRNA splicing and transport
Importin 4	IPO4	2	KAP123	Chromatin organization, vesicular transport and cytoskeleton organization, ribosome biogenesis in yeast
Importin 5	IPO5	3	KAP121	Chromatin organization, ribosome biogenesis, cytokinesis, vesicular transport and cytoskeleton organization
Importin 7	IPO7	1	KAP119	Cell cycle regulation, ribosome biogenesis
Importin 8	IPO8	2	KAP108	Ribosome biogenesis
Importin 9	IPO9	1	KAP114	Nucleosome organization, ribosome biogenesis
Importin 11	IPO11	2	KAP 120	Developmental processes
Biportins				
Exportin 4	XPO4	1	N.A..	RNA procesing, ribosome biogenesis
Exportin 7	XPO7	1	N.A.	Broadly functioning protein cargoes
Importin 13	IPO13	1	KAP122	Transcription factors and RNA binding proteins
Unknown function				
RanBP6	N.A.	1	N.A.	N.A.
RanBP17	N.A.	2	N.A.	N.A.

Table 1. Classification of human Kaps. Adapted from [64]

Exportin-dependent nuclear export of RNAs

The transport of RNA molecules from the nucleus to the cytoplasm is a fundamental process for gene expression. After different RNA species are transcribed within the nucleus, they are exported to the cytoplasm through NPCs by different types of Kaps. Following, the principal export routes for each type of RNA are explained, and they are resume in **Figure 5.**

Export of mRNAs

Messenger RNAs (mRNAs) carry genetic information from the DNA to the ribosomes for translation into proteins. They exhibit substantial variation in length, sequence, and structure, which complicates their export. mRNAs are initially synthesized as precursor mRNAs (pre-mRNAs) by RNA polymerase II (Pol II) and subsequently undergo a maturation process that involves the addition of a cap at the 5' end, splicing to remove introns, cleaving the 3' end, and finally polyadenylation. During these successive steps, numerous RNA-binding and -modifying proteins are recruited to the transcripts, forming mature ribonucleoprotein complexes (mRNPs) [70]. Importantly, these factors also serve as export adaptors, establishing a physical bridge between the mRNA molecule and its export receptors, such as XPO1, also called chromosomal region maintenance 1 (CRM). [62,71].

While XPO1's principal function is not related to it, this exportin plays a crucial role in transporting pre-mRNAs [72,73]. XPO1 is involve in the trafficking of a specific subset of transcripts, such as the export of mRNAs from several proto-oncogenes and cytokines that contain AU-rich elements (AREs) in their 3' untranslated regions (UTRs). These AREs can interact with different adaptor proteins containing NES, such as Hur protein or transportin 2 (Trn2), thus linking them to the XPO1-dependent export pathway [74]. Additionally, it is well established that CRM1 functions in the nuclear export of various viral mRNAs, including those that are unspliced or only partially spliced [75].

In addition to XPO1, various proteins and complexes play vital roles in mRNA trafficking [76,77]. One of the most notable complexes is NXF1-NXT1, also known as TAP (Transporter associated with Antigen Processing), which has homologs like Mex67-Mtr2 in yeast [78,79]. Importantly, this exporter is structurally distinct from the Kaps and functions independently of Ran-GTP. Nevertheless, the NXF1-NXT1 complex can interact with FG-Nups, which enables it to pass through the NPC's permeability barrier.

Recent discoveries have shed light on how the transcription-export complex (TREX) recognizes mRNAs once they are processed and packaged into mRNPs. This recognition process licenses the loading of the NXF1-NXT1 complex, facilitating the nuclear export of mRNAs [80].

Export of rRNAs

Ribosomal RNAs (rRNA) are essential components of the ribosomes, the protein-synthesis machines of the cell. Ribosomes are composed of a large (60s) and a small (40s) subunit, which together contain 4 rRNA species (28/25S rRNA, 5.8 rRNA, 5s rRNA and 18S rRNA) and more than 70 ribosomal proteins.

The process of ribosome biogenesis in eukaryotic cells is a highly regulated multistep process that requires the transcription of precursor rRNAs (pre-rRNAs) in the nucleolus, as well as the synthesis of ribosomal proteins in the cytoplasm, with subsequent import into the nucleolus, where they will be assembled to pre-rRNAs to form pre-ribosomal particles. The nuclear export machinery is not recruited at early stages of pre-ribosomal assembly but only at late stages.

Transport of pre-40S and pre-60S particles requires common factors as well as export factors that are unique to each export pathway. XPO1 was the first exportin discovered to be involved in this process. In addition, protein complexes such as Tap-p15 in metazoans (NXF1 in humans) and Rrp12, which interact with FG-Nups, were later found to be important export factors that also promote the transport of both particles [81,82]. Another important factor that has been implicated in the pre-60S particle trafficking in an XPO1-dependent manner is Nmd3p [83].

Export of snRNAs

Spliceosomal small nuclear RNAs (snRNAs) play a crucial role in the processing of pre-mRNA during the splicing process, being involved in the removal of introns. Different types of snRNAs are named according to their specific roles in splicing. With the exception of U6 snRNA, which is produced by Pol III and does not exit from the nucleus, all the remaining snRNAs (U1, U2, U4, and U5) are synthesized as precursors (pre-snRNAs) by Pol II, acquiring a 5' cap, which serves as a signal for nuclear export [84]. The reason why they are exported from the nucleus before being imported again for their function in splicing is still unknown. However, it has been proposed that the cytoplasmic phase of snRNA biogenesis might provide a proofreading step to prevent the nuclear accumulation of non-functional snRNAs [85].

The principal export receptor for snRNAs is XPO1 which interacts with NES-containing adaptors [86], such as the PHAX protein, which binds to the 5' cap of the snRNA for transport [87,88]. In the nucleus, phosphorylation of PHAX is required for the recruitment of XPO1 and Ran-GTP. After export to the cytoplasm, GTP hydrolysis of Ran and the dephosphorylation of PHAX are necessary to efficiently dissociate the export complex and release the snRNA. Once in the cytoplasm, snRNAs undergo a maturation process before being imported back into the nucleus, where they, together with numerous other splicing factors, assemble into the functional spliceosome[85].

Export of miRNAs

Micro-RNAs (miRNAs) are small noncoding RNA molecules that participate in gene regulation. They are produced as larger precursors in the nucleus and eventually mature in the cytoplasm into single-stranded RNA species of 22 nucleotides (nts) that induce post-transcriptional gene silencing through base-pairing homology with their target mRNAs [89].

The trafficking of miRNAs is mediated by the member of the Kap family XPO5, which recognizes the 3' overhang of the miRNA precursor (pre-miRNA). Biogenesis and nuclear export of miRNAs are coupled at several levels. The key enzyme involved in this coupling is Drosha, which generates a double-stranded RNA minihelix with a ~ 2 nt overhang, a unique structure recognized not only by XPO5 but also by the downstream processing enzyme Dicer in the cytoplasm. Thus, a strict linkage of all processing and export steps ensures the high specificity of miRNA production and function [62,90].

miRNAs regulate a wide range of biological processes, including developmental timing, cell differentiation, apoptosis, and immunity against viruses, processes that are frequently altered in cancer. Therefore, it is not surprising that XPO5 is associated with the development of various tumours, such as hepatocarcinoma [91,92].

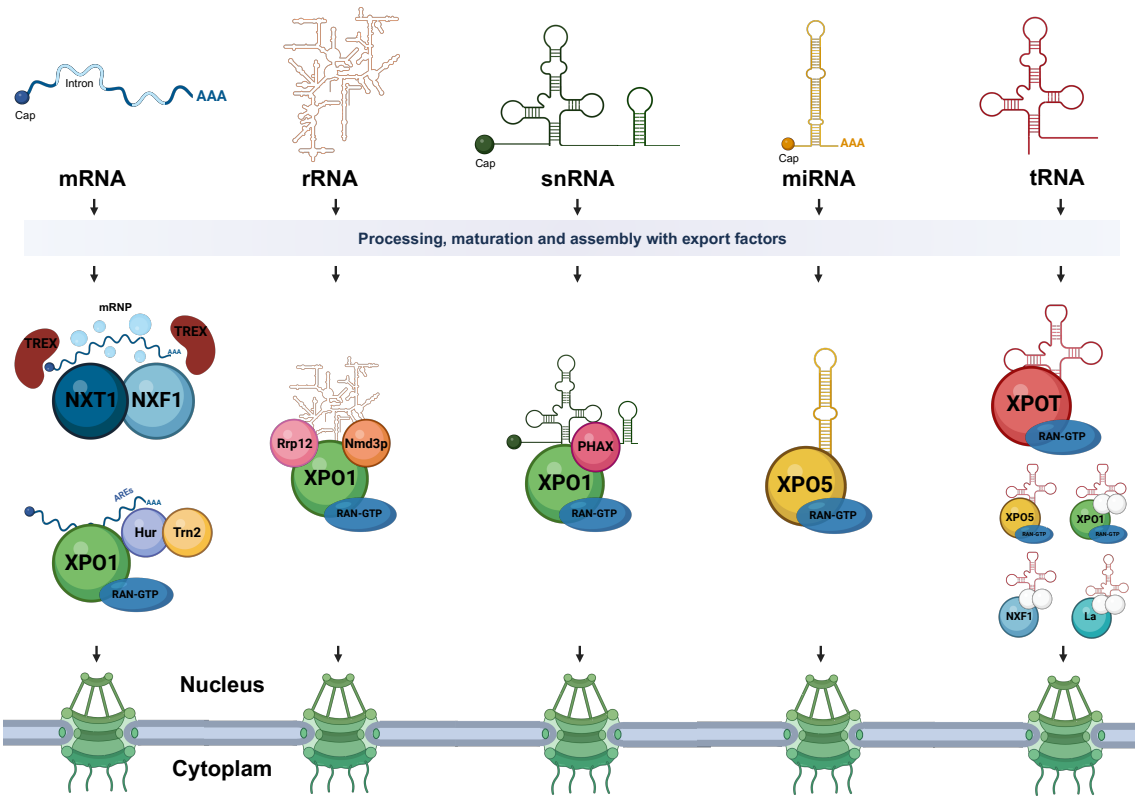

Figure 5. The different RNA export pathways. Major export routes are shown (mRNA, rRNA, snRNA, miRNA and tRNA). In each case, the primary RNA transcript is shown, as well as the transport-competent RNA after it has undergone processing, maturation and assembly with export factors. Exportins from Kap family are represented together with Ran-GTP and the cargo (corresponding RNA) in their ternary structure. Protein adapters of the tRNA adaptors in the case of export leader by XPO1, NXF1 and La protein, are represented as white balls due to the lack of information about these adapters in this field.

Biology and export of tRNAs

Discovered more than 60 years ago [93], tRNAs are key adaptor molecules involved in deciphering the genetic code during translation of mRNAs in protein synthesis, by transporting their cognate amino acid to the ribosome. These molecules are highly structured, commonly consisting of ~ 76 nts arranged in a cloverleaf secondary structure containing three stem loops: D-loop (dihydrouridine-containing loop), T-loop (thymidine, pseudouridine and cytidine-containing loop) also called TΨC loop, and between them the anticodon loop, where a unit of three nucleotides corresponds by homology with other three nucleotides of an mRNA codon (**Figure 6**). These stem loops fold to form the classical L-shaped tRNAs conformation. The arm with the 3' and 5' ends is called amino acid arm and, as the name implies, is where the corresponding amino acid will be ligated [94]. Besides their compact shape, another defining characteristic of some tRNAs is the presence of inosine, a modified adenosine, in their anticodon triplet, which constitutes the basis for the wobble hypothesis [95].

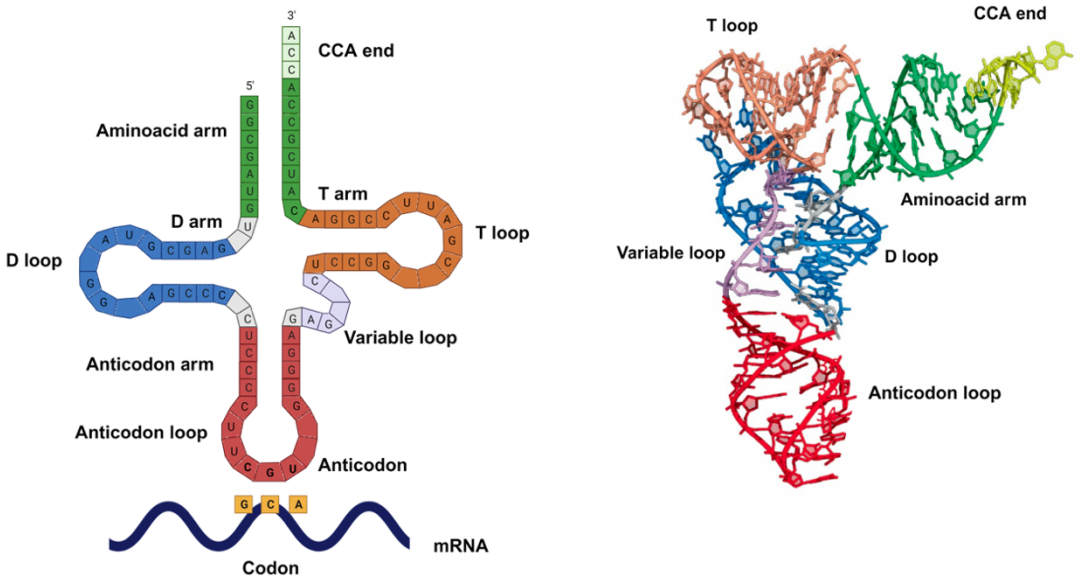

Figure 6. Basic structure of tRNA. Schematic structure of the cloverleaf tRNA structure with anticodon-codon pairing, and tridimensional structure of the tRNA.

Strikingly, the human genome contains around 500 genes encoding nuclear tRNAs, which are transcribed by RNA Pol III, beside 22 tRNAs genes that are encoded by the mitochondrial genome [96]. tRNAs can be classified into two large families: isoacceptor and isodecoder families. There are 21 isoacceptor families, each consisting of tRNAs that encode the same amino acid but have a different anticodon; therefore, there is one isoacceptor family for each amino acid. Isodecoder families, by contrast, are composed of tRNAs that share the same anticodon but present nucleotide differences elsewhere in their structure. Interestingly, the number of isodecoders (as fraction of all tRNA genes) varies widely in eukaryotes and tends to increase across the phylogenetic tree. Half of the human tRNAs genes encode isodecoders, whereas this fraction is as low as 3% in budding

yeasts such as *Saccharomyces cerevisiae*. In light of the presumed functional redundancy between different isodecoders, the reasons why human genomes contain so many tRNA genes remain unclear [97,98].

To accomplish their roles as genome decoders, tRNAs molecules require to be involved in a complex maturation process (**Figure 7**). This process includes the removal of a specific sequences at the 5' and 3' end, as well as a singular splicing process where several proteins are involved. In essence, tRNAs are initially transcribed by the RNA Poll III in an immature form known as precursor tRNA (pre-tRNA). Once transcribed, pre-tRNAs first interact with a RNase called RNAseP, which, along with a ribonucleoprotein complex, cleaves the 5' leader specifically [99]. Subsequently, RNaseZ excises the 3' trailer, a short uridine sequence generated during transcription termination of tRNAs with the assistance of La protein [100]. Following this, a nucelotidyl transferase adds a CCA triplet to the newly processed amino acid arm [101]. The CCA tail is of great importance in tRNA function, as it is recognized by the aminoacyl tRNA synthetases (AARSs), which are responsible for attaching the correct amino acid to each tRNA [102]. The next step in achieving mature tRNAs involves the splicing of the introns. In humans, 28 out of the 429 predicted high-confidence tRNA genes contain introns that require removal through splicing [96,103]. Intron excision and ligation of the 5' and 3' tRNA exons are catalyzed by two multiprotein assemblies: the tRNA splicing endonuclease (TSEN)[104], and the tRNA ligase complex[105,106].

At some point during the maturation process, AARS load tRNA molecules with their specific amino acid. Each AARS is dedicated to one of the 20 standard amino acids and their corresponding tRNAs. The ability to distinguish among numerous tRNAs is just as crucial for maintaining the overall accuracy of protein biosynthesis as differentiating between amino acids. Consequently, the interaction between AARs and tRNAs has been aptly referred to as the "second genetic code", highlighting its pivotal role in upholding the precision of protein synthesis [107].

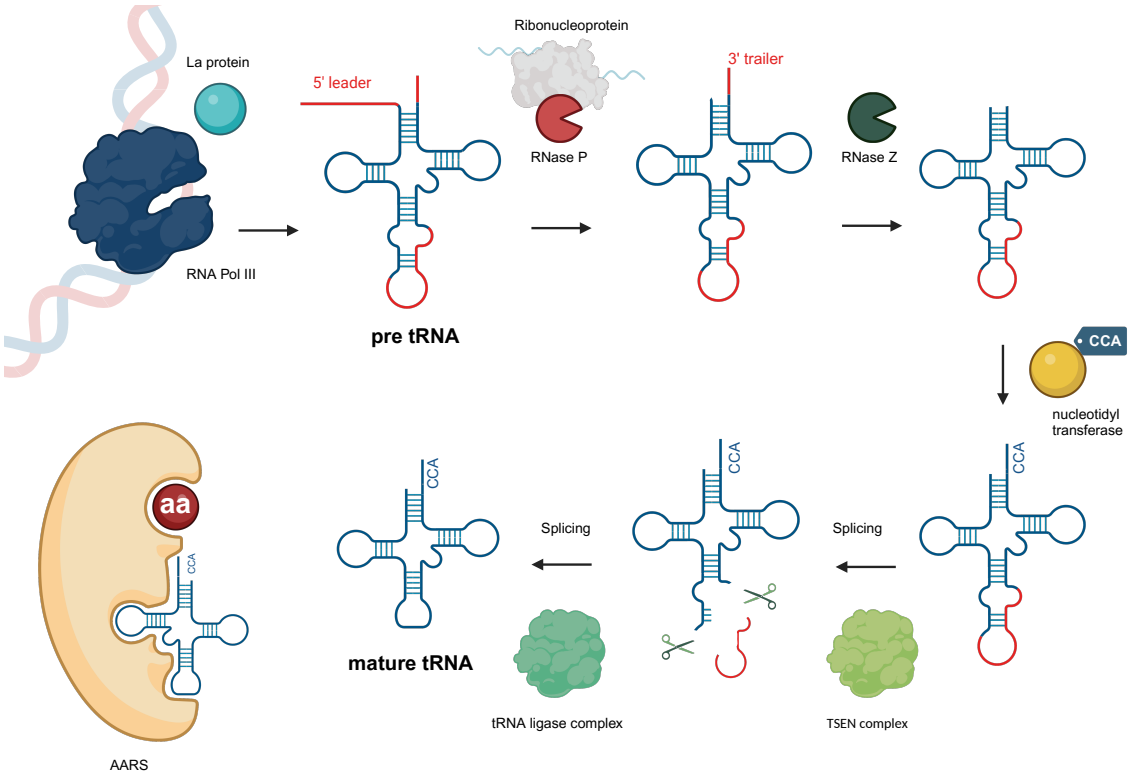

Figure 7. tRNA maturation process. RNA Pol III is represented transcribing the DNA, La protein is assisting the process. Pre tRNA is represented with red sequences that will be removed to finally form a mature tRNA, with the corresponding steps where the different enzymes and complex play a crucial role. AARs (in yellow) is loaded with the corresponding tRNA to ligate the corresponding amino acid.

In addition to the intricate maturation process that tRNAs undergo, these molecular adapters also undergo various post-transcriptional modifications, making them the most modified RNA type[108]. These modifications serve a wide range of functions, although many of them are not yet fully understood. They can vary from simple methylations at the ribose bases to complex and extensive hypermodifications, often requiring a cascade of enzymatic reactions for their synthesis [109].. These modifications are essential for tRNA perform tis functions effectively, and they can dynamically respond to changes in cellular metabolism or environmental cues. Any disruption in these post-transcriptional modifications could potentially interfere with protein biogenesis, thereby disturbing protein homeostasis [110,111].

XPOT as the main tRNA transporter

Although tRNAs are smaller than 40 kDa, the cutoff size for passive diffusion through the NPC, a transport receptor is required for the tRNA to overcome the permeability barrier and hydrophobic meshwork of the NPC [112]. It was in 1998 when in Heidelberg, Germany, at the laboratory leaded by the Prof. Ian William Mattaj and the laboratory of Prof. Dirk Görlich, identified a novel human member of the karyopherin family of proteins. Through the injection of the recently discovered protein into the nuclei of *Xenopus* oocytes and the study in HeLa cells, they demonstrated that in presence of RAN-GTP this new protein forms complexes with tRNAs and transport them to the cytoplasm through the NPC. They could call it human Los1p in reference to its homologue gen in yeast, but due to the lack of strong conservation between species, they decided to name it Exportin-tRNA, XPOT [113,114].

As the rest of the Ran-GTP exportins, XPOT transport its tRNAs cargoes thanks to the RAN-GTP differential gradient between the cytoplasmatic and nuclear compartments. This phenomenon is facilitated by the temporary union of XPOT with the proteins that forms the NPC; XPOT is able to bind in a Ran-GTP-dependent manner to Nup153 and Ranbp2, facilitating the shuttling to the cytoplasm, an in a Ran-independent manner to Nup14 in the cytoplasmatic filaments of the NPC basket [115]. All of this suggest that both, cargo-free and cargo-RanGTP-loaded XPOT are concentrated at the proximity of the NPC facilitating the transporting of its cargoes [116].

Regarding Xpot-tRNA binding, the transporter wraps around tRNA with contacts distributed around the acceptor arm, T-loop, and D-loop. The anticodon arm makes no contacts with the protein [117]. One requisite for XPOT to be able to bind their cargoes, is that the 3' of the aminoacid arm has to be fully modified, with their corresponding addition of the CCA[118]; but the splicing of the tRNA is not needed for XPOT recognition, being not able to discriminate between tRNAs containing or non-containing introns [119]. While free Xpot has an elongated form, Ran-GTP binding to XPOT induces structural rearrangements resulting in a more closed structure of the receptor [117]. Besides its strict role in transport, XPOT also serves as a quality control checkpoint for tRNAs before their export, being able to recognize all mature cellular tRNAs, providing that they are properly folded. Mutations that disrupt tRNA tertiary structure impede transport, making stronger the idea that XPOT recognizes a structural motif in the nucleic acid cargo [102,120]. Aminoacylation of tRNAs appears to be critical in organisms such as *Xenopus oocytes* and yeast for their XPOT/Losp1 transport from the nucleus to the cytoplasm[102,121].

XPOT is not the only tRNA transporter in the cell

Although XPOT is the principal transporter of tRNAs, is not the only protein capable to perform this process. XPO5 [119,122], XPO1 [119], NXF1 [119,123] or La protein [124] are also involved.

XPO5, the transporter of pre-miRNAs, can also export tRNAs through the NPC, although in a less effective way [122]. Together with XPOT, they are the only exportins capable of binding to RNA molecules directly, without the need of adapters. Interestingly, elongation factor 1A (EF1A) plays an important role in the export of aminoacylated tRNAs (aa-tRNAs) together with XPO5. Aa-tRNAs recruit EF1A into a XPO5 complex, facilitating their transport to the ribosome via the NPC[125]. It is not well stablished how XPO5 interacts with tRNAs but does so without discriminating between aminoacylated and non-aminoacylated forms. However, it is known that XPO5 interact with tRNAs different than XPOT. XPOT binds to the amino acid arm, what presumably blocks the access of eEF1A to the 3' end of the tRNA. As a result, XPO5 must recognize tRNA in a distinct manner, allowing for the association of EF1A with XPO5-bound aa-tRNA [122].

XPO1 can export at least 221 NES-containing proteins plus a subset of nuclear RNAs into the cytoplasm [126,127], therefore is not a surprise that it is been involved also in tRNA transport [128]. In yeast, its homologue Crm1 has been recently verified as a *bona fide* intron containing tRNA nuclear exporter, with preferences between tRNAs [119]. But in this organism, the processing of tRNAs differs to humans in several steps. In yeast, before tRNAs play their role into the ribosomes, they are exported from the nucleus twice, due to the splicing of intron-containing tRNAs occurs at the cytoplasmatic face of outer mitochondrial membrane, and after these modifications, the uncharged tRNA has to be reimported to the nucleus to be recognized and aminoacylated by the corresponding aminoacyl tRNA synthetases, to finally be exported again to the cytoplasm [129].

Losp1, is involved in both export events, due to it can bind spliced an unspliced tRNAs. Msn5, orthologous of XPO5, however is only involved in secondary export, binding preferentially to spliced and aminoacylated tRNAs, with or without the help of EF1A, just like in humans. Mex67-Mtr2 (NXF1 orthologous) has been recently linked with tRNA transport as a error-prone transporter, exporting tRNAs to the cytoplasm prior 5' leader removal and without splicing/not splicing discrimination [119].

La protein (autoantigen La, also known as SSB) has been implicated in several tRNA processes, the most ubiquitous of which is the binding of newly synthesized Pol III transcripts, stabilizing them and therefore preventing the digestion of pre-tRNAs by exonucleases [130,131]. Moreover, La is thought to play a pivotal role transporting pre-tRNAs to the cytoplasm [124].

Once in the cytoplasm, a protein called Scyl1 facilitates to EF1A those tRNAs that have been previously charged, allowing them to finally arrive to the ribosome. For protein synthesis [132].

XPOT role in cancer and aging through proteostasis maitenance

tRNAs play a pivotal role in translation by establishing a direct and precise connection between a triplet of nucleotides in mRNA and the corresponding amino acid. However, besides serving as adaptors in translation, tRNAs play additional roles. Thus, they are also important molecules that influence protein expression in the context of cell cycle progression [133], cell proliferation and differentiation [134], stress response [135], cancer and various diseases [136,137], as well as drug resistance [138].

It is established that the abundance of tRNAs in cells can impact translation efficiency [135]. In the scenario of cancer, the overexpression of tRNAs can accelerate the rate of protein synthesis [139]. This can disrupt proteostasis due to an imbalance between mRNA codon usage and the relative abundance of cognate tRNAs, impacting the polypeptide elongation rate and potentially causing pauses in translation [140]. Nevertheless, control of tRNA quantity is not the only factor of importance for their proper function, and the modifications that occur during tRNA maturation are also crucial. Recent works shown that tRNA hypomodification and tRNA-modifying-enzyme deregulation occur in several diseases where proteostasis is affected, namely, neurodegenerative and metabolic diseases [141]. Considering the significance of tRNA regulation for proper cellular function and the maintenance of proteostasis within cells, it is reasonable to expect that the control of their principal transporter is also crucial, and its dysregulation is implicated in a wide range of pathologies.

XPOT role in cancer

Several Kap family members have been found to be altered in neoplastic processes [142]. For example, XPO1 mutations have been identified in diverse hematological malignancies, including classical Hodgkin lymphoma, primary mediastinal B cell lymphoma or chronic lymphocytic leukemia[143–145]. Furthermore, lower expression levels of XPO5 was shown to closely associate with thyroid, liver, larynx, and colorectal cancer [146,147]. Moreover, it is particularly intriguing that the first association of NXF1 with tRNAs was discovered in lung cancer cells lacking the translocated promoter region (TPR) protein, an important component of the NPC [123].

XPOT overexpression has been observed in a significant number of tumors, including neuroblastoma, where high protein levels of the exportin are correlated with a poor prognosis [148]. It is also implicated in hepatocellular carcinoma, contributing to tumor proliferation an invasion [149,150], as well as in breast cancer [151], bladder urothelial carcinoma [152], ovarian cancers and mesothelioma [153,154].

XPOT role in aging

A genome-wide analysis of *Saccharomyces cerevisiae* revealed that deletion of the XPOT ortholog Losp1 robustly extended replicative lifespan (RLS). This comprehensive

study involved 68 researchers from various universities in the United States and Hong Kong and tested 4698 single-gene deletion *S. cerevisiae* strains. It was the very first study to establish a link between Losp1, the subcellular localization of tRNAs and the aging process [155].

Taking together the data from the study, the researchers concluded that blocking nuclear export of tRNAs is sufficient to extend yeast RLS in the budding yeast *S. cerevisiae*. Given our laboratory's focus on investigating factors that regulate aging and longevity, and their connection with cancer, with a specific emphasis on the importance of proteostasis regulation, a significant part of this doctoral thesis has been dedicated to the generation and study of a new mouse model deficient in XPOT.

OBJECTIVES

In recent decades, extensive research has focused on understanding the impact of protein homeostasis on aging. Disruption of proteostasis has been linked to accelerated aging, while its experimental amelioration has been demonstrated to retard the aging process. The maintenance of proteome integrity also plays a significant role in tumor development. Disruptions in protein homeostasis can confer an advantage to cancer cells, whereas, conversely, proteostasis may exert a protective role.

In order to unravel some of these regulators of longevity and cancer, we focused on the mechanisms that protect the cells through proteostasis enhancement, guided by studies that identified two genes with functions not previously associated with them: *Zfand2b*, encoding AIRAPL, a protein involved in the protection against myeloproliferative neoplasms, and *Xpot,* that codes for the tRNA exportin XPOT whose loss in budding yeast expands lifespan by changes in the subcellular localization of tRNAs. Firstly, we explored regulatory mechanisms of protein homeostasis through the proteostasis factors AIRAP and AIRAPL and how they can contribute to myeloproliferative malignancies. Finally, we assessed strategies for proteostasis amelioration to study aging and cancer through the principal tRNA transporter XPOT.

The specific objectives of this Doctoral Thesis were:

1. Generation and characterization of *Zfand2a-Zfand2b* deficient mice to further analyze the role of these proteins in proteostasis control during myeloid malignancies.

2. Generation and characterization of *Xpot*-deficient mice to explore the role of this protein in proteostasis control during aging and tumorigenesis.

EXPERIMENTAL PROCEDURES

Molecular Biology Methods

DNA genotyping

Genomic DNA was isolated from mouse and embryo tail biopsies and using alkaline lysis buffer (NaOH 25 mM, EDTA 0.2 mM, pH=8) followed by 99ºC incubation for 90 min and posterior neutralization (Tris 40 mM, pH=7.4). In all cases, PCR was performed using Platinum™ Taq DNA polymerase (Invitrogen) under the following conditions: denaturation at 95 ºC for 30 seconds, annealing at 60 ºC for 30 seconds, and extension at 72 ºC for 45 s, with 35 cycles of amplification. AIRAP-AIRAPL double knockout mouse model was genotyped using the following oligonucleotides: For *Zfand2a* genotyping: 5'-GGA TGT GCT GCA AGG CGA TTA AGT TGG GTA ACG-3', 5'-ACC CAT GTA AGA GCC AGG CAC TTG CAC-3' and, 5'-GGG CGG AAT GGA TTT GCT GAT CAA GAG-3'. For *Zfand2b* genotyping: 5'-CGC CCA CCC CCC GGA TCT AAG-3', 5'-GCA GGC ATC GCA CTT GAG TGG C-3' and, 5'-GAG CCG AGC TGT CAG CGC TTG-3'. PCR products consisted in a band of 329 base pairs (bp) for the mutant *Zfand2a* allele, and 561 for the wild-type allele. In the case of *Zfand2b,* a band of 561 bp for the mutant allele and 329 for the wild-type allele. For *Xpot* genotyping: 5'-GGG ATC TCA TGC TGG AGT TCT TCG-3', 5'-GGC TGT TTC TTT GTT TTG AGT CAG G-3' and, 5'-ATT TAA AGC TTC CGG GTT AAC TAG AGC-3'. PCR products consisted in a band of 574 for the mutant allele and 435 in the case of the wild-type allele. Fibroblasts for both mice model used in cell culture experiments were also genotyping with the same oligonucleotides

RNA preparation and quantitative-real-time analysis

Collected cells or tissues were homogenized in TRIzol reagent (Life Technologies) and RNA was extracted with the RNeasy Mini kit (QUIAGEN) following the manufacturer's instructions. After extraction, samples were quantified using a NanoDrop ND-1000 spectrophotometer (Nanodrop Technologies) and evaluated for purity (260/280 nm ratio). cDNA was synthesized with the QuantiTect Reverse Transcription kit (QUIAGEN) using 1 μg of total RNA and following the manufacturer's instructions. Quantitative RT-PCR analysis was performed in triplicate for each sample with 20 ng of cDNA using an Applied Biosystems 7300HT Real-Time PCR System. We used SYBR® green PCR Universal Master Mix (Applied Biosystems). For *Zfand2a* expression measurement we used the following oligonucleotides: 5'-ACC CAT GTA AGA GCC AGG CAC TTG CAC-3' and, 5'-GGG CGG AAT GGA TTT GCT GAT CAA GAG-3'. For *Zfand2b* expression measurement: 5'-GCA GGC ATC GCA CTT GAG TGG C-3' and, 5'-GAG CCG AGC TGT CAG CGC TTG-3'. For *Xpot* expression measurement: 5'-GGC TGT TTC TTT GTT TTG AGT CAG G-3' and, 5'-ATT TAA

AGC TTC CGG GTT AAC TAG AGC-3'. As internal control, gene expression was normalized to the *β-actin* gene, using the following oligonucleotides: 5'-CTG AGG AGC ACC CTG TGC T-3' and, 5'-GTT GAA GGT CTC AAA CAT GAT CTG-3'. Relative expression was calculated by $RQ=2^{-\Delta\Delta Ct}$.

RNA extraction for RNA-seq analysis

After extractions, tissues were quickly snap-frozen in liquid nitrogen, and then stored at -80 ºC until RNA extraction. Liver and colons samples were homogenized using a mortar and a pestle with liquid nitrogen, taking special care to maintain the extreme-cold conditions at all times and previously cleaning all the material with RNaseZap (Invitrogen). RNA was then extracted with TRIzol Reagent (Life Technologies), purified with ethanol precipitation and diluted in an appropriate amount of TE buffer pH 8.0, following the manufacturer's protocol. RNA quantity and quality was determined with a Bioanalyzer 2000 (Agilent).

Protein isolation for Western blot analysis and Proteomic analysis

For protein isolation from cultured cells, these were washed in 1x PBS and homogenized in RIPA lysis buffer containing 100 mM Tris pH 7.4, 150 mM NaCl, 10 mM EDTA pH 8.0, 1% sodium deoxycholate, 1% Triton X-100 and 0.1% sodium dodecyl sulfate (SDS), supplemented with protease inhibitors cocktail (Complete, EDTA-free, Roche) and phosphatase inhibitors (PhosSTOP, Roche). In the case of tissues, these were snap-frozen after extraction and stored at -80 oC prior to being homogenized in the same RIPA lysis buffer with a Polytron homogenizer. Protein concentration was determined with the Pierce BCA Protein Assay Kit. Different aliquots were prepared to be studied through proteomic analyses in the corresponding cases and in another set for western blot analysis. For Western blot analysis equal amount of total proteins were loaded onto SDS-polyacrylamide gels. Then, gels were transferred to PVDF membranes, blocked with 5% bovine serum albumin (BSA) in TBST buffer (20 mM Tris pH 7.4, 150 mM NaCl and 0.05% Tween 20) and incubated overnight at 4 ºC with primary antibodies diluted in TBST-3% BSA. After washing, membranes were incubated for 1 h with fluorescently labelled secondary antibodies and scanned on an Odyssey infrared scanner (LI-COR Biosciences). The primary antibodies used in this study were: anti-ZFAND2B (Atlas antibodies, HPA035260), anti-ZFAND2A (MyBioSource, MBS3214310), anti-XPOT (Merk, SAB2102726), anti-XPO5 (Merk, HPA018402), anti-XPO1 (Cell signaling, D6V7N), and anti-β-actin (A5441; Sigma-Aldrich). For proteomic analyses, 3µg of total extract protein were used. Samples were digested with trypsin and labelled with TMT-11. The proteomics analyses were performed in the CRG/UPF Proteomics Unit which is part of the Spanish National Research Infrastructure ICTS Omics Tech.

Plasmid and sgRNA cloning

sgRNA were designed to target human *Xpot,* human and mouse *Xpo5* and , human and mouse *Xpo1* exons. In. each case, three sgRNAs were designed to target different regions of the first exon of each gene by using Benchling CRISPR Design tool. For the infections of human and mouse cells, we used the lentiviral vector lentiCRISPRv2 developed by Dr. F. Zhang (MIT, Boston,USA) [156] (Addgene, #52961), where cloned the following sgRNAs:

- sgRNA-control: 5'-GGAGACGGGATACCGTCTCT-3'
- sgRNA-human-*Xpot*-1: 5'-TTAATTACCTGTATGTCCTC-3'
- sgRNA-human-*Xpot*-2: 5'-TAAAAATTTCCCCAGATGCC-3'
- sgRNA-human-*Xpot*-3: 5'-AGCTTCTGCACACACCTGCC-3'
- sgRNA-human-*Xpo5*-1:5'-GATGAGGTTGGCATGTCGTT-3'
- sgRNA-human-*Xpo5*-2: 5'-GCAGCCTCCCGAGCACAACA-3'
- sgRNA-human-*Xpo5*-3: 5'-GTATCTGAAGAACAGTGTCA-3'
- sgRNA-human-*Xpo1*-1: 5'-GCTAACATTGTCATAATTGC-3'
- sgRNA-human-*Xpo1*-2: 5'-TCAACTGTGTCAGTTTGTAA-3'
- sgRNA-human-*Xpo1*-3: 5'-TTAAATGCTTAGATTTGACT-3'
- sgRNA-mouse-*Xpo5*-1: 5'-GATGTTCATCCTTCTCCGAC-3'
- sgRNA-mouse-*Xpo5*-2: 5'-ATGGAACAGCATGTCCCGAT-3'
- sgRNA-mouse-*Xpo5*-3: 5'-TCAGATAGACCTTCTCCAAT-3'
- sgRNA-mouse-*Xpo1*-1: 5'-TCGACCCGTGTCCAAGCATC-3'
- sgRNA-mouse-*Xpo1*-2: 5'-CTCTGACCCAACTTGTGTAG-3'
- sgRNA-mouse-*Xpo1*-3: 5'-TTCCTTACCTCTACACAAGT-3'

Northern blot analysis

Isolation of total RNA from cell lines was performed using the Trizol Reagent (Invitrogen) according to the manufacturer's instructions. Typically, 5 μg of RNA was separated in a 10% denaturing urea-polyacrylamide gel (20 × 25 cm; Sequagel, National Diagnostics). The RNA was blotted on Hybond- N+ membranes (GE Healthcare) and fixed by ultraviolet cross-linking. Membranes were pre-hybridized in 5× SSC, 20 mM Na2HPO4, pH 7.2, 7% SDS, and 0.1 mg ml^{-1} sonicated salmon sperm DNA (Stratagene) for 1 h at 50 °C. Hybridization was performed in the same buffer overnight at 50 °C including 100 pmol of the different DNA [5′-32P]-labeled probes. Blots were subsequently washed twice at 50 °C with 5× SSC, 5% SDS and once with 1× SSC, 1% SDS and analyzed by phosphorimaging. Membranes were re-hybridized at 50 °C using a DNA probe complementary to U6 snRNA to check for equal loading. Quantification of band intensities was performed using ImageQuant software. Following are indicated the [5′-^{32}P]-labeled probes:

- U6 snRA probe: 5′-GCAGGGGCCATGCTAATCTTCTCTGTATCG-3′
- $tRNA^{Met}_{CAT}$probe:5’-GGGCCCAGCACGCTTCCGCTGCGCCACTCTGC-3’
- $tRNA^{Pro}_{AGG}$ probe: 5’-CTA AGC GAG AAT CAT ACC CCT AGA CCA ACG AGCC-3’
- $tRNA^{Arg}$ probe: 5’-TAGAAGTCCAATGCGCTATC-3’
- $tRNA^{Lys}$ probe: 5’-ATGCTCTACCGACTGAGCTA-3’
- $tRNA^{Gly}$ probe: 5’-TACCACTGAACCACCAATGC-3’
- $tRNA^{Tyr}$ probe: 5’-CTACAGTCCTCCGCTCTACC-3’
- $tRNA^{Leu}$ probe: 5’- GACCACTCGGCCATCCTGAC-3’

Cell Biology Methods

Cell culture

We maintained HEK-293T, NB-4, SKM-1, KG-1, NOMO-1, HL-60, K-562, HEL, JEKO-1, GRANTA, HT, PFEIFER, MEC-1, and JVM-3 cell cultures in Dulbecco’s modified Eagle’s medium (DMEM) supplemented with 10% fetal bovine serum (FBS), 1% penicillin-streptomycin-L- glutamine and 1% antibiotic-antimycotic (Gibco). Hematological cell lines MRC5, A549, Calu-1, H-226, H-358, H-661, H-1792, H-1993, H-2009, FaDu, LNCaP, U-2-OS, MDA-MB-231, and HCT-116 cell cultures in Roswell Park Memorial Institute (RPMI) medium supplemented with 10% FBS, 1% penicillin-streptomycin-L- glutamine and 1% antibiotic-antimycotic (Gibco). In the case of mouse fibroblast cell cultures, DMEM supplemented with 10% FBS, 1% penicillin-streptomycin-L- glutamine and 1% antibiotic-antimycotic plus 1X non-essential amino acids, 10 mM HEPES buffer, 100 μM 2-mercaptoethanol and 1X sodium pyruvate (all from Gibco).

Viral packaging and cell transduction

For lentiviral infection, HEK-293T cells were transfected with the corresponding lentiCRISPRv2 vector with second-generation packaging plasmids using Lipofectamine reagent (Life Technologies). Supernatants were filtered through 0.45 μm polyethersulfone filters to collect the viral particles and added in a 1:3 dilution to previously seeded human and mouse fibroblasts, supplemented with 0,8 μg/ml polybrene (Millipore). Antibiotic selection was done two days after infection and subsequent studies were performed two week later.

Subcellular fractionation

To perform subcellular fractionation the REAP method was conducted [157], with slight modifications. Cells were collected and washed with 1X cold PBS. After centrifugation, supernatants were removed from each sample and cell pellets were resuspended in 900 µL of ice-cold 0.1% NP40 (Calbiochem, CA, USA) in PBS and resuspending 5 times using a p1000 micropipete. Supernatant was collected as cytosolic fraction and subsequently stored at -80 ºC until further use. This step was repeated once again, with the supernatant being discarded. Finally, remaining pellet was resuspended kindly in 1X PBS, and designated as nuclear fraction.

Animal model methods

Animal care

All animal procedures were performed in accordance with institutional guidelines and approved by the Committee of Animal Experimentation of the Universidad de Oviedo and the Consejería de Medio Rural y Cohesión Territorial, Principado de Asturias. All animals were housed in a facility with a photoperiod of 12 h light/12 h dark, at 22 ± 2 ºC, 50 ± 10% relative humidity and fed ad libitum with standard diet.

Generation of new mouse models

To generate AIRAP-AIRAPL new mouse model, AIRAPL mouse model and AIRAP mouse model were crossed. Because this animal exhibited a mixed genetic background, the resulting animals were mated with a C57BL/6N pure strain. Resulting animals were then backcrossed again for a total of 10 times, ensuring the acquisition of an animal with a pure C57BL6 bacground. The Xpot mouse model was carried ogenerrated by the Mutant Mouse Resource and Research Center (MMRRC) through gene trapping in mouse embryonic stem (ES) cells. C57BL/6N mouse ES cells were electroporated with linearized plasmid DNA including an IRES*:lacZ* trapping cassette and a floxed promoter-driven *neo* cassette. ES cell clone HEPD0794_1_A11 containing the trapping cassette inserted between the exons 5 and 6 in *Xpot* gene into chromosome 10, was injected into C57BL/6J-*Tyr*$^{c\text{-}Brd}$ blastocysts. Resulting chimeras were mated to C57BL/6N. Progeny were subsequently backcrossed to C57BL/6N.

Serum metabolites and cell blood analyses

For analysis of serum metabolites, blood was extracted from the mandibular sinus of mice previously anesthetized with isoflurane. EDTA was used as anticoagulant. Blood was centrifuged at 2,000 g and 4ºC, and plasma in the supernatant was collected and measured immediately with an Element HT5 hematology analyzer. For blood glucose determinations, animals were starved for 6 horas to avoid alterations due to food intake. Glucose levels were measured with an Accu-Check glucometer (Roche Diagnostics) using blood from the tail vein. Special attention was paid to avoid inducing additional stress beyond that inherent to the procedure itself, ensuring that glucose levels remained unaffected. For hematological analysis, blood was extracted as above. Cell counting in blood was performed using an Abacus junior vet equipment in the case of AIRAP-AIRAPL mouse model once a month, and Skyla VB1 Veterinary Clinical Chemistry Analyzer in the case of Xpot mouse model.

Histological analysis

Tissues were collected in 4% paraformaldehyde in PBS and embedded in paraffin. H&E staining was performed by Servicios Científico Técnicos from University of Oviedo (Oviedo, Spain), and all samples were analyzed by a pathologist. For the processement of the embryonic samples, paraffin embedding, as well as the subsequent serial sectioning and hematoxylin and eosin staining, were conducted by Patología Molecular Comparada from Centro de Investigación del Cancer (CIC), University of Salamanca. A pathologist from this group analyzed the embryonic samples

Flow cytometry studies

Blood was extracted from mice through cardiac puncture while they were anesthetized with isoflurane throughout the entire procedure. EDTA was used as an anticoagulant. For processing, 10 ml of cold 1X red blood lysis buffer (RBC) (150 mM NH_4Cl, 10 mM $HNaCO_3$, 1 mM EDTA, pH 7.4) was added to the total volume of obtained blood (1 ml) and allowed to act for 3 min on ice. Subsequently, FACS buffer (1X PBS, 10% FBS 2 mM EDTA) was added to halt the lysis. The mixture was centrifuged at 400g for 4 min at 4 ºC, and the supernatant was removed. This process was repeated twice. Finally, the cell pellet was resuspended in an appropriate volume, 200 µl in the case of the AIRAP-AIRAPL mouse model, and Xpot 200 µl in the case of the Xpot mouse model. To process the spleen, initially, a small longitudinal incision was made to rupture the visceral peritoneum covering it. Subsequently, the spleen was mechanically disaggregated on a pre-moistened 40 µm cell strainer with FACS buffer, using a plunger, and the cells were collected in FACS buffer. After centrifugation and removal of the

supernatant, RBC lysis buffer was added, and allowed to act for 3 min. The lysate was neutralized with FACS buffer and then centrifuged. The resulting pellet was resuspended in the appropriate volume of FACS buffer. To process the bone marrow. The tibiae and femurs of the hind limbs were collected and cleaned, removing the surrounding muscle tissue. By centrifuging them at 2000 g for 15 s, the cells comprising the bone marrow were collected in FACS buffer. At this stage, the same procedure as for the spleen was followed to lyse the red blood cells using RBC lysis buffer. Finally, the resulting pellet was resuspended in the appropriate volume of FACS buffer.

To carry the cytometry analysis, in the case of AIRAP-AIRAPL mouse model 10 million cells from spleen, bone marrow and the total number of blood cells were mixed with the antibodies in 0.5 ml of FACs buffer. 30 min later, they were centrifuge at 1200 rpm for 5 min and resuspended again in 0.5 ml of FACs buffer with 5 G of propidium iodide. 10 min later, the sample was pumped into the Northern Lights Spectral Citometer Cytek from the Unidad de Citometría de Flujo y Separación cellular at ISPA-FIMBA (Oviedo, Spain). In the case of Xpot mouse model, 1 million cells from spleen, bone marrow and half the number of total blood cells were mixed with antibodies from the lymphoid panel. Simultaneously, an equivalent number of cells were mixed with antibodies from the myeloid panel. 30 min later, they were centrifuge at 1200 rpm for 5 min and resuspended again in 100 µl of FACS buffer with 2.5 µg of DAPI. 10 min later, the sample was pumped into CytoFLEX (Beckman Coulter Life Sciences) flow cytometer from Servicios Científico-Técnicos of University of Oviedo (Oviedo, Spain). Data from both approaches were analyzed by the computational program FlowJo. The antibody quantities used were those recommended by the commercial suppliers.

Antibodies used in the characterization of progenitor and effector population of the AIRAP-AIRAPL mouse model were the following: CD45-PerCP (Abcam, ab10558), CD3-Pacific Blue (Biolegend, 100213), B220-APC-Fire750 (Biolegend, 103259), Nk1,1-Alexa Fluor 660 (eBioescience™, MA1-70100), Ly6G-PE Fluor 610 (eBioescience™, 61-96668-82), Ly6C-Alexa Fluor 700 (Biolegend, 128024), CD115-PE-Cyanine 7 (Biolegend, 135523), CD11b-PerCP-e710 (eBioescience™, 46-011-280), cKIT-PE (Biolegend, 105808), Ly-6A/E(Sca1)-Brilliant Violet 421 (Biolegend, 108128), CD135-APC (Biolegend, 135310), CD34-FITC (eBioescience™, 11-0349-42), CD48-Brilliant Violet 605 (Biolegend, 103441), CD150-Brilliant Violet 785 (Biolegend, 115937), CD127-Brilliant Violet 510 (Biolegend, 135033), CD16/32-Brilliant Violet 650 (BD bioesciences, 751690), F4/80-Alexa Fluor 532 (eBioescience™, 54-4801-82), CD11c-Brilliant Violet 570 (Biolegend, 117331), SiglecF-Brilliant Violet 480 (BD bioesciences, 746668), CD123- Brilliant Violet 711 (BD bioesciences, 740730).

Antibodies used in the characterization of lymphoid population of Xpot mouse model were the following: CD45-PerCP-Cyanine 5.5 (eBioescience™, 45-0451-82), CD3-FITC (eBioescience™, 11-0032-82), CD45R (B220)-APC (eBioescience™, 17-0452-82), CD4-Alexa 700 (eBioescience™, 56-0041-82), CD8-PE-Cyanine7

(eBioescience™, 25-0081-82). Antibodies used in the characterization of myeloid populations of Xpot mouse model were the following: CD45-PerCP-Cyanine 5.5 (eBioescience™, 45-0451-82), F4/80-FITC (eBioescience™, 11-4801-82), Ly6G-PE610 (eBioescience™, 61-96668-82), CD11B-APC (eBioescience™,17-0112--82), Ly6C-Alexa Fluor 700 (Biolegend, 128024), CD14-PE-Cyanine7 (Biolegend, 123316).

Indirect calorimetry and locomotor measurements

All measurements were performed using the Comprehensive Laboratory Animal Monitoring System (Oxymax CLAMS system by Columbus Instruments) and analyzed following manufacturer's instructions. Mice were housed individually and kept on a 12:12-h light–dark cycle. Mice were monitored for 48 h and the first 24 h were discarded in the analysis, considering them as acclimation period. Total ambulatory activity and food consumption were measured. Food intake was normalized to body weight. Rates of oxygen consumption (VO2), CO_2 production (VCO2) and energy expenditure (EE) were determined and normalized to body weight.

Rotarod test

Motor coordination was evaluated with a Rotarod LE8500 (LSI, LETICA) system by measuring the running time in the rotating bar until fall. The bar started rotating at a speed of 4 rpm and progressively increased to 40 rpm after 5 min. Rotarod tests were performed for 8 days, considering the first 4 days as acclimation. Each day, the test was repeated 3 times in each mouse, leaving a minimum rest of 30 min between each run.

Forelimb grip strength test

The strength of the mice was assessed through a grip strength test using the BIOSEB's Grip Strength Test apparatus (BIOSEB, BIO-GS4). The mice gripped a lever, pulled, and the force applied was measured in grams. This test was conducted on three different days, with three measurements each day, leaving a minimum rest of 30 min between each measure.

Colorectal carcinogenesis

For colon tumor induction, *Xpot*$^{+/+}$ or *Xpot*$^{+/-}$ females of 2 months of age were injected intraperitoneally with 12.5 mg/kg of azoxymethane (AOM; Sigma Aldrich, Ref. A5486). After 5 days, dextran sulfate sodium (DSS; MP Biomedicals, Ref. 160110) at

1.5% was administered in the drinking water for 5 consecutive days. Next, normal water was given for 16 days, followed by two cycles of 5 days on DSS with another cycle of 16 days on standard water between them [158,159]. Ten days after the last DSS cycle, mice were euthanized and colons were extracted, flushed with PBS, measured, and then fixed in 4% paraformaldehyde solution (PFA). Longitudinal sections of colons were stained by hematoxylin and eosin (H&E) and tumors were counted and evaluated by their histological features.

Lung carcinogenesis

For lung tumor induction, urethane (Sigma, 1 mg/kg body weight) was administrated intraperitoneally in 8-week-old-mice. Urethane injection was repeated after 48 h, followed by ten weekly urethane administrations urethane administrations to compensate the relative resistance of C57BL/6 mice strain to this carcinogen. Immediately after finishing the protocol, mice were euthanized, and lungs were harvested and fixed in 4% formaldehyde. Paraffin-embedded samples were cut into serial sections of 100 μm with a microtome and stained with H&E for subsequently pathological evaluation.

Bioinformatics and statistical methods

Statistical analysis

Animals of the same age, sex and conditions were used for comparisons between mice groups. The number of mice included per group was based on previous experiments with randomized distribution. Unless otherwise specified in figure legends, all experimental data are reported as mean ± 95% of confidence interval (CI). Comparison between two groups with normal distribution was performed using a two- tailed Student's t-test assuming same standard deviation (SD). Survival analysis was performed by using the Kaplan-Meier method, and statistical differences were analyzed with the log-rank (Mantel-Cox) test and Gehan-Breslow-Wilcoxon test. Body weight was analyzed using a multiple t-test method assuming same SD. All statistical tests, data analysis, and plots were generated using R and RStudio (R Core Team, Vienna, Austria, https://www.r-project.org; RStudio Team, Boston, MA, USA, https://www.rstudio.com) and GraphPad Prism 9.0. Plots and figures were modified using Adobe Illustrator CC.

RNA-seq, proteomics and bioinformatic analysis

Libraries were prepared using the TruSeq Stranded Total RNA with Ribo-Zero Gold (Illumina) and sequenced as 150 bp paired-end on a NovaSeq6000 Illumina platform with at least 20 million reads per sample by Macrogen. Paired-end reads were aligned to the GRCm39 genome (Ensembl release 106) using STAR (2.7.10a) with default parameters [160]. Raw counts were imported and summarized to gene-level count matrices using tximport (1.22.0) and differential expression analysis was performed using with DESeq2 (1.34.0) [161]. An adjusted P-value ≤0.05 was used as the significance threshold for the identification of differentially expressed genes. Gene-set enrichment analysis (GSEA) were performed using the R package fgsea (1.20) [162]. Genes were pre-ranked by the base-2 logarithm (in) of the fold change multiplied by the negative base-10 logarithm in of the p value [log2FoldChange * -log10(pvalue)]. GSEA was tested for enriched gene-sets from the Gene Ontology (GO) sub-collection extracted from the mouse Molecular Signatures Database through msigdf (7.4). Analysis were performed using R (4.1.3) within RStudio (https://www.rstudio.com/). Plots representing normalized enrichment scores (NESs) from GSEA were generated using GraphPad Prism 9.0. and RStudio.

RESULTS

1. Generation of a new mouse model deficient in two proteostasis factors, AIRAP and AIRAPL

Maintaining protein homeostasis is crucial for an appropriate response to dynamic environments. The presence of regulatory mechanisms of protein quality control preserves the stability and functionality of the proteome, with the ER playing a pivotal role in this regulatory process. Consequently, several components of protein quality control machinery have been implicated in cancer and aging [7,8,163]. Among them, in this first section of the doctoral thesis we are focusing on the proteostasis factors AIRAP, and AIRAPL, encoded by *Zfand2a* and *Zfand2b* genes, respectively. Their orthologue AIP-1 is associated with impaired proteostasis during aging in *Caenorhabditis elegans* [39], and recently studies conducted by our laboratory have linked AIRAPL to tumorigenic processes in the hematopoietic system. Its absence in mice leads to alterations in this compartment, ultimately resulting in the development of myeloid malignancies [42]. On the other hand, although AIRAP plays a similar role in proteostasis maintenance, its deficiency is not associated with any pathological phenotype in mice. To gain insight into these homologous proteins and their role in the generation and development of MPN, have generated a new knock-out mouse model deficient in both proteostasis factors.

1.1 Generation of AIRAP-AIRAPL deficient mice

With the aim of generating a double knockout mouse model deficient in *Zfand2a* and *Zfand2b*, we initially crossed the *Zfand2a*$^{+/-}$ mice obtained from the David Ron Laboratory [41] with the *Zfand2b*$^{+/-}$ previously generated in our laboratory [42]. This breeding resulted in a typical percentage of newborn pups following Mendelian inheritance patterns, with 6.25% of each genotype combination: *Zfand2a*$^{+/+}$- *Zfand2b*$^{+/+}$ (as a wild type control), *Zfand2a*$^{-/-}$-*Zfand2b*$^{+/+}$, *Zfand2a*$^{+/+}$-*Zfand2b*$^{-/-}$, and the double knock out *Zfand2a*$^{-/-}$-*Zfand2b*$^{-/-}$.

Due to the crossing of two different mouse strains, we initially obtained what we refer to as a mixed strain. Subsequently, after ten consecutive crosses with C57BL6 parental mice, we successfully established the double knockout mice with a pure C57BL6 genetic background. To verify that the mouse model did not express *Zfand2a* or *Zfand2b,* we extracted fibroblast from the four different genotypes, expanded them in cell culture and extracted RNA to study the expression of AIRAP and AIRAPL at the transcriptional level by real time quantitative PCR (RT-qPCR) (**Figure 8**). We did not find expression of *Zfand2a* in *Zfand2a*$^{-/-}$-*Zfand2b*$^{+/+}$, neither in *Zfand2a*$^{-/-}$-*Zfand2b*$^{-/-}$ mice. Likewise, we did not observe expression of *Zfand2b* in *Zfand2a*$^{+/+}$-*Zfand2b*$^{-/-}$, or *Zfand2a*$^{-/-}$-*Zfand2b*$^{-/-}$ mice.

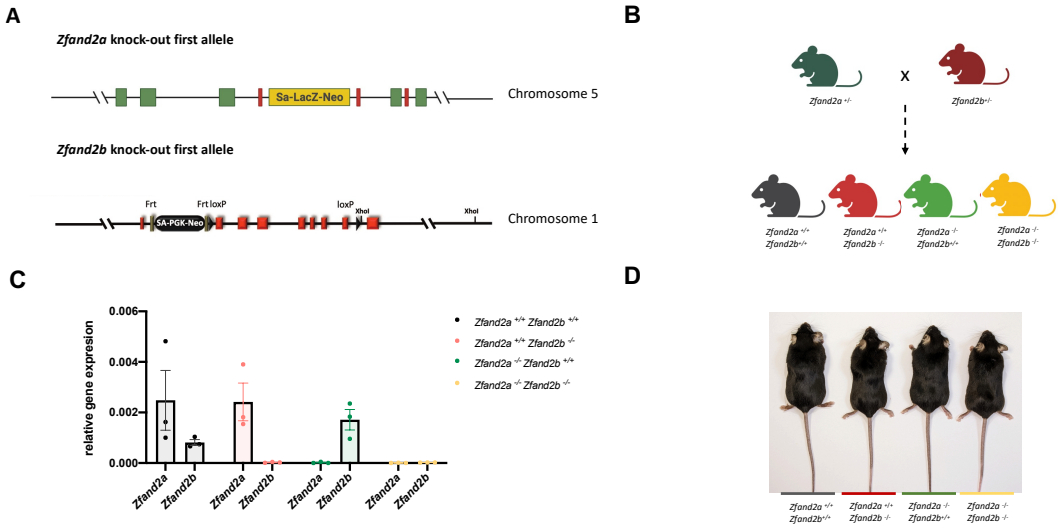

Figure 8. Generation of the double knockout AIRAP-AIRAPL deficient mouse model. (**A**) Schematic representation of the knockout alleles of *Zfand2a* and *Zfand2b* alleles. (**B**) Generation of AIRAP-AIRAPL knockout mouse model by crossing AIRAP deficient mouse model and AIRAPL deficient mouse model. (**C**) qPCR analysis of *Zfand2a* and *Zfand2b* expression of mouse fibroblast extracted from the mouse model. (**D**) Representative image of the four different genotypes.

1.2 Phenotypic characterization of AIRAP-AIRAPL deficient mice

Once we confirmed that the expression of the proteostasis factors were the correct in each genotype, we proceeded to expand the lineage to generate a larger group of mice, first working with the mice in a mixed genetic background, where the lifespan of the mouse model was studied and finally with the pure C57BL6 strain. Lifespan studies revealed that there are not major differences between the *Zfand2a*$^{-/-}$-*Zfand2b*$^{+/+}$ mice and the wild type littermates. However, this was not the case for Zfand*2a*$^{+/+}$- *Zfand2b*$^{-/-}$, as we already knew they have a shorter lifespan compared to the wild type. We observed that the median survival of AIRAPL deficient mice was 567 days, in contrast to the 751 days of the control wild type or the 679 days of the AIRAP deficient mice. The double knockout mice exhibited a similar lifespan to the AIRAPL deficient mice, with a median survival of 585 days (**Figure 9**).

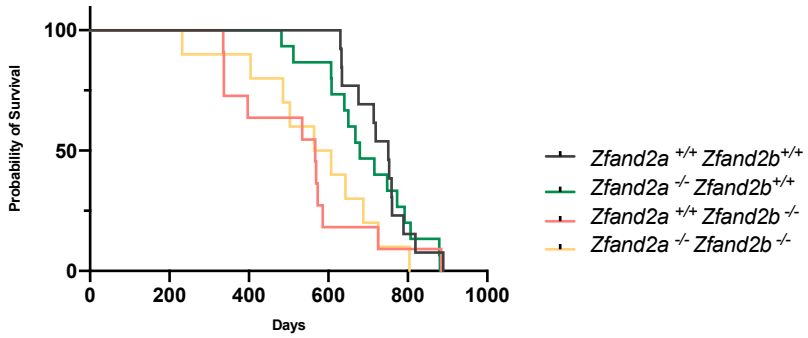

Figure 9. Lifespan study of AIRAP-AIRAPL deficient mouse model. Kaplan Meier survival plot of AIRAP-AIRAPL deficient mouse model in mixed genetic background. n= 13 *Zfand2a*$^{+/+}$-*Zfand2b* $^{+/+}$, n= 12 *Zfand2a*$^{+/+}$-*Zfand2b* $^{-/-}$, n=15 *Zfand2a*$^{-/-}$-*Zfand2b* $^{+/}$, n= 10 *Zfand2a*$^{-/-}$-*Zfand2b* $^{-/-}$. Mean survival: 751 days *Zfand2a* $^{+/+}$ *Zfand2b* $^{+/+}$, 679 days *Zfand2a*$^{-/-}$ *Zfand2b* $^{+/+}$, 567 days *Zfand2a* $^{+/+}$ *Zfand2b* $^{-/-}$ and 585 days *Zfand2a* $^{-/-}$ *Zfand2b* $^{-/-}$.

1.3 Hematologic characterization of AIRAP-AIRAPL deficient mice

To comprehensively characterize this mouse model and further investigate its hematological phenotype, we conducted monthly blood monitoring of the animals, assessing blood cell counts using the Abacus Junior Vet equipment (**Figure 10 A**). We observed no differences between AIRAP deficient mice and their wild type littermates. Conversely, white blood cell levels were significantly higher in the case of *Zfand2a*$^{+/+}$-*Zfand2b*$^{-/-}$ mice and notably even higher in the double knockout mouse model. By the 11th month of life (**Figure 10 B**)., wild type had a median with blood cell count of 6,33 x 10^9 cells/L, whereas *Zfand2a*$^{+/+}$-*Zfand2b*$^{-/-}$ exhibited 17,17 x 10^9 what is higher than the double counts in wild type. Interestingly, *Zfand2a*$^{-/-}$-*Zfand2b*$^{-/-}$ mice had a median count of 31,45 x 10^9 cells/L, nearly five times higher than *Zfand2a*$^{+/+}$-*Zfand2b*$^{+/+}$. On the other hand, *Zfand2a*$^{-/-}$-*Zfand2b*$^{+/+}$ mouse model showed a median count of 8,22 x 10^9 cells/L.

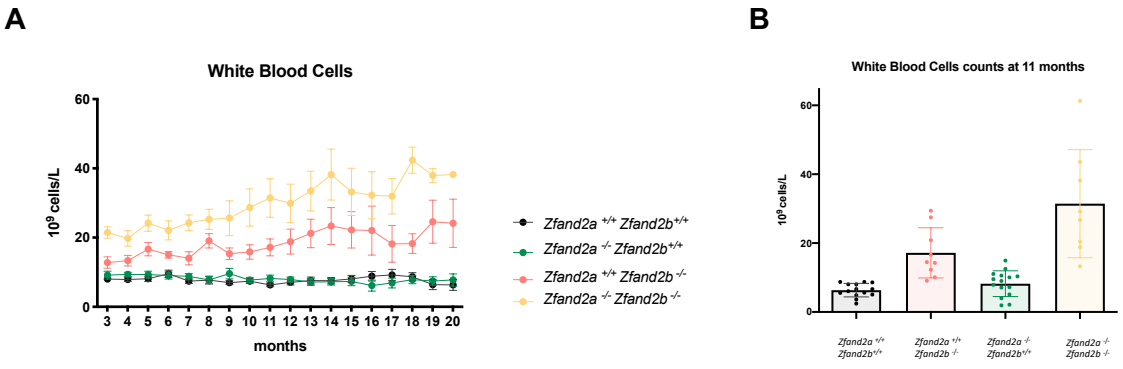

Figure 10. White blood counts of AIRAP-AIRAPL mixed mouse model throughout its lifespan. (A) Total white blood cell count by hematological analyzer Abacus junior vet during 20 months of mouse model in mixed genetic background. (B) White blood cells count at 11th months of life.

Once the pure C56BL/6 murine model was successfully obtained, blood counts were conducted using the Element HT5 hematology analyzer. The study revealed an increase in the total white blood cell count of the double knockout mouse compared to the count of the remaining genotypes. AIRAPL-deficient presented higher amounts of WBC compared with wild type, and no differences were found in AIRAP mice compared to wild type (**Figure 11A**). These data corroborated the findings previously established in the mixed murine model.

Additionally, neutrophils, lymphocytes and monocytes cells were counted, along with red blood cells and platelets. The count of these components was significantly elevated in AIRAP-AIRAPL deficient mice. AIRAPL-deficient mouse exhibited a greater increase of them compared to wild type mice, which is statistically significant only in the case of neutrophils due to the low number of mice studied (**Figure 11 A-D**). No differences were observed between AIRAP-deficient mice and the wild type littermates. Interestingly, no differences have been found in the total number of red blood cells (**Figure 11 E**) or platelets (**Figure 11 F**).

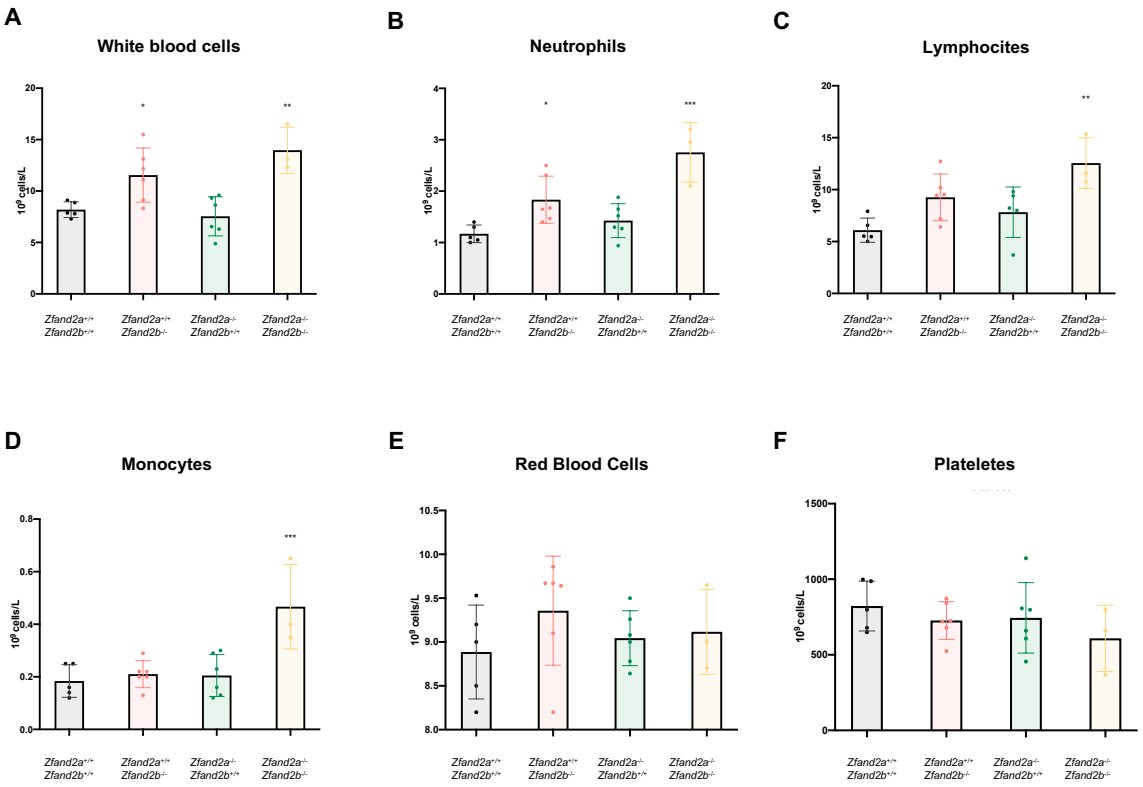

Figure11. Blood cell counts of AIRAP-AIRAPL pure C57BL/6 mouse model at 6 months of life. All count cells were done with the Element HT5 hematology analyzer, 6-month-old mice represented (A) White blood cell counts, (B) Neutrophils, (C) Lymphocytes (D) Monocytes, (E) Red blood cells, (F) platelets.

1.3.1. Design of a hematological panel for the characterization of progenitor and effector cell populations in AIRAP-AIRAPL mouse model for spectral flow cytometry

To gain a more in depth understanding of the hematological study in the murine model, we designed an approach to characterize various populations during hematopoietic differentiation, encompassing progenitor cell and effector cells populations. Through this approach, we aimed to more accurately determine the specific stage of hematopoietic differentiation at which the primary alterations occur in the mouse model under study.

As AIRAPL deficient mouse model exhibits MPNs, cytometry studies were conducted primarily on the myeloid lineage while also pretending to study the principal lymphoid populations. According to the classical model of hematopoiesis, HSC sit at the apex of a differentiation hierarchy (**Figure 12**) and give rise to increasingly restricted progenitors, which subsequently produce and continuously replenish mature blood cells. [164]. In this model, HSCs transition to long-term repopulating HSCs (LT-HSCs), and this to short-term repopulating HSCs (ST-HSCs). Both populations possess self-renewal capacity, although LT-HSC have a higher capacity due to their lower degree of differentiation [165]. ST-HSC sequentially transition through the multipotent progenitor (MPP) stage, which is a complex group of cells without self-renewal capacity. HSCs and MPPs are contained within the Lin^{-} $Sca1^{+}$ $cKit^{+}$ (LSK) compartment, a big population of cells that does not express specific mature markers (Lin^{-} or lineage $^{-}$) and express the surface markers Sca1 and cKit, also known as CD117. LSK compartment is considered as the less differentiated in the hematopoietic hierarchy. Within the MPP population, is possible to distinguish among four different types of progenitors (MPP1/2/3/4), based on the presence or absence of two membrane markers, CD150 and CD48 [166]. MPP1 is closely related to ST-HSCs, also referred to as MPP5, and is positioned downstream of HSCs but upstream of less potent MPP2/3/4 [167]. MPP2 is biased toward the megakaryocyte (MK)/erythroid lineage, MPP3 is largely granulocyte/macrophage biased, and MPP4 is largely lymphoid biased.

Following the hematopoietic lineage, MPPs differentiate into common lymphoid progenitors (CLP), which display lymphoid potential and finally will develop into mature B and T cells, as well as natural killer (NK) cells. Additionally, they give rise to common myeloid progenitor (CMP), which, in turn, gives rise to two major groups of myeloid progenitors: megakaryocyte-erythrocyte progenitor (MEP), responsible at the end of the platelet and erythrocyte production; and granulocyte-monocyte progenitor (GMP). GMPs branches into two directions: on one hand, it generates macrophage and dendritic cell progenitor (MDP); and on the other hand, it produces progenitors that eventually lead to the granulocytic cells known as eosinophils, basophils, and neutrophils. MDPs are responsible for generating dendritic cells, and the common monocyte progenitor (CMoP) from which monocytes will be produced. Depending on the expression level of Ly6C cell surface marker, is possible to differentiate between inflammatory, intermediate, and patrolling monocytes. When monocytes extravasate to invade a tissue, they transform into

macrophages, a population of phagocytic cells distinguishable by the expression of F4/80 marker. All these populations of progenitors and effector cells will be analyzed by flow cytometry, using the Northern Lights spectral flow cytometer (Cytek) with the combination of a total 20 markers represented in the **Figure 12**

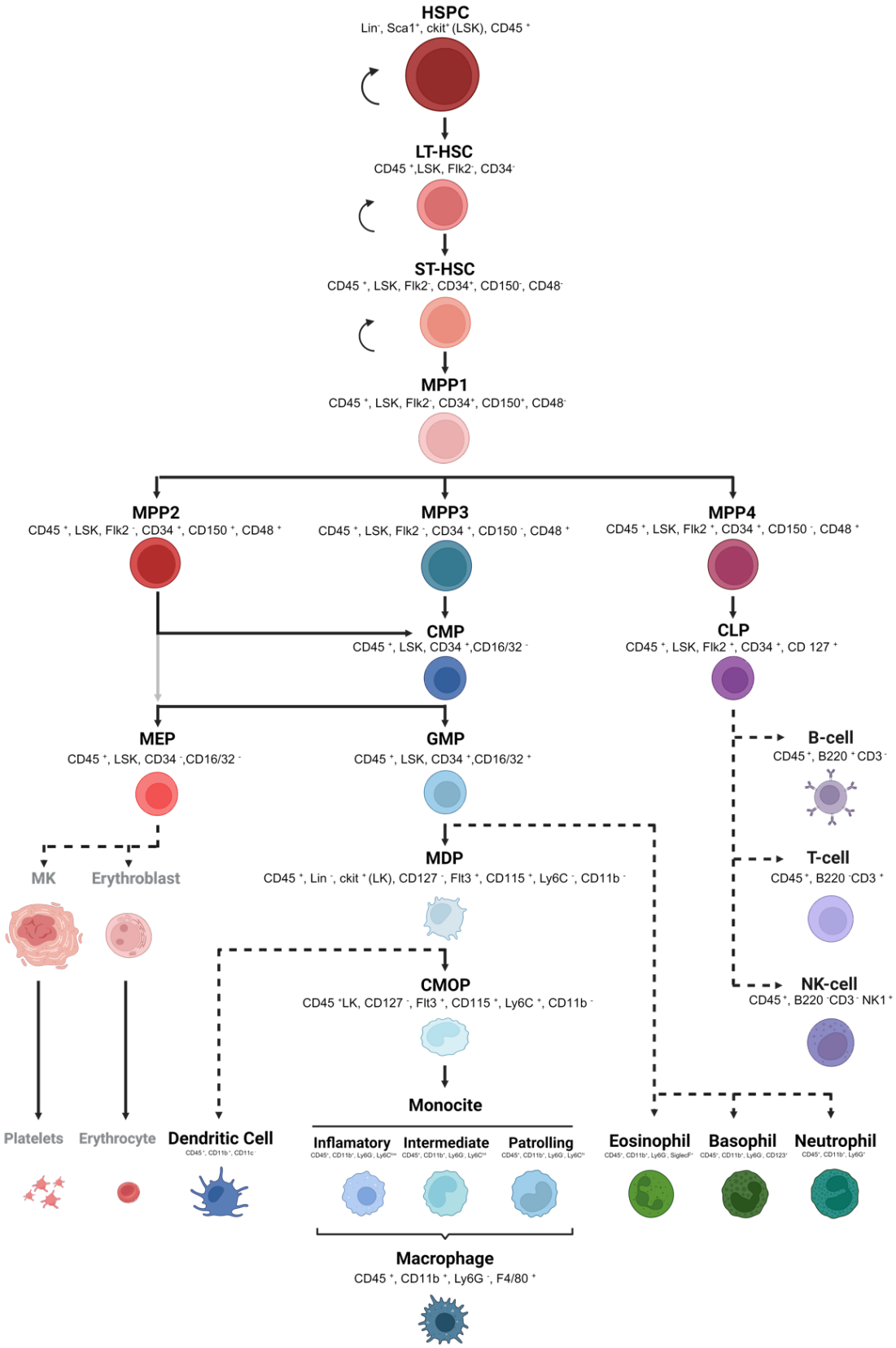

Figure 12. Hemeatopoietic hierarchy representation of the cell population studied in AIRAP-AIRAPL mouse model. Arrows indicate close transition through differentiation. Dashed arrows represent a transition were not all the steps of differentiation are represented. Grey arrow indicate different way of differentiation. Cell population names in gray were not studied in flow cytometry analysis. HSPC (Hematopoietic Stem and Progenitor Cell), LT-HSC (Long Term Hematopoietic Stem Cell) ST-HSC (Short Term Hematopoietic Stem Cell), MPP (Multipotent Progenitor), CMP (Common Myeloid Progenitor), CLP (Common Lymphoid Progenitor), MEP (Megakaryocyte Erythrocyte Progenitor), GMP (Granulocyte Macrophage Progenitor), MDP (Monocyte Dendritic Progenitor), CMoP (Common Monocyte Progenitor) NK cell (Natural Killer cell).

The cytometry study was conducted on the bone marrow (BM), spleen, and peripheral blood (PB) of wild type mice to test the panel and characterize the populations to study. Cells obtained from the tissues underwent red blood cell lysis to specifically study the leukocyte line. A total of 8 million cells from the spleen and BM, as well as all cells obtained from PB, were labeled with the antibody mix and subsequently injected into the spectral cytometer. Propidium iodide was used as a viability marker. Subsequent analyses were performed using the FlowJo software. Total population mentioned above were successfully characterized (**Figure 13**). From the total events introduced in the spectral cytometer, represented using FSC and SSC, we selected then only single cells or singlets, and by selected the propidium iodide negative cells we chosen $CD45^+$ as the total leucocytes to further characterize the cell populations. From $CD45^+$, T cell ($CD3^+$) and B cell ($B220^+$) population were obtained, and the rest were named as noTnoB cells. Within noTnoB, $CD11b^+$ cells correspond with the total of myeloid cells and $NK1.1^+$ to NK cells. From the myeloid cells we differentiated between neutrophils when expressing Ly6G, macrophages when expressing $F4/80^+$, eosinophils as the SiglecF positives and basophils, $CD132^+$. Furthermore, cells expressing CD11c were selected as dendritic cells. From cells no expressing lineage markers (Lin^-) (CD3, B220, NK1.1, Ly6G, Ly6C, F4/80, CD11c, SiglecF and CD123) the progenitor cells were obtained. We were able to differentiate between LK cells (Lin^-, Sca^+,$ckit^+$), LK cells (Lin^-, Sca^-, $ckit^+$), and CLP ($CD135^+$ and $CD127^+$). From LSK cells we identified LT-HSC ($CD135^-$, $CD34^-$), ST-HSC ($CD135^-$, $CD34^+$), and the total of MPPs. Furthermore, form LK cells MPP1/2/3/4 were characterized depending on the expression of CD48 and CD150. Through this comprehensive characterization strategy, we will be able to identify the different populations of effector and progenitor cells in AIRAP-AIRAPL deficient murine model.

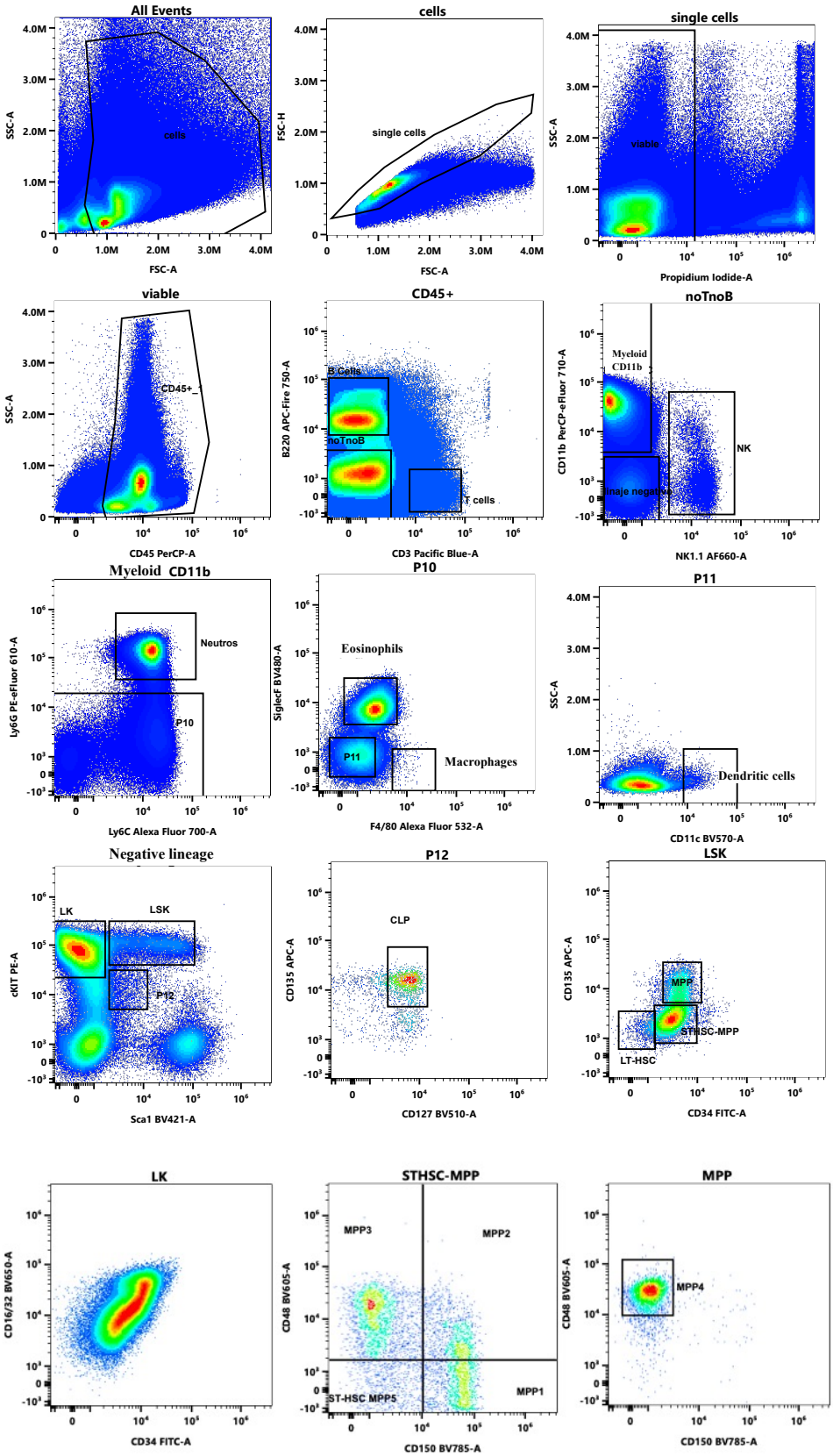

Figure 13. Differential surface marker expression identifies different effector and progenitor cell populations. Representative flow cytometry plots of the 20 cell surface markers studied on 12-months-old murine bone marrow cells.

2. Generation of a new mouse model deficient in XPOT

In most organisms, a decrease in overall health and vitality occurs over time, concomitant with an increased incidence of several significant causes of morbidity and mortality. With the aim of avant-garde genetic techniques, several groups have shown that single genes can exert a profound influence on lifespan [168–170]. The genetic study of lower organisms and its correlation with aging provides valuable insights that contribute to our enhanced understanding of the aging process in higher organism. In yeast, many genes that affect RLS, that means how many daughter cells a mother can produce before it stops dividing, also play an important role in aging in *C. elegans* and *M. musculus.* A comprehensive genome screen of viable budding yeast *Saccharomyces cerevisiae*, which identified 238 long-lived gene deletions, has positioned the *LOS1* gene, *Xpot* orthologous as one of the most significant contributors to the extension of RLS. This discovery is particularly intriguing, as the role of *LOS1* as the primary determinant of subcellular tRNA localization had never been previously associated with aging.[155] Motivated by our laboratory's interest in studying factors that regulate aging and longevity, and because of the consequences of the deficiency of *LOS1* orthologous in vertebrates have not been studied, we have undertaken the development of a knock-out mouse model deficient in *Xpot.* In this second part of the doctoral thesis, we will focus on the generation of the Xpot mouse model, as well as the different approaches carried out to characterize this novel mouse model.

2.1 Generation of Xpot-deficient mice

To explore the importance of XPOT in the development of an organism and gain deeper insight in the role of this exportin in aging, we have generated *Xpot*-deficient mice using a "knock-out first" strategy [171]. The modified allele contains an IRES:*lacZ* trapping cassette and a floxed promoter-driven *neo* cassette inserted between the exons 5 and 6 in *Xpot* gene into chromosome 10. This construction disrupts the gene function, generating a null allele. (**Figure 14 A**) The peculiarity of this design is that this cassette can be easily modified in ES cells or through crosses with transgenic *FLP* and *cre* mice, allowing the mutation to be reverted to wild type [171].

To verify that the mouse model indeed did not express Xpot, we extracted fibroblasts from $Xpot^{-/-}$ and $Xpot^{+/-}$ mice, expanded them in cell culture and extracted RNA and protein to study the expression of Xpot at the transcriptional level by RT-qPCR, and at the translational level by Western blot analysis (**Figure 14 B-C**). We did not find expression of *Xpot* in the knockout animal and levels approximately half when compared with wild type littermate controls $Xpot^{+/+}$.

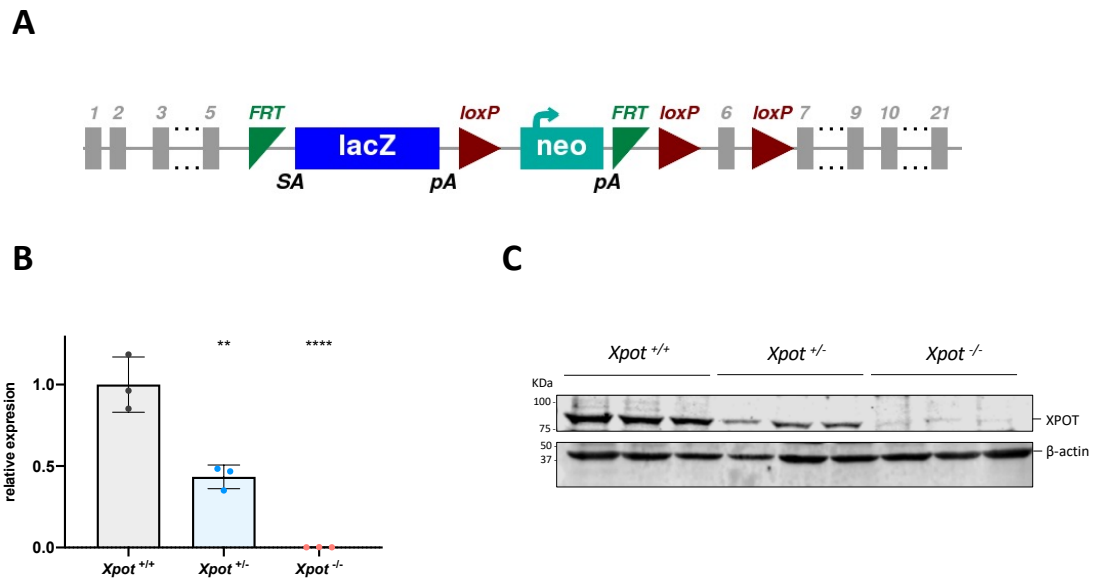

Figure 14. Analysis of *Xpot* expression in Xpot-deficient mice. (A) Schematic representation of a knock out *Xpot* locus in chromosome 10. (B) qPCR analysis of *Xpot* expression of mouse fibroblast, n= 3 $Xpot^{+/+}$, n= 3 $Xpot^{+/-}$,n= 3 $Xpot^{-/-}$; ordinary one-way ANOVA. **** p< 0,0001. Bar plots represent mean ± SD. (C) Western blot analysis of mouse fibroblast.

2.2 Phenotypic characterization of Xpot-deficient mice

Once we confirmed that the murine model, we were working with is indeed a knock-out first model, we proceeded to expand the lineage to generate a larger group of mice. To carry this out, heterozygous $Xpot^{+/-}$ mice were crossed to obtain null $Xpot^{-/-}$. Interestingly, only 2,36% of the total newborn mice were $Xpot^{-/-}$. 57,83 % corresponded to $Xpot^{+/-}$ and 39,81% $Xpot^{+/+}$. A total of 932 pups were analyzed. As shown in **Figure 15 A**, theese percentages do not fit the Mendelian rates. The proportion of males and females was equal in wild type and heterozygous mice, but we found fewer female pups than male,7 versus 15 (**Figure 15 B**).

The small number of $Xpot^{-/-}$ mice that were born exhibited smaller body size compared to their $Xpot^{+/-}$ and $Xpot^{+/+}$ littermates (**Figure 15 C**). From the day of their birth, they displayed smaller body shape and throughout their lifespan, both males and females consistently exhibited reduced body weights (**Figure 15 D**) There was no discernible difference in the size of the $Xpot^{+/-}$ mice, making visual differentiation from the wild type controls impossible, and there was no variation in their weight throughout their lifespan (**Figure 15 C-D**).

Furthermore, *Xpot* knockout mice are characterized by a remarkably shorter lifespan compared to their wild type littermates. $Xpot^{-/-}$ mice live on average for 508,5

days, while wild types live for 887,5 days. Additionally, there are not significant differences between the lifespans of *Xpot*$^{+/-}$ (840 days on average) and *Xpot*$^{+/+}$ mice (**Figure 15 E**).

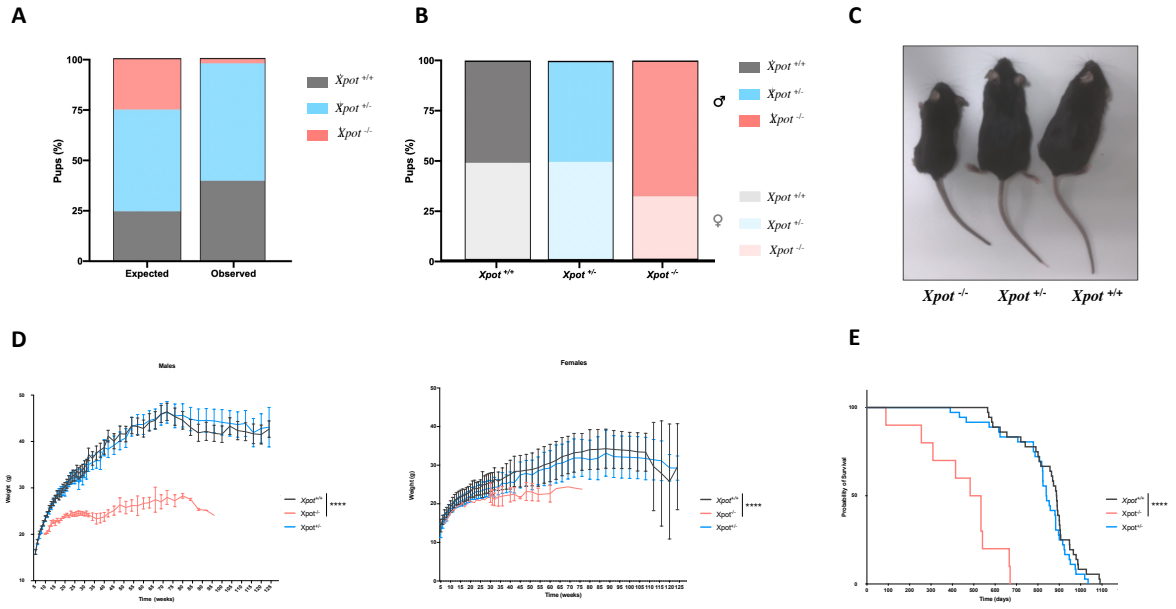

Figure 15 . **Phenotypic characterization of Xpot-deficient mice**. (**A**) Percentage of mice born by genotype n= 932 (**B**) Percentage of mice born by sex in each genotype, n= 371 *Xpot*$^{+/+}$, n= 539 *Xpot*$^{+/-}$,n= 22 *Xpo*$^{-/-}$. (**C**) Representative image showing the phenotypic appearance of these mice. (**D**) Body weight curve in males and females from week 5 until die, for males n= 16 *Xpot*$^{+/+}$, n= 17 *Xpot*$^{+/-}$,n= 7 *Xpot*$^{-/-}$, for females n= 20 *Xpot*$^{+/+}$, n= 19 *Xpot*$^{+/-}$,n= 2 *Xpot*$^{-/-}$. Ordinary one-way ANOVA. **** p< 0,0001 (E) Kaplan-Meier survival plot, n= 36 *Xpot*$^{+/+}$, n= 36 *Xpot*$^{+/-}$,n= 9 *Xpot*$^{-/-}$. Log-rank (Mantel Cox) test and Gehan-Breslow-Wilcoson test. **** p< 0,0001.

2.2.1 Serum biochemistry characterization of Xpot-deficient mice

Biochemical analysis of serum from 13-month-old *Xpot*$^{-/-}$, *Xpot*$^{+/-}$ compared to control *Xpot*$^{+/+}$ mice, revealed that *Xpot* null mice displayed significantly lower levels of cholesterol in blood, also a reduction in amylase levels, although these levels remained within the normal range. The rest of the biochemical analytical values were similar to those of the control group. Glucose analyses were conducted in a distinct group of animals of varying ages, by using a glucometer. For this purpose, two peripheral blood extractions were performed from the tail of the animals after they had fasted overnight on two separate days. The graph in **Figure 16** represents the means of these two days, showing that *Xpot*$^{-/-}$ mice exhibit slightly lower glucose levels compared to their littermates *Xpot*$^{+/-}$ and *Xpot*$^{+/+}$.

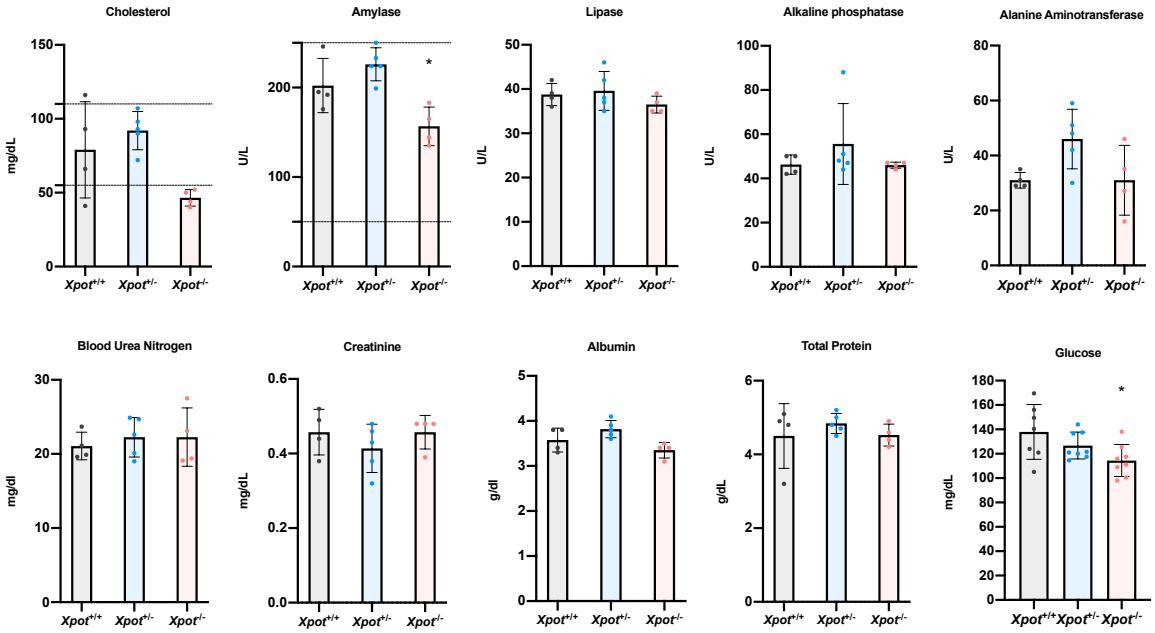

Figure 16. Serum Biochemistry characterization of Xpot-deficient mice. Different serological parameters from total serum, measured with the biochemistry apparatus Skyla. 13-month-old animals n= 4 *Xpot*$^{+/+}$, n= 5 *Xpot*$^{+/-}$, n= 4 *Xpot*$^{-/-}$. Dashed lines indicate the normal range of cholesterol and amylase concentration in a C57BL6 mice. Glucose graph represent the media of two measures in different days, mice were from different ages, from 4 months to 1 year, without differences between age n= 7 *Xpot*$^{+/+}$, n= 8 *Xpot*$^{+/-}$ and n= 8 *Xpot*$^{-/-}$. Ordinary one-way ANOVA, Holm-Sidak's multiple comparison test. P< 0.05 *.

2.2.2 Histopathological characterization of Xpot-deficient mice

Histopathological analysis in 13-month-old animals revealed the presence of extramedullary hematopoiesis in the spleen of *Xpot* $^{-/-}$ mice. H&E staining (**Figure A-B**) showed an abundance of megakaryocytes in the spleen, which exhibit a decreased cellular density in the interfollicular areas and normal sized lymphoid follicles. No significant differences were observed between the spleens of *Xpot*$^{+/-}$ and *Xpot*$^{+/-}$. H&E from livers from 8-month-old mice showed lymphocyte infiltrate centrilobular in *Xpot*$^{-/-}$ and *Xpot*$^{+/-}$ (**Figure 17 C-D**). Other organs studied at the age of 13 months without relevant differences between groups were thymus, lungs, brain, and heart.

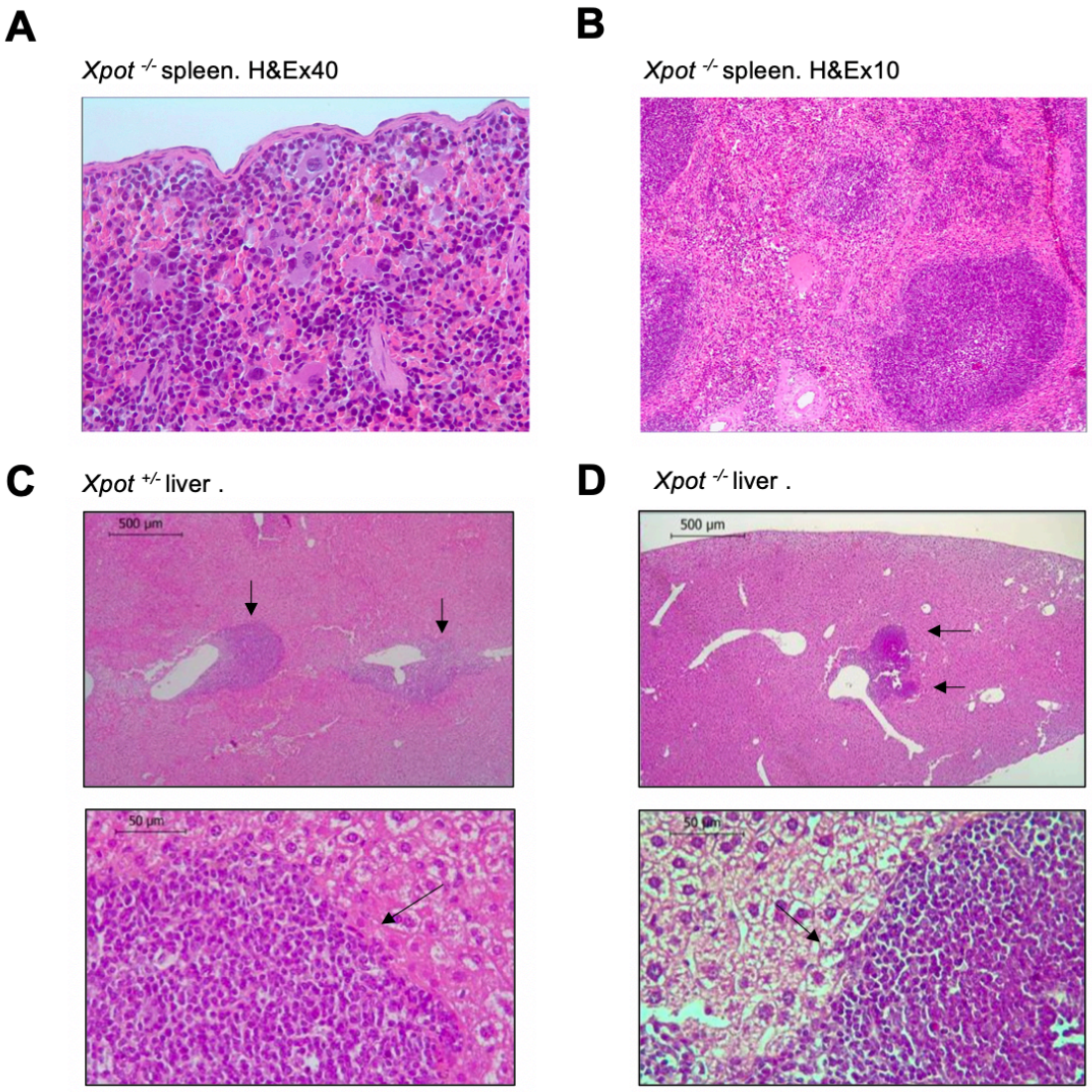

Figure 17. Histopathology studies. (**A**) *Xpot*$^{-/-}$ spleen with abundant extramedullary hematopoiesis. (**B**) Diminished cellular density in interfollicular areas. (**C**) Lymphocytic accumulation indicated by arrows in *Xpot*$^{+/-}$ and (**D**) *Xpot*$^{-/-}$ mouse livers.

2.3 Hematological characterization of the Xpot-deficient mice

Guided by the histopathological information about inflammatory infiltrates in the liver and supported by previous studies using the Element HT5 hematology analyzer, where an increase in total white blood cells in peripheral blood was observed (data not shown), we decided to conduct more comprehensive flow cytometry studies. These studies encompassed peripheral blood, spleen, bone marrow, and the inflammatory infiltrate in the liver.

The study was divided into two parts, focusing on the immunophenotyping the effector cells of the lymphoid and myeloid lineages. To achieve this, we employed two distinct panels, allowing us to detect various cell population within these compartments

by flow cytometry (**Figure 18**). Firstly, to study all the populations of interest, we employed the computational program FlowJo, to divide the cells population into different gates. From the total events introduced in the flow cytometry, represented using FSC and SSC, we selected them into single cells or singlets, and by selected the DAPI marker, we specifically selected the live cells (**Figure 18 A**). Starting with these live cells and selecting the $CD45^+$ positive cells as a marker of global leucocytes, we differentiated between the two lineages, lymphoid lineage (**Figure 18 A**) and myeloid lineage (**Figure 18 B**)

Within the lymphoid lineage (**Figure 18 A**), our panels enabled the differentiation of B lymphocytes ($CD45^+$ $B220^+$) and T cells ($CD45^+$ $CD3^+$), further subdividing the latter into cytotoxic T cells ($CD45^+$ $CD3^+$ $CD8^+$) and helper T-cells ($CD45^+$ $CD3^+$ $CD4^+$). Additionally, we investigated NK cells ($CD45^+$,$NK1.1^+$). On the other hand, the specific panel for the myeloid lineage (**Figure 18 B**), allowed us to differentiate cells expressing the adhesion integrin CD11b marker, which is present in cell types such as neutrophils, monocytes/macrophages, granulocytes, and NK cells. We referred to these $CD11b^+$ cells as "myeloid cells", even though this marker is also present in NK cells. However, the percentage of this population in NK cells is so small that CD11b is a canonical myeloid marker. Cells expressing the Ly6G marker ($CD45^+$ $CD11b^+$ $Ly6G^+$) were identified as neutrophils. Cells that were $Ly6G^-$ were differentiated based on their size into eosinophils ($CD45^+$ $CD11b^+$ $Ly6G^-$ $SSC\text{-}A^{hi}$) and a heterogeneous population of macrophages/monocytes. Within this population, four subtypes were distinguished by the expression of F4/80 and Ly6C receptors: macrophages ($CD45^+$ $CD11b^+$ $Ly6G^+$ $SSC\text{-}A^{lo}$ $F4/80^+$), patrolling/non classical monocytes ($CD45^+$ $CD11b^+$ $Ly6G^+$ $SSC\text{-}A^{lo}$ $F4/80^-$

Ly6C^{lo}), intermediates monocytes (CD45^{+} CD11b^{+} Ly6G^{+} SSC-A^{lo} F4/80^{-} Ly6C^{int}) and inflammatory monocytes (CD45^{+} CD11b^{+} Ly6G^{+} SSC-A^{lo} F4/80^{-} Ly6C^{hi}).

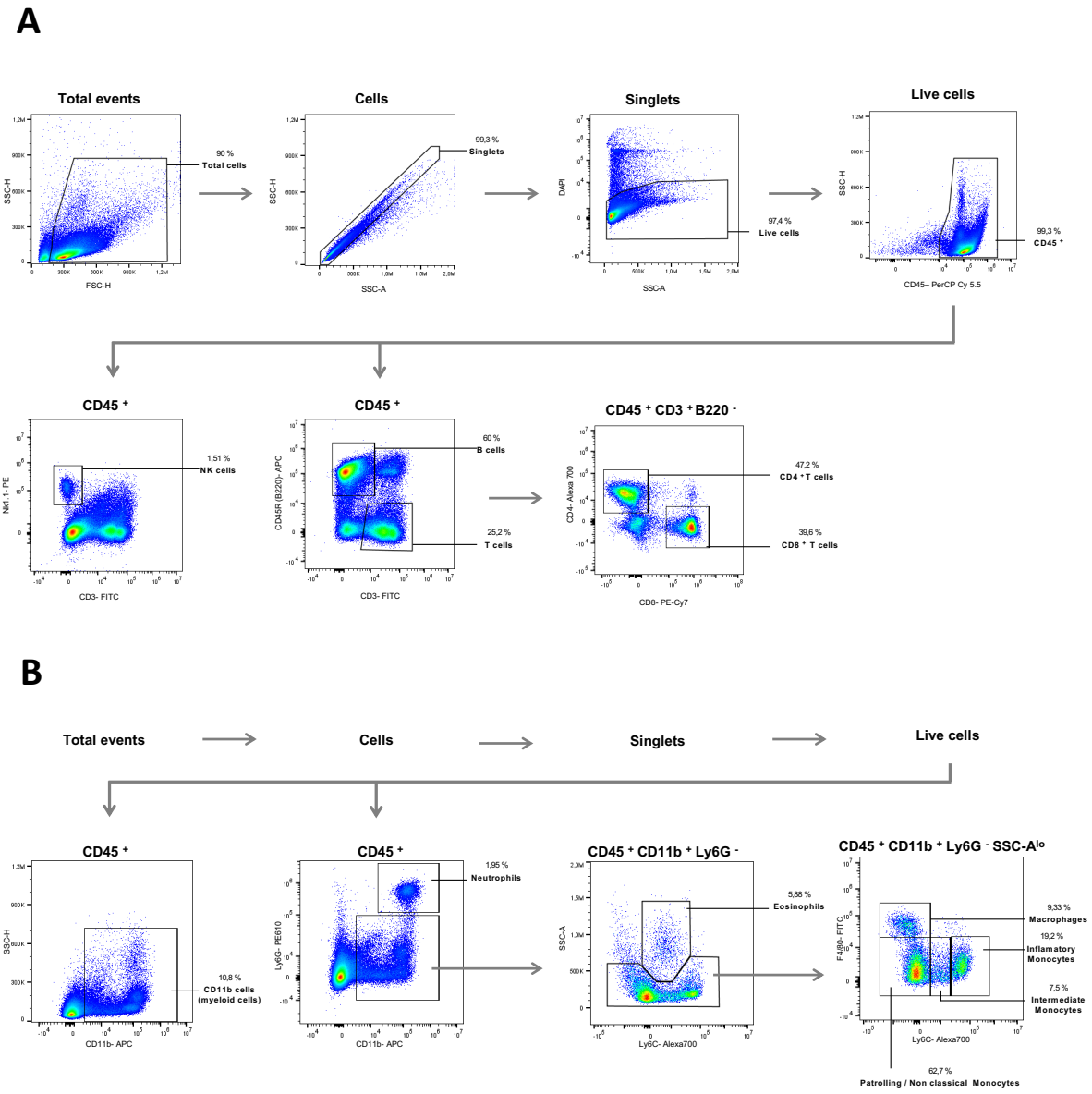

Figure 18. Gating strategy for specific population. (**A**) Lymphoid lineage is represented. A *Xpot* $^{+/+}$ spleen is represented. (**B**) Myeloid lineage is represented. The same *Xpot* $^{+/+}$ spleen is represented, but they were analyzed in different panels.

2.3.1 Lymphoid lineage characterization of Xpot-deficient mice

Based on these panels we found that the most altered population in all the compartments studied from Xpot mouse model was the one corresponding to lymphocytes B, which is significatively lower in Xpot-null mice when compared with wild type mice. Surprisingly, the levels of B cells in *Xpot*$^{+/-}$ were considerably high compared not only to *Xpot*$^{-/-}$ but also with *Xpot*$^{+/+}$ controls (**Figure 19 A**). Levels of T cells were also elevated in *Xpot*$^{-/-}$ when compared to control littermates (**Firuge 19 B**). In the case of *Xpot*$^{+/-}$ mice, higher T cell levels were observed in blood, but not in the other

compartments, where they were found in lower proportion compared to wild type mice. These results suggest that the increase in the number of T cells in *Xpot*$^{-/-}$ mice could correspond to an increase in the number of CD4^{+} cells, as evidenced by an increase within the CD3+ population, along with a decrease in CD8^{+} cells, both in blood and spleen (**Firuge 19 D).** No differences were found in bone marrow (data not shown). NK cells were especially high in blood of null-*Xpot* mice. However, this was not the case in bone marrow, where they were found diminished. This population of innate immune cells in *Xpot*$^{+/-}$ mice followed the same trend as the knockout mouse but not as pronounced.

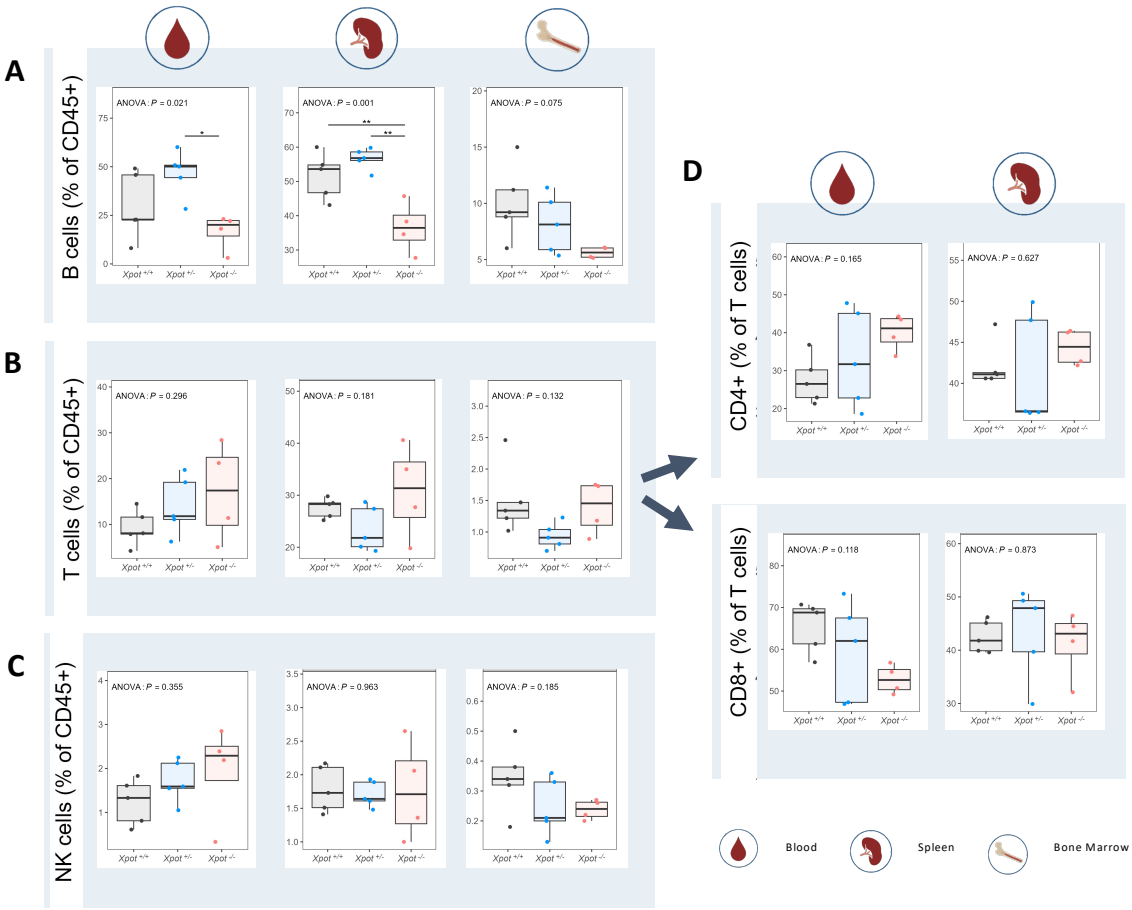

Figure 19. Cytometry studies of different hematological compartments of Xpot-deficient mice. Lymphoid lineage represented. (**A**) Percentage of B cells, (**B**) T cells and (**C**) NK cells of a total of CD45^{+} cells from peripheral blood, spleen, and bone marrow of Xpot mouse model. (**D**) represent percentage of CD4^{+} and CD8^{+} from the total of T cells (CD3^{+}) in blood and spleen. n= 5 *Xpot*$^{+/+}$, n= 5 *Xpot*$^{+/-}$, n= 4 *Xpot*$^{-/-}$ 13-month-old mice.

2.3.1 Myeloid lineage characterization of Xpot-deficient mice

Regarding myeloid cells (CD11b^{+}), they were especially high in the spleen of *Xpot*$^{-/-}$ mice (**Figure 20 A**), where neutrophils, eosinophils, inflammatory monocytes and intermediate monocytes (**Figure 20 B-E**) are high when compared to control and *Xpot*$^{+/-}$ mice. There were no differences when talking about patrolling/non classical monocytes

into the total CD45^{+} cells (data not shown). However, they were significatively lower within the macrophage/monocyte population (**Figure 20 F**), perhaps due to the increase of the inflammatory and intermediate monocytes increase.

In *Xpot*$^{-/-}$ blood and bone marrow, CD11b^{+} cells, neutrophils, and eosinophils exhibited higher counts compared to wild type (**Figure 20 A-C**). Interestingly, in heterozygous mice, these populations in these compartments showed contrasting behaviors. Inflammatory monocytes were reduced in both *Xpot*$^{-/-}$ and *Xpot*$^{+/-}$ mice in blood and bone marrow (**Figure 20 E**), while patrolling/non classical monocytes showed a slight increase (**Figure 20 F**). This last contrasted to the findings in the spleen.

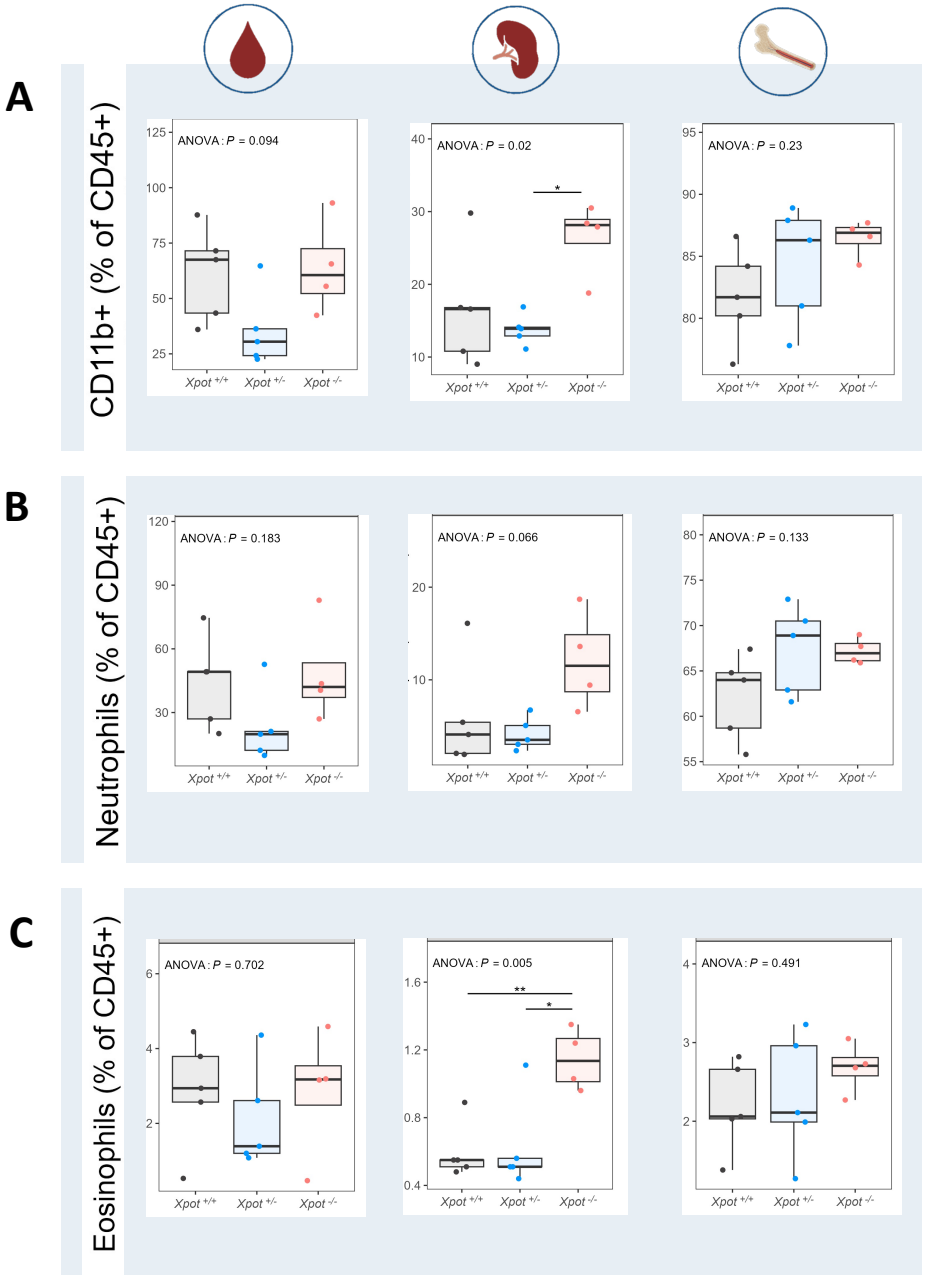

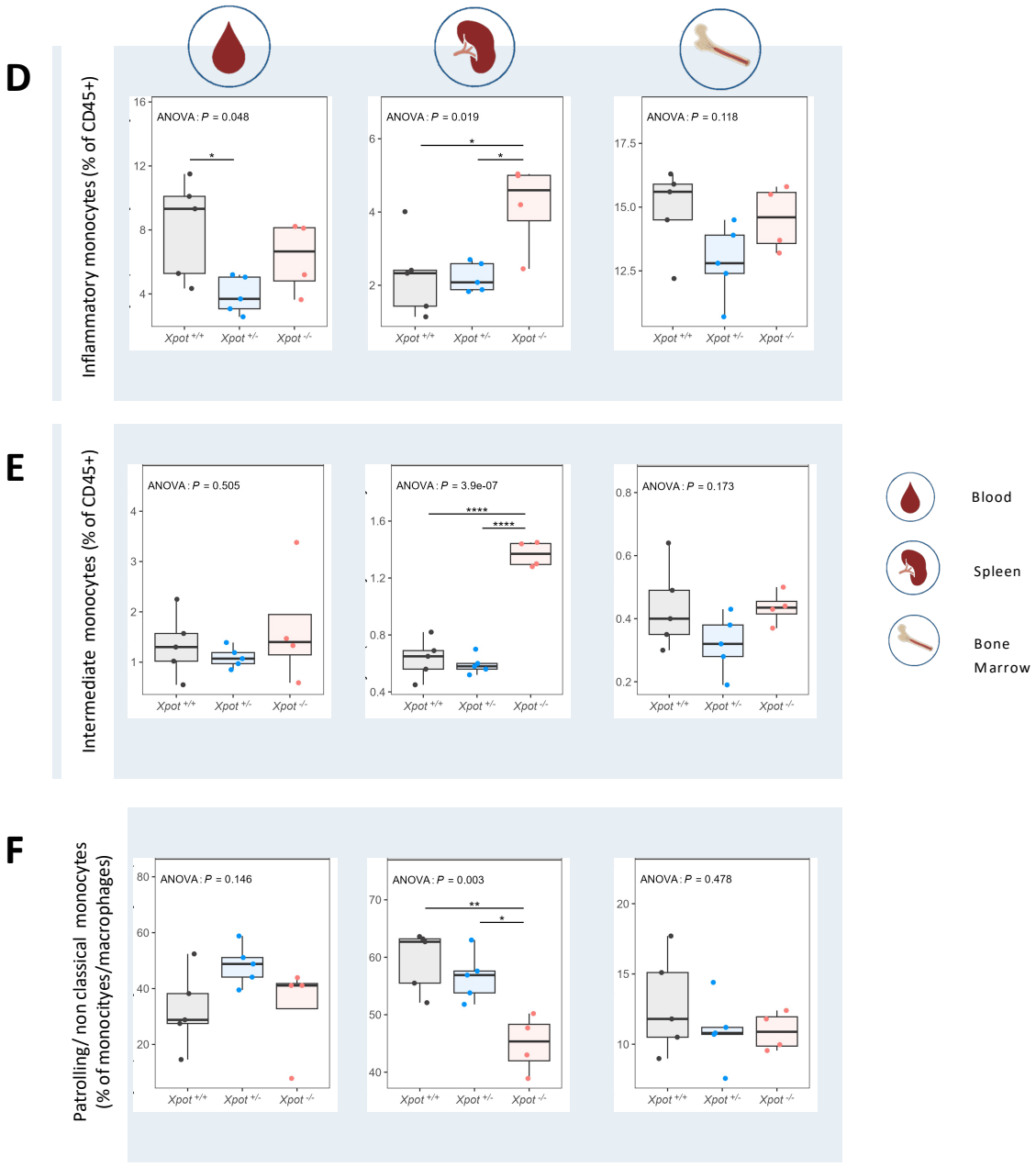

Figure 20. Cytometry studies of different hematological compartments of Xpot mouse model. Myeloid lineage represented. (**A**) Percentage of $CD11b^{+}$, (**B**) neutrophils, (**C**) eosinophils, (**D**) inflammatory monocytes, and (**E**) intermediate monocytes from total $CD45^{+}$ cells. (**F**) Patrolling / non classical monocytes are represented from the total of monocytes/macrophages ($CD45^{+}$ $CD11b^{+}$ $Ly6G^{-}$). Blood, spleen, and bone marrow were analyzed. n= 5 *Xpot*$^{+/+}$, n= 5 *Xpot*$^{+/-}$, n= 4 *Xpot*$^{-/-}$ 13-month-old mice.

2.3.1 Liver Inflammatory infiltrate characterization of Xpot-deficient mice

Due to the results obtained from the histopathological analysis on the liver, we decided to characterize the hematological populations present in the inflammatory infiltrate of livers from the mutant mice model's. For this purpose, organ perfusion was conducted through a continuous infusion of saline buffer, aiming to remove as much peripheral blood as possible by irrigating the liver, focusing solely on studying the infiltrate. Subsequently, mechanical disaggregation was performed, following a

procedure similar to that applied to the spleen. Flow cytometry analysis revealed a considerable decrease in the B lymphocyte population (**Figure 21 A**), elevated levels of T cells (**Figure 21 B**), and an increase in NK cells (**Figure 21 C**) in *Xpot*$^{-/-}$ mice.

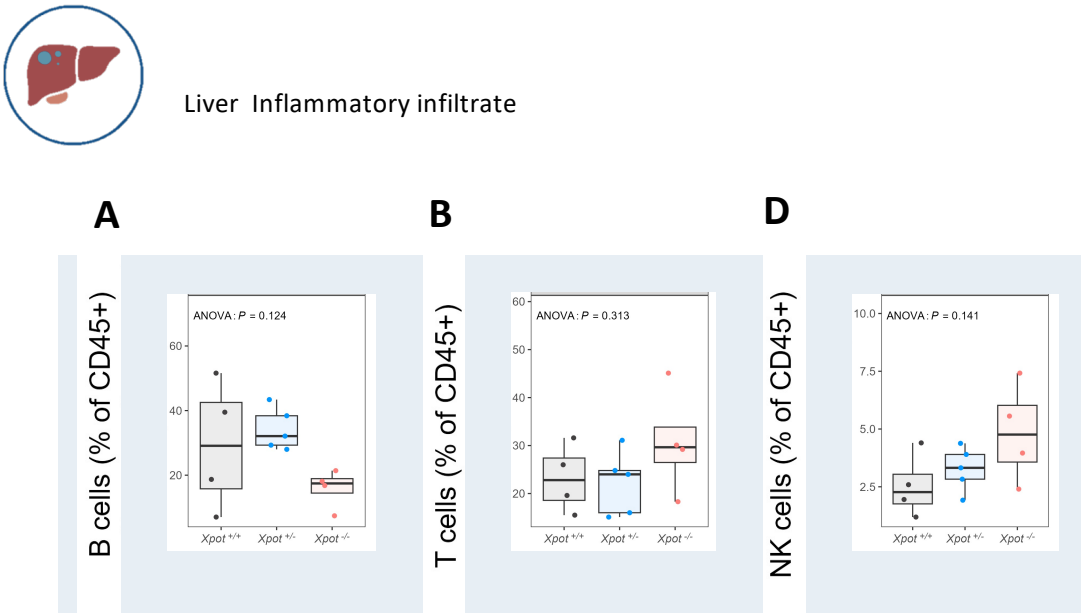

Figure 21. Cytometry studies from liver's inflammatory infiltrate of Xpot-deficient mice. (**A**) Percentage of B cells, (**B**) T cells and, (**C**) NK cells from the total of CD45^{+} cells.

2.4 Physiological characterization of the Xpot-deficient mice across age

To further characterize Xpot deficient mouse model and study it throughout its lifespan, we established two age-based groups of animals: one group comprised of young mice, and the other of older mice. These groups were categorized based on the three different genotypes, *Xpot*$^{+/+}$, *Xpot*$^{+/-}$, and *Xpot*$^{-/-}$. Subsequently, these mice underwent a metabolic test using Oxymax apparatus (CLAMS), motor coordination test using the Rotarod apparatus, a forelimb grip strength test.

2.4.1 Metabolic assessment of Xpot-deficient mice

Guided by previous studies that revealed the increasement of important metabolic pathways as glycolysis or lipolysis, we decided to conduct metabolic studies in the murine model using the Oxymax system. This apparatus provides information on oxygen and carbon dioxide quantities consumed during the day, as well as the energy expended by the animal and the respiratory exchange ratio, which informs us about the mouse's energy source. In addition to these metabolic data, the Oxymax system provides information regarding the mouse's movement throughout the day, as well as its water and food consumption. The experiments were conducted in separate batches, and mice were placed

in the metabolic cages of the system for two days, with measurements taken on the second day considered optimal due to the animal`s acclimatization.

Results revealed an increased in the consumption of oxygen and carbon dioxide in young mice as well as when they age. Furthermore, an elevation in the energy expenditure of *Xpot*$^{-/-}$ mice was found when compared to wild type (**Figure 22 A-B**). Surprisingly, *Xpot*$^{+/-}$ data showed the opposite when compared to wild type: oxygen consumption is lower in young and old *Xpot*$^{+/-}$ mice. Carbon dioxide production is also lower when young, with no differences found when compared with controls as they age. Energy expenditure is lower throughout the life of the *Xpot*$^{+/-}$ mice too. To better understand the metabolic characterization of the mouse model across age, data obtained from the young group were compared with data from the old group. No differences were observed in *Xpot* null mice, but interestingly, differences were found when *Xpot* were lacking in heterozygosity in mice. Levels of carbon dioxide production increase with age, and notably, the respiratory exchange also increase (**Figure 22 C**).

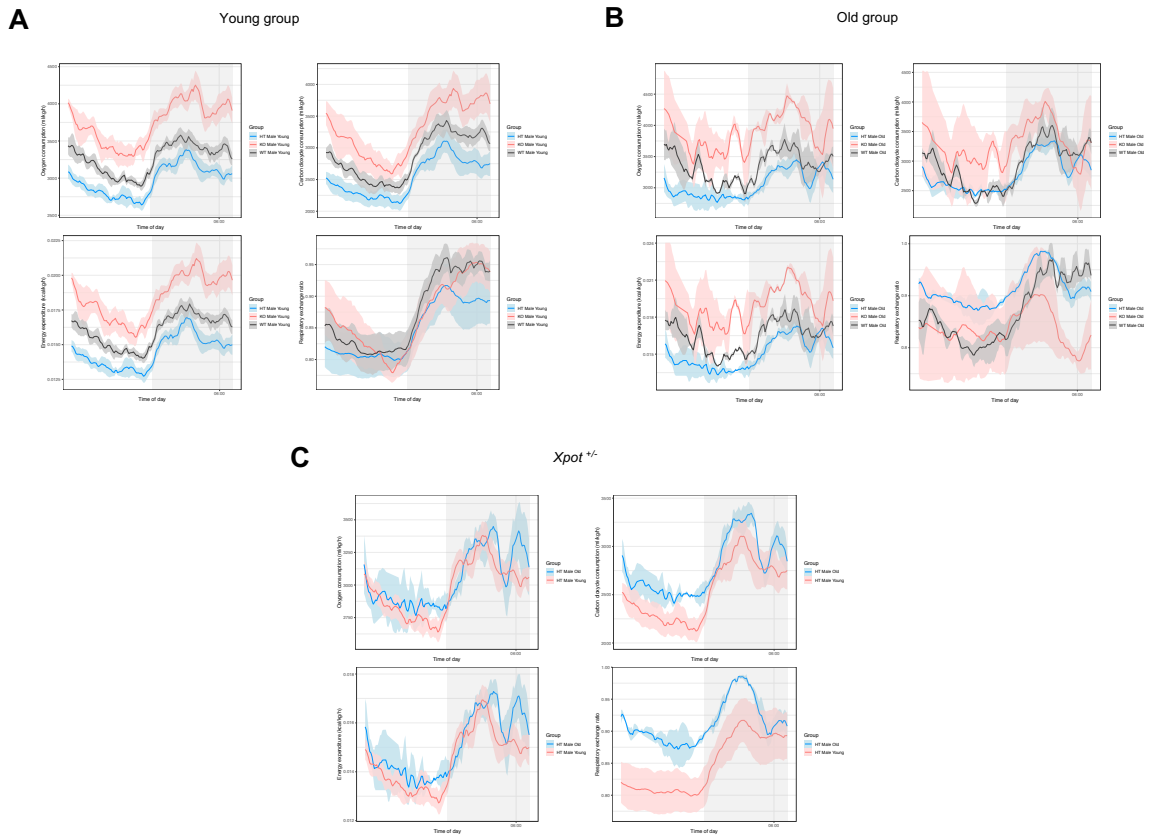

Figure 22. Oxymas assesment of Xpot-deficient mice. Oxygen consumption, carbon dioxide consumption, energy expenditure and respiratory exchange ratio are represented. Two groups (**A**) young mice(4-month-old) and (**B**) old mice (12-month-old). (**C**) Comparation between Xpot$^{+/-}$ young group and *Xpot*$^{+/-}$ old group. For young mice group n= 4 *Xpot*$^{+/+}$, n= 4 *Xpot*$^{+/-}$,n= 4 *Xpot*$^{-/-}$. For old mice group n= 4 *Xpot*$^{+/+}$, n= 4 *Xpot*$^{+/-}$, n= 4 *Xpot*$^{-/-}$.

2.4.2 Coordination assessment of Xpot-deficient mice

Rotarod apparatus consists of a rotating cylinder on which the animal is placed, and it gradually accelerates in speed. The goal of this test is to measure how long an animal can stay on the rotating cylinder before falling off. This procedure allows us to assess the animal's ability to maintain balance and coordination. Animals with good neuromotor function will be able to stay on the rod for a longer time and at higher speeds. Xpot mice of both groups underwent this test for four days after a three-day training period. As shown in the **Figure 23 A**, *Xpot*$^{-/-}$ mice demonstrate reduced endurance in the Rotarod apparatus compared to *Xpot*$^{+/+}$, at both 4 months and 12 months of age. *Xpot*$^{+/-}$ mice exhibit similar endurance as the littermate's control in their younger stages, but this equivalence significatively changes as they age, implying a deterioration of neuromuscular function over time.

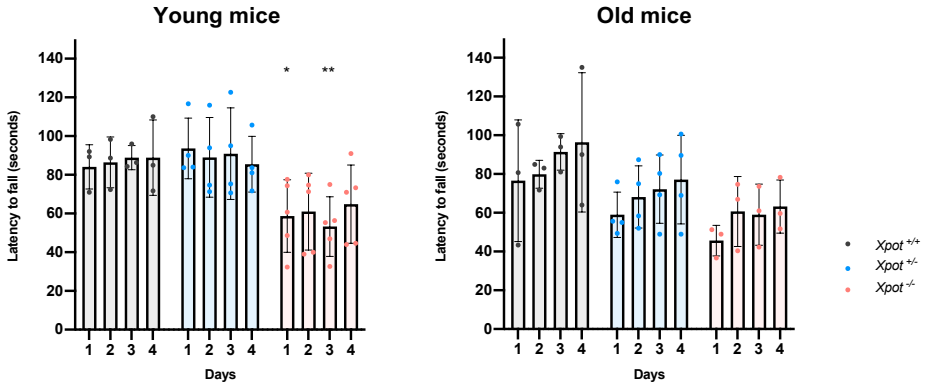

Figure 23. Rotarod assessment of Xpot mouse model. Latency to fall during an increasing speed rotarod experiment of young mice (4-month-old) and old mice (12-month-old). For young mice group n= 3 *Xpot*$^{+/+}$, n= 4 *Xpot*$^{+/-}$,n= 5 *Xpot*$^{-/-}$. For old mice group n= 3 *Xpot*$^{+/+}$, n= 4 *Xpot*$^{+/-}$,n= 3 *Xpot*$^{-/-}$.

2.4.3 Strength assessment of Xpot-deficient mice

Following, by using a specialized grip strength meter, we assessed the muscular strength and grip force of the mice's forelimbs. The procedure was conducted on two different days, with three measurements each one. The mean of these measurements is represented in (**Figure 24)**. To better analyze this data, the force should be normalized to the length of the limb bones, which would require the sacrifice of the animal. This measure was not taken to allow for the continuation of the experiments. However, the results have shown no significant differences in the forelimb strength force between groups.

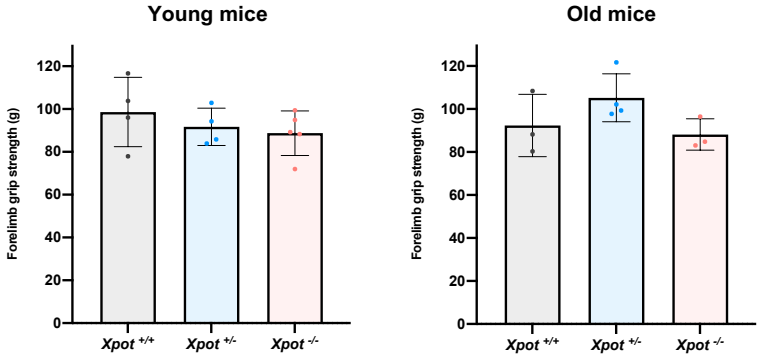

Figure 24. Forelimb grip strength assessment of Xpot-deficient mice. Strength is representing in grams of young mice and old mice group. For young mice group n= 4 *Xpot*$^{+/+}$, n= 4 *Xpot*$^{+/-}$,n= 5 *Xpot*$^{-/-}$. For the old mice group n= 3 *Xpot*$^{+/+}$, n= 4 *Xpot*$^{+/-}$, n= 3 *Xpot*$^{-/-}$.

2.6 Prenatal studies in the Xpot mouse model

When this project was initiated, fully recognizing the significance of the XPOT protein for the proper development and functioning of an individual, the expectation was not to obtain mice with a complete *Xpot* deficiency from the cross of two parental heterozygous mice. Surprisingly, *Xpot*$^{-/-}$ mice were indeed obtained, but with a very low birth rate—only 2.36% of the total newborn pups were completely deficient in XPOT (**Figure 15 A**). This outcome did not fit to Mendelian ratio, where the expected distribution would consist of 25% wild-type mice, 25% homozygous mice with two mutant alleles, and 50% heterozygous mice. To address this phenomenon, we conducted prenatal lethality studies with the primary objective of pinpointing the stage in embryonic development at which the percentage of knockout mice deviated from the Mendelian expectation. This key point thus plays a pivotal role in the murine model's embryonic development.

For this purpose, we crossed multiple pairs of parental *Xpot*$^{+/-}$ mice and monitored for the presence of a plug after coitus. It is important to note that the typical embryonic development period for a healthy mouse from the C57BL6 strain is 19 days. In our initial assessment, conducted 12.5 days post-coitus (dpc), female mice were euthanized, and we proceeded to extract the embryos. Variations in the number of embryos within the uterine horns were observed among the females, with some embryos displaying abnormal size and dark coloration. DNA extraction from these abnormal necropsied embryos was not possible due to the presence of necrotic tissue. The remaining embryos were extracted, and tail biopsies were performed for genotyping purposes. From the experiment involving embryos at 12.5 dpc (E12.5), a total of 31 embryos were analysed, with 45.16% being *Xpot*$^{+/+}$, 41.94% *Xpot*$^{+/-}$, and only 12.9% *Xpot*$^{-/-}$ **(see Figure 25 A).**

Upon noticing a deviation in the percentage of the knockout (KO) genotype at a specific prenatal developmental stage, we decided to study embryos at an earlier stage, specifically at E10.5. Similar to the previous procedure, pairs of parental *Xpot* $^{+/-}$ mice were crossed. However, upon examination, no differences were observed among the fetuses within the uterine horns. A total of 34 embryos were studied, and following genotyping, we found that the proportion of genotypes was as expected: 23.53% *Xpot*$^{+/+}$, 50% *Xpot*$^{+/-}$, and 26.47 % *Xpot*$^{-/-}$ at E10.5 (**Figure 25 A**)

Anatomically, both *Xpot*$^{-/-}$ embryos at E10.5 and E12.5 exhibited smaller sizes compared to wild-type controls and their corresponding heterozygous counterparts on the respective embryonic days. Furthermore, a distinctive characteristic of these knockout embryos was the near absence of fetal liver red colour at E10.5, making it impossible to differentiate from the rest of the structures. This contrasts with wild-type or heterozygous embryos, where a vivid red colour is attributed to the involvement of this fetal organ in premature haematopoiesis. The colour distinction between *Xpot*$^{-/-}$ and *Xpot*$^{+/+}$ and *Xpot*$^{+/-}$ became notably evident at E12.5. The heart in *Xpot*$^{-/-}$ embryos at E12.5 also exhibited greater clarity than in the other genotypes, and eye pigmentation was notably absent. No differences were found between *Xpot*$^{+/-}$ and *Xpot*$^{+/+}$ at any of the developmental stages studied **(Figure 25 B).**

Histopathological studies of the embryos were conducted, and hematoxylin and eosin (H&E) stains revealed a hypoplastic liver in *Xpot*$^{-/-}$ embryos at both E10.5 and E12.5. The fetal livers of these embryos were significantly smaller compared to the rest of their organ structures, which were also smaller when compared to *Xpot*$^{+/+}$ and *Xpot*$^{+/-}$ embryos but in a proportionate manner relative to the rest of the body. Focusing on the fetal liver, a lower number of hematopoietic progenitor cells were found in *Xpot*$^{-/-}$ embryos at both stages, with this characteristic being more pronounced in some *Xpot*$^{-/-}$ embryos at E10.5 where it was difficult to differentiate hematopoietic progenitor cells (**Figure 25 C**).

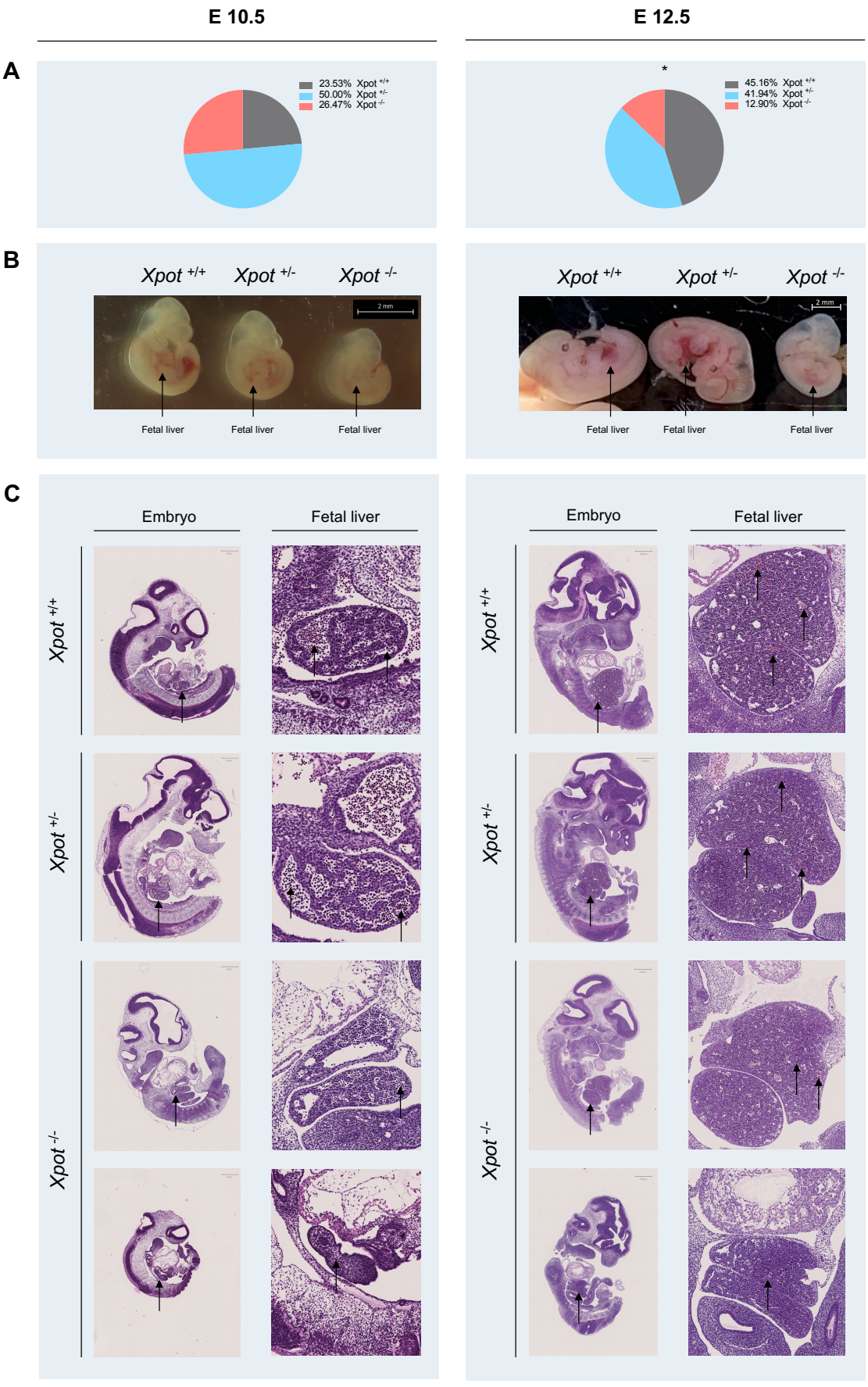
E 10.5
E 12.5
A
23.53% Xpot +/+
50.00% Xpot +/-
26.47% Xpot -/-
*
45.16% Xpot +/+
41.94% Xpot +/-
12.90% Xpot -/-
B
Xpot +/+
Xpot +/-
Xpot -/-
2 mm
Fetal liver
Fetal liver
Fetal liver
Xpot +/+
Xpot +/-
Xpot -/-
2 mm
Fetal liver
Fetal liver
Fetal liver
C
Embryo
Fetal liver
Xpot +/+
Xpot +/-
Xpot -/-
Embryo
Fetal liver
Xpot +/+
Xpot +/-
Xpot -/-

Figure 25. Prenatal study of Xpot-deficient mice. On the left E10.5 is represented, on the right E12.5. (**A**) Percentage of mouse embryo by genotype. 34 E10.5 and 31 E12.5. Chi-square test, * p<0,05. (**B**) Representative image of E10.5 and E12.5 by genotype. The scale bar is present in the figure and with arrows the fetal liver is indicated. (**C**) Representative H&E images from E10.5 and E12.5. The arrow on the embryo indicates the fetal liver, and the arrows on the fetal liver image indicates the hematopoietic progenitor cells. In the case of E10.5 *Xpot*$^{+/+}$ n=3, *Xpot*$^{+/-}$ n=3, *Xpot*$^{-/-}$ n=3. In the case of E12.5 *Xpot*$^{+/+}$ n=4, *Xpot*$^{+/-}$ n=4, *Xpot*$^{-/-}$ n=4.

2.7 Analysis of Xpot role in cancer

Several studies have established a connection between altered Karyopherin expression—mainly elevated protein levels with occasional lower expression—and cell transformation in various types of cancer cells[142]. XPOT overexpression has been demonstrated to correlate with a poor prognosis in breast, ovarian cancers, and mesothelioma[153,154]. In relation to this, tRNAs, the principal cargoes of XPOT, are intimately associated with cell proliferation and cell-cycle control. Changes in their abundance or nucleotide modification levels can have profound effects, leading to aberrant translation, alterations in protein expression, and the onset of disease states, including cancer[97]. Therefore, we found it pertinent to conduct a more comprehensive investigation to decipher the role of XPOT in cancer.

As a first approach, we assessed the mutational status of *XPOT* in various malignancies using a cancer genome database (http://cbioportal.org). Our exploration of *XPOT* mutations covered a curated set of 217 cancer studies, encompassing 70,655 human non-redundant tumor samples and 67030 cancer patients.

We found that *XPOT* exhibits mutations and amplifications in multiple tumor categories, with particular significance in lung cancer, adrenocortical carcinoma, or sarcoma, among others (with a somatic alteration frequency ranging from 17,95% to 0% and with a mean frequency of 3% in all studies). Interestingly, a subset of tumors showed deep deletions, as observed in cases such as colorectal cancer, melanoma, and endometrial carcinoma. Furthermore, structural variants (fusions with *MDM2, LMD3* or *RASSF3* were identified in liver hepatocellular and breast invasive carcinomas, ovarian epithelial and breasts tumors (**Figure 26 A)**.

After conducting research on the type and frequency of mutations occurring along the amino acid sequence of the XPOT protein, it was evident that the majority of mutations were missense. These missense mutations were uniformly distributed across the amino acid chain, with truncating mutations occurring less frequently. Most of these truncating mutations occur at the beginning of the protein, potentially leading to a heterozygous loss of XPOT function. Interestingly, this pattern was particularly prominent in cases of colorectal cancer (**Figure 26B)**.

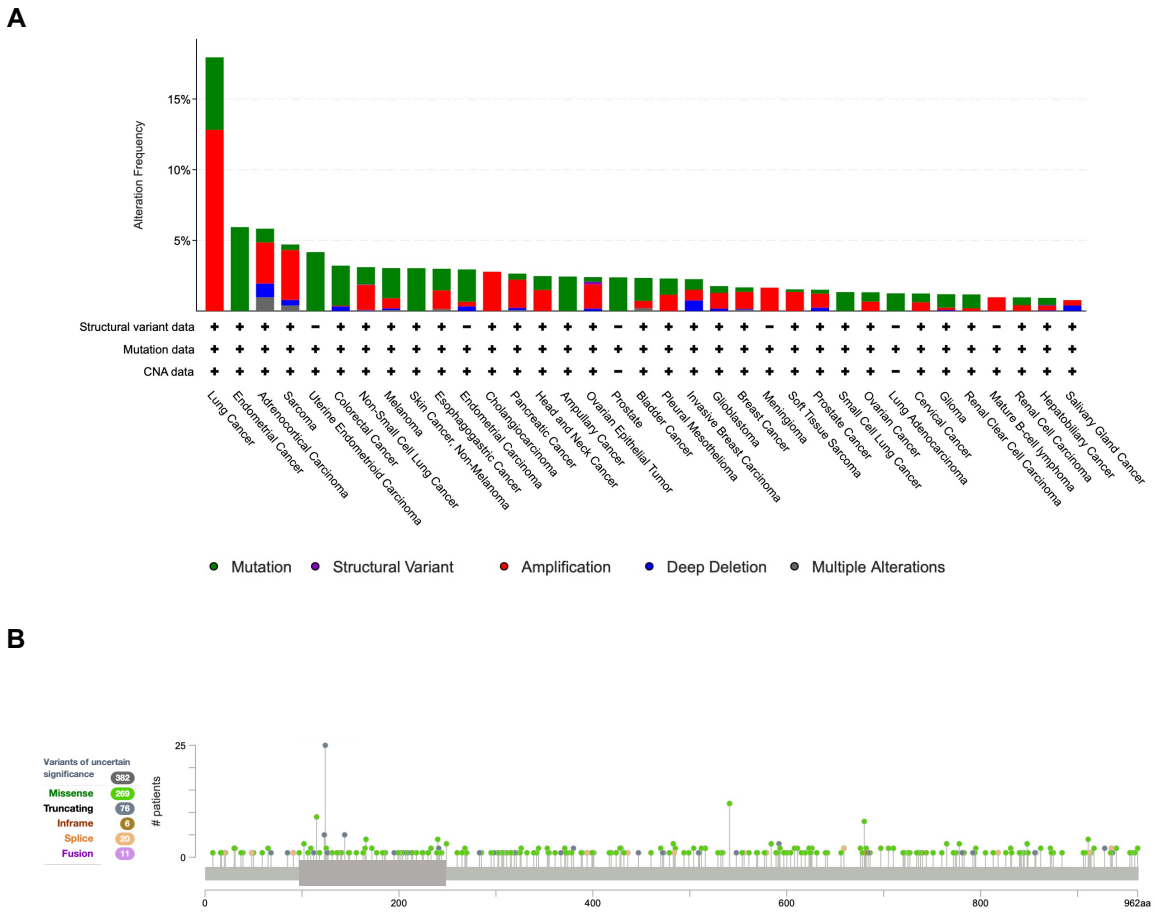

Figure 26 . Alterations in *Xpot* in different types of human tumors. Data were obtained from the cBioportal database, from 217 combined studies with 70655 samples. (**A**) Percentage of alterations in *Xpot* in different types of human tumors. The type of tumor is represented in the X-axis and the alteration frequency in the Y-axis. Green indicates mutation; red, amplifications; blue, deep deletions; purple, structural variants, and grey, multiple alterations. (**B**) Variants of uncertain significance from different patients across the amino acid structure of XPOT. The positions in the protein sequence are reflected in the X-axis, and in the Y-axis represents the number of patients with the mutation. There are 382 different variants of uncertain significance, 269 of them are missense and are represented as green dots; 76 truncating mutations, in grey; 6 inframe variants, in brown; 20 splice variants, in orange; and 11 correspond to fusion variants, represented in purple.

2.7.1 Chemical carcinogenic protocols in Xpot-deficient mice

Considering all this information and noting that XPOT is frequently mutated in lung and colorectal cancer—both of which have a high incidence in the population—we selected them as subjects for our investigation into the significance of XPOT in the generation and progression of cancer.

First, we conducted a lung adenocarcinoma protocol using the carcinogen urethane in *Xpot*$^{+/-}$ and *Xpot*$^{-/-}$ male mice. This carcinogen induces activating mutations in the oncogene KRAS, which resembling the genetic alterations found in human non-small cell lung carcinoma [172]. Urethane was administered intraperitoneally when the mice were 8 weeks old, and we monitored their weight until 7.5 months after the initial urethane administration (**Figure 27 A**). At this point, we collected their lungs for histopathological

analysis, studying the number of tumors and induced dysplasia. Additionally, we analyzed various histological changes in the lung samples, including alterations in tissue structure, the presence of hemorrhagic foci, the inflammatory infiltrate status, the presence of fibrosis and changes in the thickness of the alveolar membrane. We found no significant differences between the two groups in neither of the parameter studied, number of adenomas and carcinomas were similar between both groups (**Figure 27 B-C**). Moreover, there were no significant differences in body weight.

Secondly, to explore the role of XPOT in colorectal tumorigenesis, we conducted a carcinogenesis protocol based on inflammation in 8-week-old females with Xpot $^{+/-}$ and *Xpot*$^{-/-}$ genotypes. This procedure involved the intraperitoneal injection of the chemical carcinogen azoxymethane (AOM), which generates DNA adducts. It was followed by the administration of dextran sulphate sodium (DSS) in the drinking water. DSS was given in three cycles to induce inflammation, with each cycle followed by the administration of normal water (**Figure 27 D**). Consequently, mice developed colitis-associated neoplasms [173]. We monitored the weight of the animals throughout the entire process but did not find any differences. Interestingly, we observed no differences in the incidence of dysplasia or adenocarcinomas between both groups, nor in the size of these malignancy lesions (**Figure 27 E-F**).

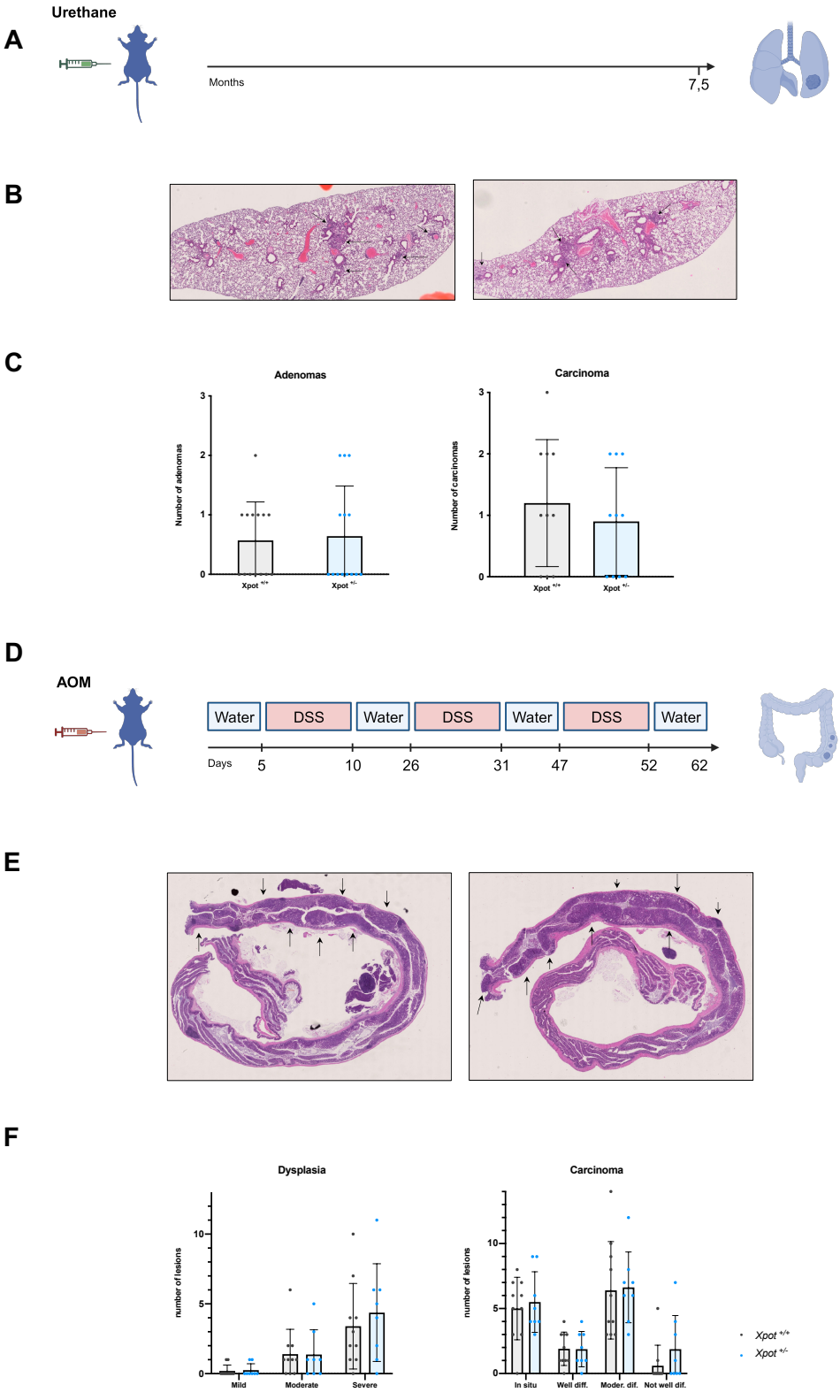

Figure 27. Two carcinogenesis protocols to study Xpot role in caner. (**A**) Diagram representing the lung carcinogenesis protocol. (**B**) Representative images of H&E staining in lung. Arrows indicate carcinomas. *Xpot*$^{+/+}$ n=10, *Xpot*$^{+/-}$ n=10. (**C**) Adenomas and carcinoma counts representation. (**D**) Diagram representing the colon carcinogenesis protocol. (**E**) Representative images of H&E staining in colon. Arrows indicate carcinomas. *Xpot*$^{+/+}$ n=10, *Xpot*$^{+/-}$ n=10. (**F**) Dysplasia and carcinomas counts representation.

2.8 Molecular characterization of Xpot-deficient mice

To gain insight into the molecular mechanism by which the deficiency of Xpot generates such phenotype in mice, we carried out full transcriptome and proteome analysis in liver and colons form *Xpot*$^{+/+}$, *Xpot*$^{+/-}$ and *Xpot*$^{-/-}$ mice. Consequently, we conducted a comprehensive analysis of the murine Xpot model, encompassing both full proteome and transcriptome. Given significant differences in blood glucose and cholesterol levels, we prioritized the liver as the primary metabolic organ for this study. Furthermore, recognizing the potential involvement of Xpot in colorectal cancer (despite our negative results in the carcinogenic protocols) and its high rate of cell regeneration, we also included the colon as a second target tissue for proteomic and transcriptomic studies in these mice.

2.8.1 Proteomic profiling study of Xpot-deficient mice

First, we conducted multiplexed quantitative proteome analysis, utilizing the tandem mass tag (TMT) workflow and high-resolution mass spectrometry, on liver and colon samples from *Xpot*$^{+/+}$, *Xpot*$^{+/-}$, and *Xpot* $^{-/-}$ mice (with three independent samples for each phenotype). The TMT-MS workflow identified only 698 common proteins among the three *Xpot* phenotypes in colon protein extracts, and 749 proteins in livers. The reduced number of identified proteins could be attributed to the absence of HPLC sample fractionation, a decision made to manage study costs.

Due to the limited number of identified proteins in each tissue, the initial statistical analysis did not unveil any significantly altered proteins. Nevertheless, we conducted a Gene Set Enrichment Analysis (GSEA) to identify potential patterns or altered pathways. Gene ontology analysis of preranked proteins for each phenotype revealed significant alterations in biological processes related to protein synthesis, ribosomal biogenesis, and translation, with the ribosome identified as the main altered cellular component. Notably, these alterations were consistent in both liver and colon tissues, underscoring the robustness of the results.

As depicted in **Figure 28 A**, both the heatmap of ribosomal proteins identified in the proteomic study and the volcano plot analysis of ribosomal proteins (**Figure 28 B highlighted in red**) indicate an increase in ribosomal proteins in the livers and colons of *Xpot* knockout mice. Notably, this tendency was also observed in the colons of heterozygous mice. These results suggest an accumulation of ribosomes in these tissues, possibly indicating an alteration of the translational machinery in line with the deficiency of the tRNA carrier protein.

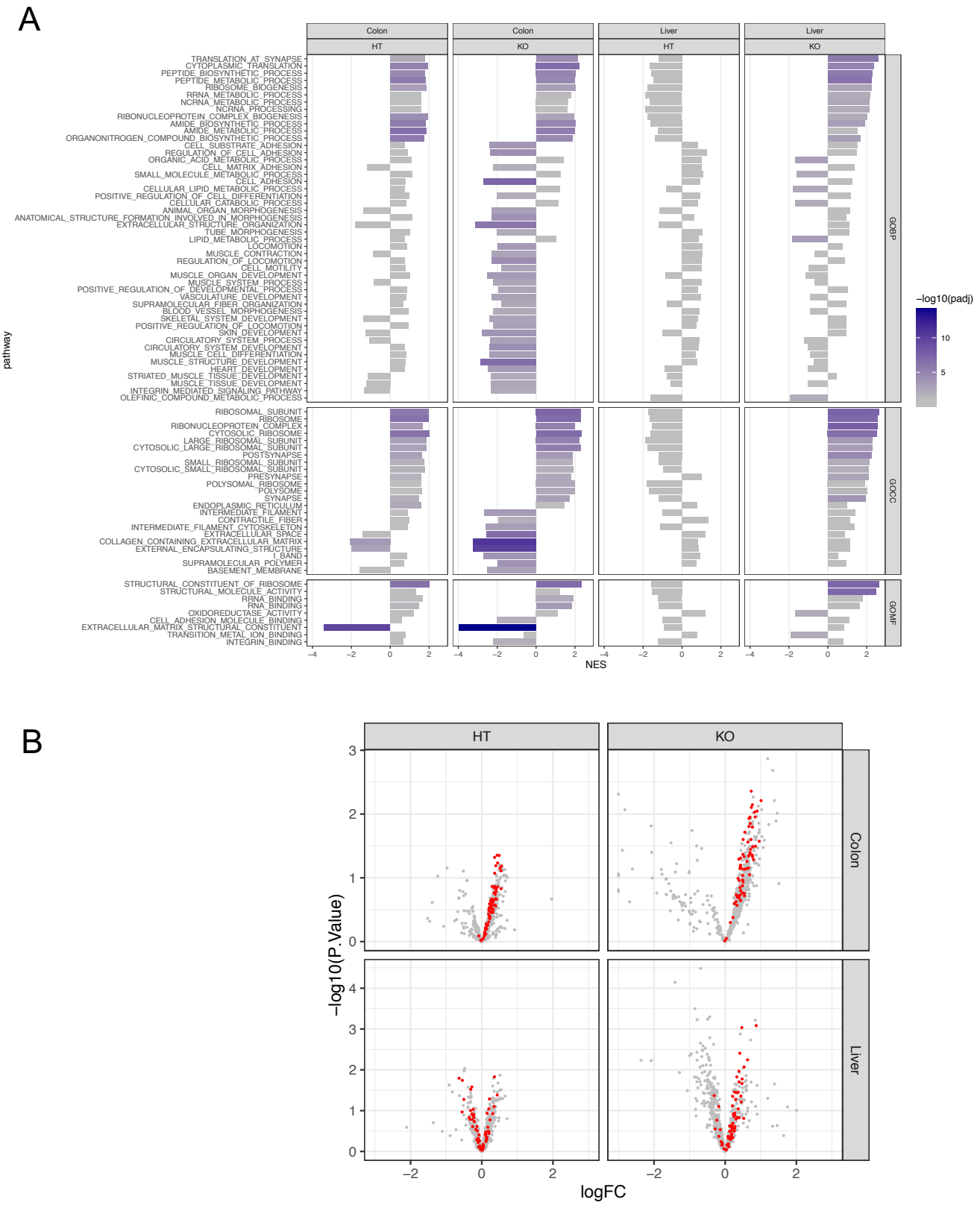

Figure 28. Proteomic analysis of Xpot mouse model. (A) Gene Set Enrichment Analysis (GSEA). (**B**) Volcano plot for differential protein expression analysis. Ribosomal proteins are indicated in red.

2.8.2 Transcriptomic profiling of the Xpot-deficient mice

Secondly, to further investigate and validate our previous findings, we conducted a transcriptomic study on the same tissues from the murine Xpot model used for proteomic analysis. For this purpose, we compared the full transcriptome of liver and colon samples from *Xpot*$^{+/+}$ (n=4), *Xpot*$^{+/-}$ (n=4), and *Xpot*$^{-/-}$ mice (n=3).

The multiple t-test analysis revealed a total of 25 and 71 differentially expressed genes in the livers of *Xpot*$^{+/-}$ and *Xpot*$^{-/-}$ mice, respectively, when compared to wild-type animals (adjusted P-value < 0.05 and log2 fold-change>0.5). In colon samples, we identified 10 and 614 differentially expressed genes, respectively (**Figure 29**). **Figure 30 A** and **Figure 30 B** illustrate the unsupervised hierarchical clustering of the differentially expressed genes in the liver (90 genes) and colon (624 genes), respectively, confirming strong clustering between biological replicates, especially between *Xpot* $^{-/-}$ and *Xpot* $^{+/+}$ in both organs.

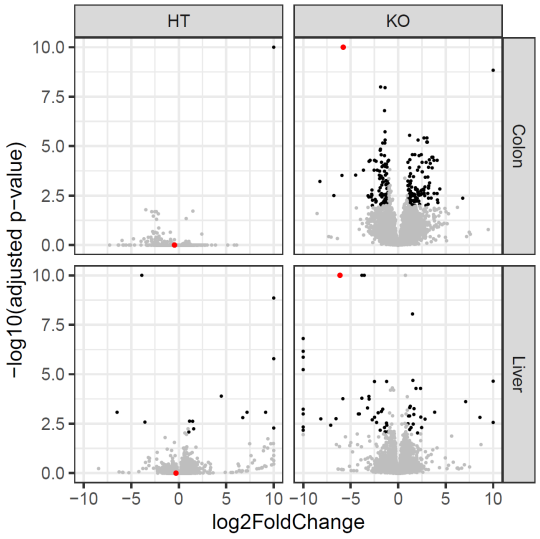

Figure 29. Volcano plot for differential gene expression analysis. X-axis represent the logarithm (base2) of fold change (log2) and Y-axis shown the antilogarithm (base10) of adjusted p-value(p value, -log10). *Xpot*$^{+/+}$ (n=4), *Xpot*$^{+/-}$ (n=4), and *Xpot*$^{-/-}$ mice (n=3).

Surprisingly, despite the abundance of differentially expressed genes in colon samples from *Xpot*$^{+/-}$ and *Xpot*$^{-/-}$ mice, they exhibited no shared differentially expressed genes (**Figure 31 A**). Instead, in both *Xpot* $^{+/-}$ and *Xpot*$^{-/-}$ mouse livers, we identified four upregulated genes (Rsc1a1, Amy2a5, Muc2, and Gm20547) and one downregulated gene (Ighv1-72) (**Figure 31 B**). Notably, Rsc1a1 is particularly relevant as it plays a critical role in the negative regulation of glucose transmembrane transport through the SGLT1 cotransporter in the small intestine. RSC1A1 mediates the deceleration of the release of SGLT1-containing vesicles from the trans-Golgi network[174,175]. Additionally, Amy2a5 encodes pancreatic alpha-amylase 2a5 [176], Gm20547 encodes a C3/C5 convertase of the complement system [177], and Muc2 encodes the oligomeric mucus gel-forming Mucin 2. Mucin 2 provides an insoluble mucous barrier that protects the intestinal epithelium and

is particularly prominent in the gut, where it is secreted from goblet cells into the lumen of the large intestine [178].

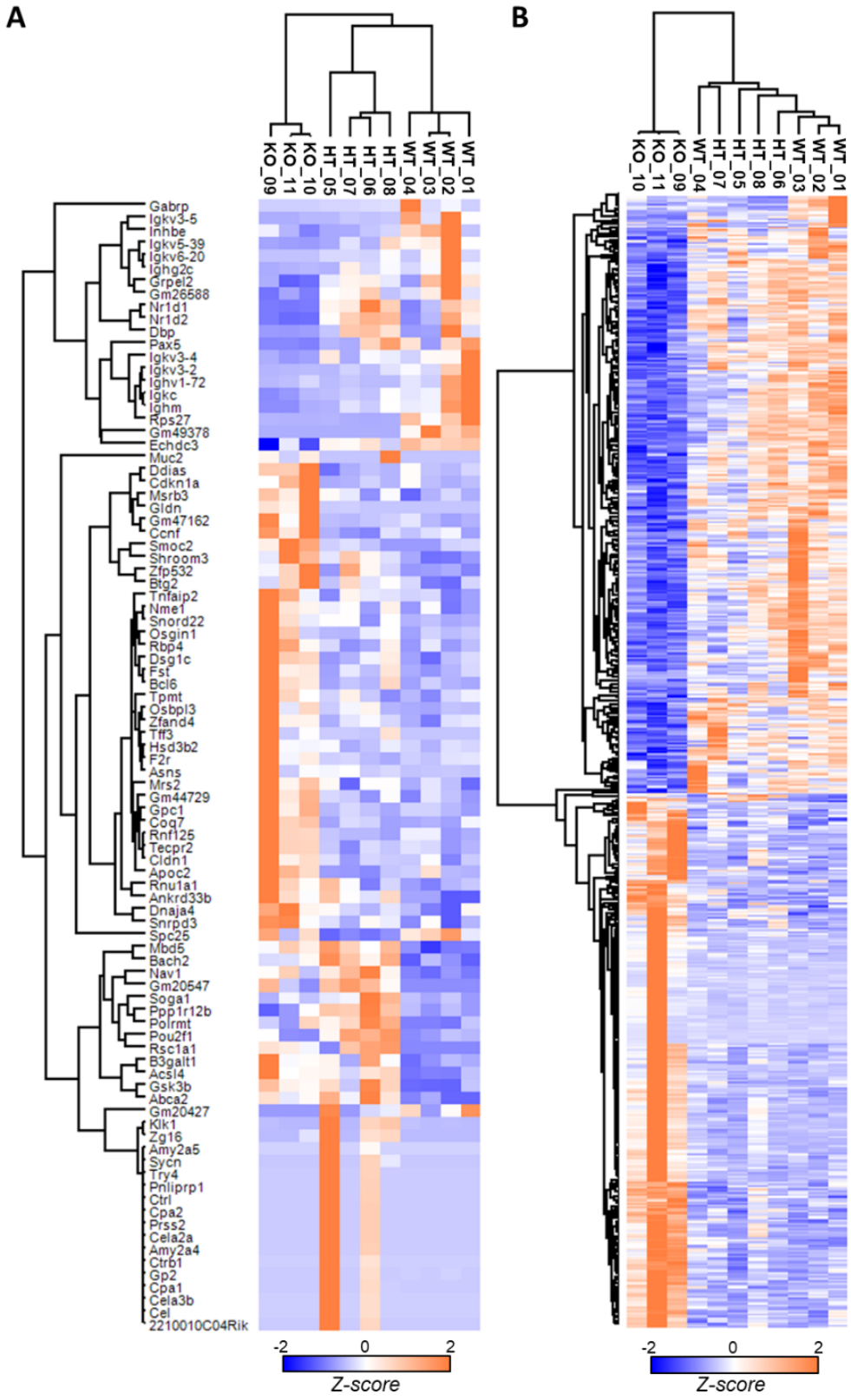

Figure 30. Hierarchical clustering of the differentially expressed genes. (**A**) 90 genes are represented from liver samples. (**B**) 624 genes are represented from colon samples. *Xpot*$^{+/+}$ (n=4), *Xpot*$^{+/-}$ (n=4), and *Xpot*$^{-/-}$ mice (n=3).

Additionally, the heightened expression of *Bcl6* and reduced expression of *Pax5*, along with several *IghC* and *V* genes, in the livers of *Xpot*$^{-/-}$ mice were particularly noteworthy. PAX-5, also known as the B-cell-specific activator protein BSAP, serves as a nuclear transcription factor crucial for the differentiation, development, and proliferation of B-cells [144,179]. Intriguingly, the inactivation of the *Pax5* gene results in the dedifferentiation of mature B cells into progenitor cells in the bone marrow, which subsequently differentiate into activated T cells [180]. On the other hand, BCL6 functions as a transcriptional repressor with a significant role in the formation of germinal centers in both normal and malignant lymphoid tissues. Bcl-6 acts as a master transcription factor, regulating T follicular helper cells (T_{FH} cells), which are essential for the generation of germinal centers in the follicles of secondary lymphoid organs. These centers play a vital role in B cell division and aiding in the fight against infections [181,182].

Moreover, despite the striking differences between the two organs, we identified three commonly differentially expressed genes in Xpot-deficient mice. Notably, we observed elevated levels of *Tnfaip2* and decreased levels of *Nr1d1* and *Nr1d2* in both tissues (**Figure 31 C**). *Tnfaip2* encodes the Tumor Necrosis Factor Alpha-Induced Protein 2, participating in various physiological processes, including inflammation, angiogenesis, cell differentiation, and proliferation [183]. *Tnfaip2* is enriched in the spleen, male mature germ cells, hematopoietic and lymphoid tissues, and its expression can be activated by other cytokines such as IL-lβ, lipopolysaccharide, and interferon-γ. Dysregulation of TNFAIP2 has been reported in various cancers [184,185]. Nr1d1 and Nr1d2, nuclear receptor subfamily 1 group D member 1 (Nr1d1), and nuclear receptor subfamily 1 group D member 2 (Nr1d2) are transcription factors that act as repressors of retinoic acid-related orphan receptor binding elements. They are involved in the control of circadian rhythms during liver aging and lipid metabolism [186,187].

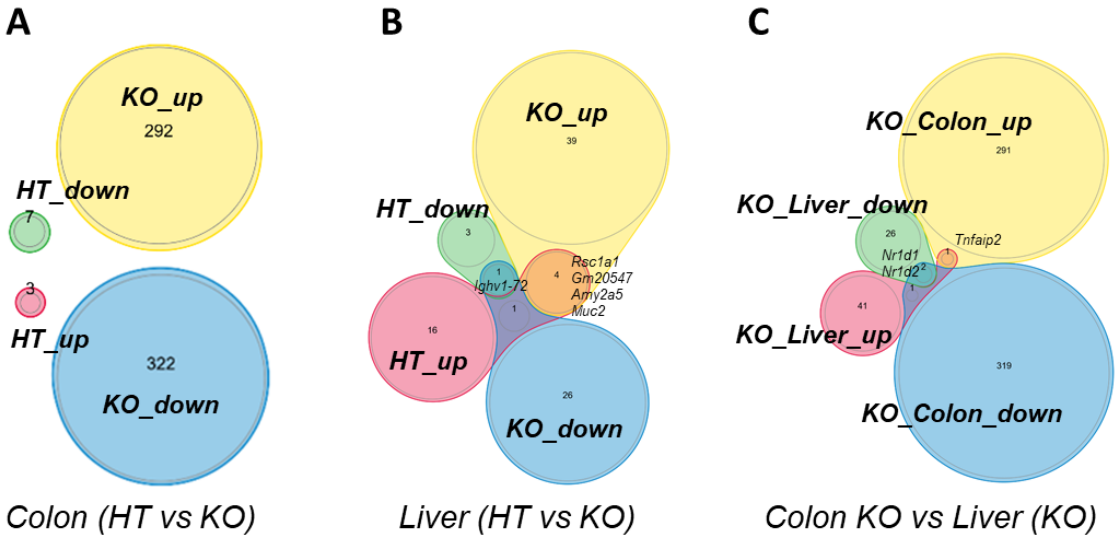

Figure 31. Venn diagram for shared differentially expressed genes. (**A**) Differential gene expression in *Xpot*$^{+/-}$ and *Xpot*$^{-/-}$colons (**B**) Differential gene expression in *Xpot*$^{+/-}$ and *Xpot*$^{-/-}$livers (**C**) Differential gene expression in colon and liver from *Xpot*$^{-/-}$ mice. *Xpot*$^{+/+}$ (n=4), *Xpot*$^{+/-}$ (n=4), and *Xpot*$^{-/-}$ mice (n=3).

To gain a deeper understanding of the altered pathways in these organs, we conducted Gene Set Enrichment Analysis (GSEA) using the Gene Ontology (GO) database. Analysis of preranked proteins through Gene Ontology revealed numerous significantly deregulated pathways in both the liver and colon of Xpot $^{+/-}$ and Xpot $^{-/-}$ mice compared to wild-type animals (**Figure 32**). Firstly, an enrichment in gene sets related to the activation of adaptive immune responses (leukocyte-mediated immunity, T-cell activation, type II interferon production among others) was observed in the colon of *Xpot*$^{-/-}$ animals and in the liver of *Xpot*$^{+/-}$ animals. However, this response was negatively enriched in the liver of *Xpot*$^{-/-}$ animals. It's worth noting that the liver, being an organ highly vascularized, may correlate the decrease of immune-related pathways with the reduction of lymphocytes in peripheral blood. Secondly, an enrichment in gene sets related to the biogenesis of ribonucleoprotein complexes and ribosomes was observed in both the liver and colon of *Xpot*$^{-/-}$ mice, confirming the findings from the proteomic study and emphasizing the robustness of the results. This enrichment was not observed in *Xpot*$^{+/-}$ mice and was even negative in the liver of the latter. Lastly, there was a negative enrichment of genes involved in fatty acid metabolism in the liver of *Xpot*$^{+/-}$ and *Xpot*$^{-/-}$ mice, with a positive enrichment in aerobic respiration and oxidative phosphorylation genes in the livers of *Xpot*$^{-/-}$ mice.

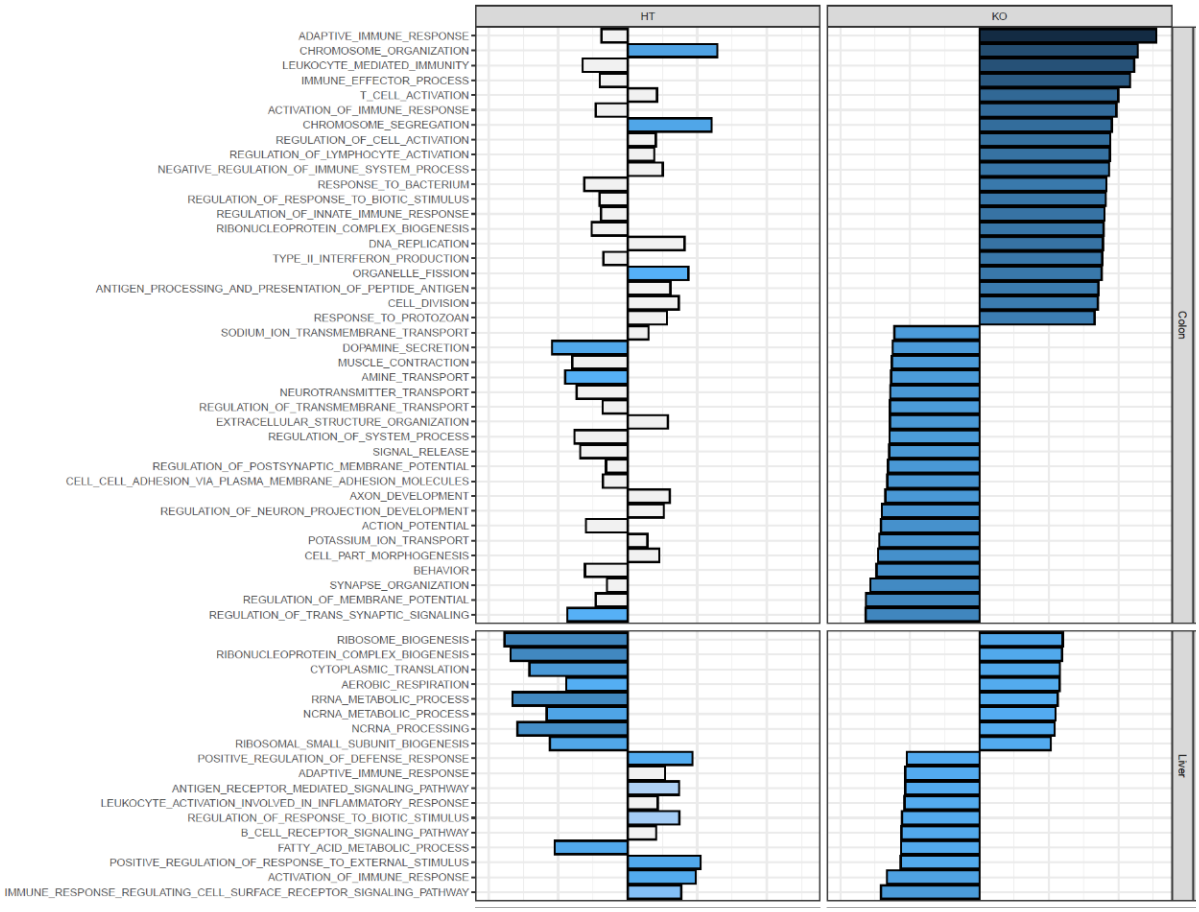

Figure 32. Gene Set Enrichment Analysis (GSEA) using gene ontology (GO). *Xpot*$^{+/+}$ (n=4), *Xpot*$^{+/-}$ (n=4), and *Xpot*$^{-/-}$ mice (n=3).

Finally, although not available at the time of writing this thesis, we conducted a single-cell transcriptomic study of the bone marrow and spleen from these mice. Preliminary results (not shown) seem to align with observations made in bone marrow and spleen cytometry of Xpot knockout mice. We anticipate that these findings will contribute to a more comprehensive characterization of the Xpot-deficient model, aiding in the identification of potential molecular targets of this exportin.

2.9 Analysis of Xpot deficiency *in vitro*

Since its discovery over 25 years ago, much has been learned about Xpot, initially associating it with the transport of tRNAs from the nucleus, where these adapter molecules are transcribed, to the cytoplasm, where they carry out their final function. This situates Xpot as a key player in protein synthesis and the proper functioning of the proteome. Most of the knowledge about this protein has been derived from studies conducted in lower organisms such as *Xenopus* oocytes and *S. cerevisiae*, where it was initially linked to the aging process. However, despite its connection to the emergence of various types of tumors in humans, there is limited information available on how it functions and the role it plays beyond tRNA transport in mammalian cells. Therefore, in this section, we focused on the study of *Xpot* in immortalized primary cells from the murine model and various human cell lines. This involves investigating its expression, along with that of other exportins, and exploring its response to different stress stimuli. Additionally, we will generate cells deficient not only in *Xpot* but also in other karyopherins related to tRNA export to study the trafficking of tRNAs from the nucleus to the cytoplasm.

2.9.1 Exportin expression in cells derived from Xpot mouse model and human cancer cell lines

In order to delve deeper into the molecular mechanisms of the mouse model we proceeded to extract fibroblast from the mice ears, for their subsequent cultivation in cell culture and immortalization using the lentiviral expression vector pLOX-Ttag-ires-TK. We generated immortalized fibroblast from $Xpot^{+/+}$, $Xpot^{+/-}$, and $Xpot^{+/-}$, 3 different mice from each genotype as biological replicates. Western blots analyses were done to study the expression of XPOT, XPO5, XPO1 in immortalized fibroblast, with no differences between the protein expression of the Kaps XPO5 and XPO1 (**Figure 33 A**). To further investigate the relevance of XPOT in the tumorigenesis process specially in hematologic neoplasms, and carry out this process in human cells, we decided to examine XPOT expression, along with that of XPO5 and XPO1, in various tumor human cell lines. This includes cell lines derived from hematologic tumors (**Figure 33 B**), as well as other types

of cancers (**Figure 33 C**). Differential expression levels of XPOT and the other studied exportins were identified through Western blot analyses.

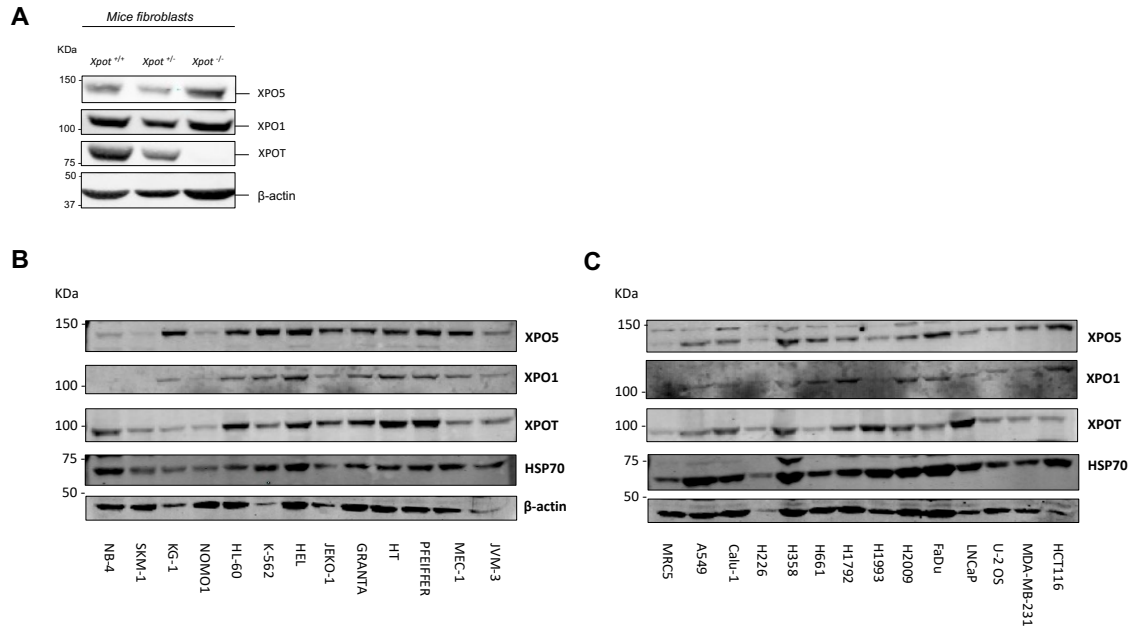

Figure 33. Expression of XPOT, XPO5 and XPO1 different cell lines. (**A**) XPO5, XPO1 and XPOT expression in immortalized fibroblast from Xpot mouse model. Expression of β-actine was used as a control. (**B**) XPO5, XPO1 and XPOT expression in different human hematological tumorigenic cell lines. (**C**) XPO5, XPO1 and XPOT expression in diverse human tumorigenic cell lines.

2.9.2 Generation of different cell lines deficient in Xpot, Xpo5 and Xpo1 by CRISPR Cas9

The development of CRISPR/Cas9 as a genome editing tool has revolutionized biomedical research by offering a relatively simple method, akin to molecular scissor, for selectively removing genes as desired by the user. This system is based on the endonuclease Cas9, which produce double strand breaks (DSBs) in the DNA, guide by a small RNA called single-guide RNA (sgRNA) with homology for a specific region in the genome. These breaks can be repaired through the non-homologous end-joining (NHEJ) mechanism or by homology directed repair (HDR), resulting in the introduction of mutations in the genome or the interruption of the gene sequence, thereby knocking the gene [188]. Taking advantage of this valuable system we generated cells lacking *Xpo5* and *Xpo1* with the aim to study how they will respond when lacking not only *Xpot* but also other exportins related with tRNAs. We decided to carry out this in the immortalized fibroblast obtained from the mouse model *Xpot* $^{-/-}$, besides in *Xpot* $^{+/-}$, and the wild type control *Xpot* $^{+/+}$. In addition to this, we were interested also in studying it in human cell lines, therefore we selected U2OS, K562 and MRC5 cell lines as candidates for CRISPR/Cas9 modification as well.

To conduct these experiments, we designed 3 different sgRNAs with homology for the first exons of mouse *Xpo5* and *Xpo1* genes, to be used in immortalized fibroblast; and other 3 different sgRNAs toward human *Xpot*, *Xpo5* and *Xpo1* genes. Once infected with

the lentiviral expression vector GeCKO v2 containing the genetic information for the Cas9 expression as well as the specific sgRNA and performed the antibiotic selection to be sure that we only work with the Cas9 expressing cells, we conducted Western blot analysis for study the exportin expression. We were unable to knock out XPO1 in any of the cell lines, both those derived from the murine model and human cell lines (**Figure 34 A and C-D**). Contrastingly, although not completely, we were able to knock out XPO5 in both human cell lines K562 and MRC5 (**Figure 34 E-D**), as well as in the murine fibroblast, even when lacking XPOT.

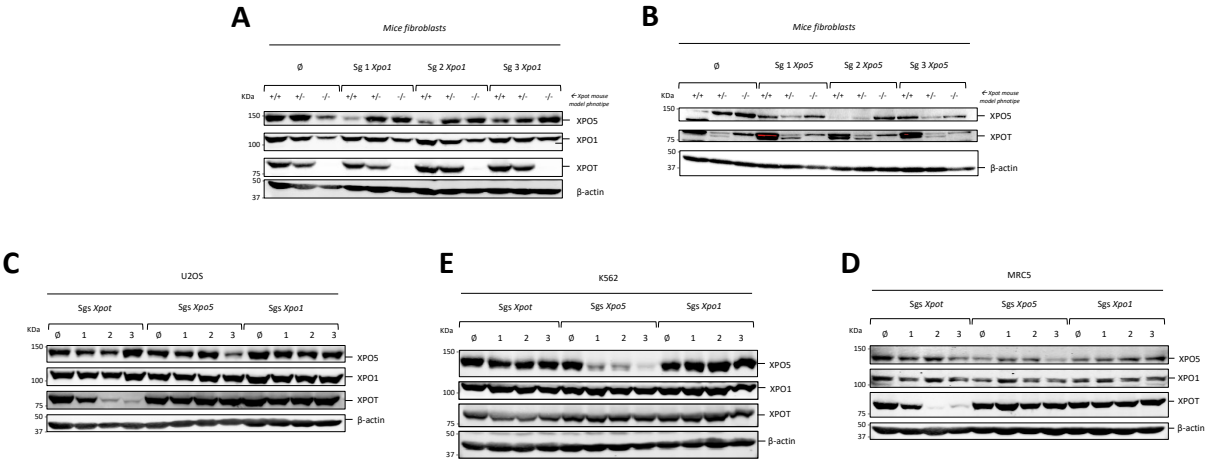

Figure 34. Expression of XPOT, XPO5 and XPO1 in CRISPR-Cas9 murine immortalized fibroblast and cell lines. (A) Inmortalized fibroblast from Xpot mouse model, infected with 3 different sgRNAs with homology to *Xpo1* sequence. (B) Immortalized fibroblast from Xpot mouse model, infected with 3 different sgRNAs with homology to *Xpo5* sequence (C) U2OS cell line infected with different sgRNAs against *Xpo1, Xpo5* and *Xpot.* The same sgRNAs where used in (D) K562 cell line and (E) MRC5 cell line.

Considering that in budding yeast, the absence of the Xpot orthologous gene, Losp1, leads to the accumulation of tRNAs in the nucleus, we aimed to investigate the cytoplasmic/nuclear localization of tRNAs in the fibroblasts derived from the Xpot mouse model. To address this study, we initially separated the cells into two fractions, nuclear and cytoplasmatic, using a detergent-containing buffer. Subsequently, through the Northern blot technique and the use of different probes targeting specific tRNAs, we could examine their presence in both cell extracts. Furthermore, this study was conducted on tRNAs which do not undergo the splicing process and those that do, being able to study a possible disruption of the tRNA maturation. In Northern blots from spliced tRNAS, was possible to observe the pre-tRNA, referring to the tRNA still with the intron, the mature tRNA, which has already undergone the splicing process, and in some cases, a smaller-sized tRNA fragment corresponding to the intron. The small nuclear RNA U6 was used as a loading control in all cases. Prior to conducting the Norther blot analysis, a Western blot was performed on both extract samples. Antibodies against lamin A and C, proteins that typically reside in the nucleus, were used, as well as α-tubulin, a protein that typically remains in the cytoplasm. This approach served as a checkpoint to prevent cross-contamination between the extracts (**Figure 35 A**). Finally, no apparent differences

were found when comparing nuclear extracts among genotypes and cytoplasmic extracts as well (**Figure 35 B-E**). Surprisingly, we could observe the presence of pre-tRNAs in cytoplasm extracts, in control *Xpot*$^{+/+}$ cells, *Xpot*$^{+/-}$ and *Xpot* $^{-/-}$, although without differences in amount between genotypes (**Figure 35 F-G**).

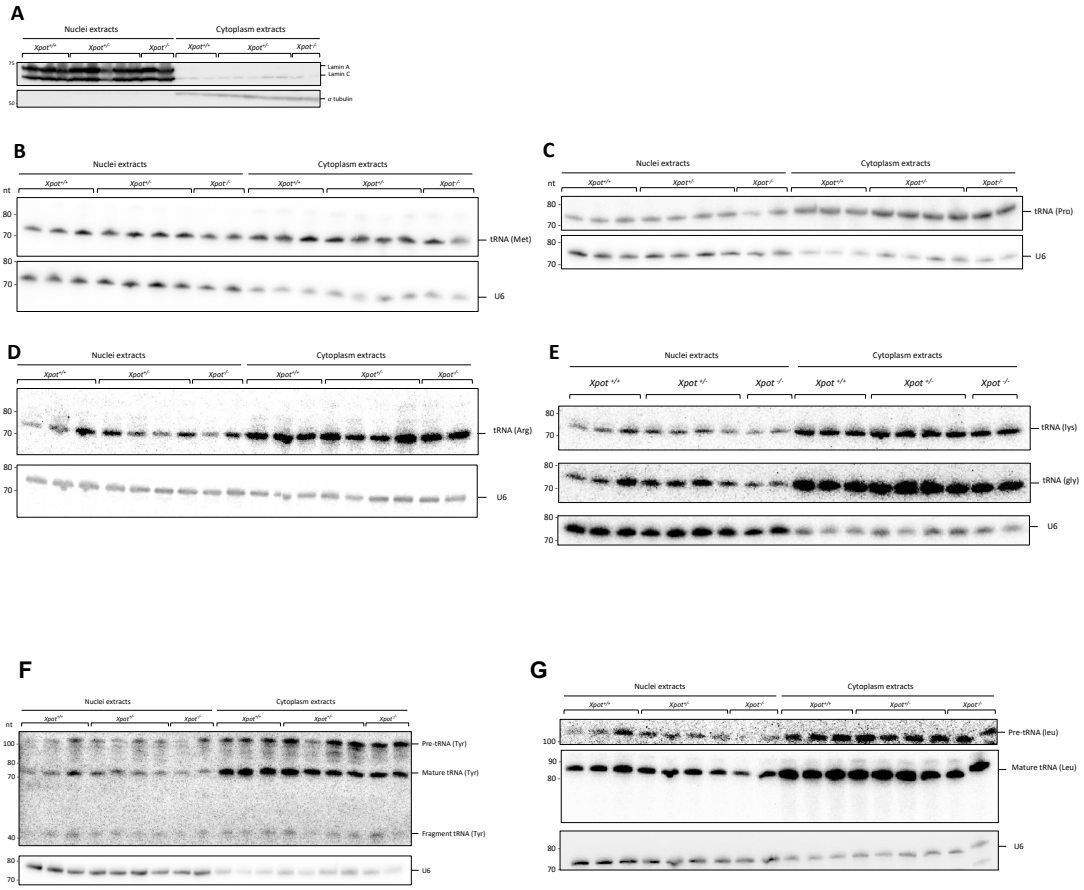

Figure 35. tRNA transport study of different tRNAs by northern blot analysis. (**A**) Western blot against lamin A/C and tubulin to guaranty a proper cytoplasm and nuclei extracts separation. Northerns blots against tRNAs that does not suffer splicing (**B**) tRNA-methionine (Met), (**C**) tRNA-proline (Pro), (**D**) tRNA-arginine (Arg) and .(**E**) tRNA-lysine (Lys). (**F**) tRNA-tyrosine (Tyr) and (**G**) tRNA-leucine (Leu). As a control snRNA U6 is used.

2.9.4 tRNA transport profile in immortalized fibroblast from Xpot-deficient mice and lacking Xpo5 by CRISPR/Cas9 system

To investigate the role of other exportins in tRNA trafficking from nucleus to cytoplasm, and together with XPOT, we selected double knockout fibroblast in both *Xpot* and *Xpo5* to conduct the Northern blot analysis. Since we were unable to achieve knockout cells for *Xpo1,* this exportin was excluded from the study. Additionally, human cell lines were not included in these analyses due to the unavailability of double-knockout *Xpo5* and *Xpot* cells. Therefore, as previously said, our focus was on murine fibroblasts lacking *Xpo5* and *Xpot.*

Curiously, the results revealed an elevation of mature tyrosine tRNA in the nucleus extracts from the double knockout cells compared to Xpot$^{+/+}$, *Xpot*$^{+/-}$ and *Xpot*$^{-/-}$ nucleus extracts (**Figure 36 A**). *Xpot*$^{+/+}$-*Xpo5*$^{-/-}$ fibroblasts, also exhibited an elevation in mature tRNAs in nucleus when compared with *Xpot*$^{-/-}$ cells, but it was not as pronounced as when both exportins were lacking. Nucleus extracts from *Xpot*$^{+/-}$-*Xpo5*$^{-/-}$, also showed a similar increase of mature tRNAs, though not as high as in the double knockout. Furthermore, concerning pre-tRNAs, there was a similar increase to that of mature tRNAs in the nucleus when both exportins were deficient, and also in *Xpot*$^{+/-}$-*Xpo5*$^{-/-}$ extracts. Surprisingly, this elevation was also observed in cytoplasm extracts. All these results were quantified and represented in bar graphics (**Figure 36 B**).

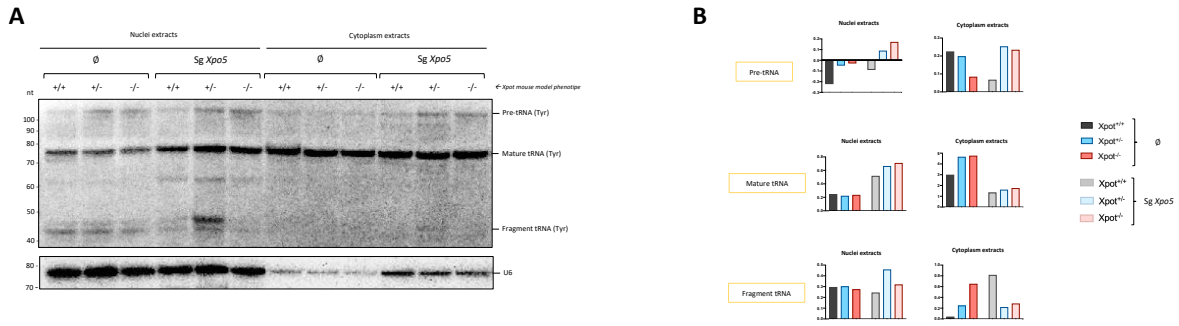

Figure 36. Transport profile of tRNA-Tyr in immortalized fibroblast from Xpot mouse model treated with CRISPR/Cas9 to delete Xpo5. (A) Northern blot using U6 as a control. (B) Quantification, data relativized to the control U6.

DISCUSSION

Most living organisms can function properly in the face of internal and external continuous changes because of rich networks of regulatory mechanisms. This holds true at all levels of organization, spanning from gene networks to cellular biochemistry, from tissue and organ properties to behavior of the whole organisms. The harmony between these networks is what enables an individual to be healthy. Because no system exists in isolation, the health of an organism is dependent on how well all the systems of the body function together to execute homeostatic control. In this sense, the disorganization of health-preserving circuits implies common patterns in disease pathogenesis. Thus, delving deeper into the biology of physiological health could complement our understanding of disease and expand the scope of new therapeutic approaches [189,190].

Proteome stability is an essential requirement for a cell to maintain a healthy status. Sustaining a healthy proteome poses a lifelong challenge for an organism; however, protein homeostasis, or proteostasis is achieved through a conserved network of quality control pathways. These pathways orchestrate the biogenesis of correctly folded proteins, prevent proteins from misfolding, and remove potentially harmful proteins through selective degradation. Nevertheless, the proteostasis network has a limited capacity and decays with age. Its collapse deteriorates cellular functionality and organismal viability, leading to metabolic, oncologic, or neurodegenerative disorders [8,191].

Disruption of general proteostasis accelerates aging. For example, the administration of advanced glycation end products (AGEs) or lipofuscin (an aggregate of covalently cross-linked proteins, sugars, and lipids) to *Drosophila melanogaster* results in the accumulation of AGE-modified and carbonylated proteins, leading to diminished healthspan and lifespan [192]. Loss of the protease ZMPSTE24 abolishes the normal proteolytic maturation of the protein prelamin A, inducing a progeroid syndrome in mice characterized by a substantial reduction in lifespan [193]. Additionally, mutations in RPS9, promoting error-prone translation, cause premature aging in mice [194]. On the other hand, experimental amelioration of proteostasis has demonstrated its potential to retard the aging process. For instance, intranasal application of recombinant human HSP70 protein in mice has been shown to enhance protesasome activity, reduce brain lipofuscin levels, improve cognitive functions, and extend lifespan [195]. In nematodes and flies, the enforced overexpression of isolated proteasome subunits improves proteostasis, increasing lifespan [196]. These findings underscore the intricate relationship between proteostasis modulation and the aging trajectory.

Genomic instability and oxidative stress can lead to increased production of damaged and/or dysregulated proteins in cancer cells [7]. To manage the resulting proteotoxic stress, cancer cells rely on sophisticated protein quality control mechanisms to maintain a proper protein homeostasis for survival and growth. For instance, numerous HSPs have been reported to be overexpressed in a wide range of cancers [16]. The overexpression of HSP90 can downregulate E-cadherin and promote epithelial mesenchymal transition, a key step in tumor metastasis [197]. Autophagy is believed to play

a crucial role in promoting cancer cell survival and growth in advanced cancers by providing substrates for metabolism through the intracellular recycling of damaged proteins. Conversely, the regulation of protein homeostasis not only provides benefits to cancer cells but also plays a detrimental role. Autophagy is considered a tumor suppressor mechanism in the early phases of tumorigenesis, inhibiting tumors by removing oncogenic protein substrates, toxic unfolded proteins, and damaged organelles, thereby maintaining genomic stability [198]. Furthermore, studies indicate that multiple proto-oncogenic proteins can be degraded by the UPS, functioning to suppress cancer growth and progression [199].

In the present Doctoral Thesis, we have focused on investigating the protective role of protein homeostasis during the aging process, along with its fundamental function as a safeguard against the development of neoplasms. This exploration, conducted by the generation of the two mice model previously explained, has been guided by preceding studies in lower organisms. While many aging studies have primarily focused on non-vertebrate model organism, such as yeast (*S. cerevisiae*), worms (*C. elegans*) and fly (*D. melanogaster*) [200], it is essential to acknowledge that certain important aspects of human aging and associated diseases, such as cancer, cannot be faithfully recapitulated in invertebrate models as they lack specific organs and systems. These consequences are highlighted in our presented work. The deficiency of AIP-1 in *C. elegans* results in a reduced lifespan phenotype due to the accumulation of misfolded proteins within cells [39]. Guided by these results, our laboratory previously generated an AIRAPL deficient mouse model, with the principal aim to study this reduction in lifespan caused by proteostasis imbalance. The generation of this mouse model finally led to associating AIRAPL as a key regulatory factor in neoplastic transformation within the hematopoietic compartment [42]. On the other hand, deficiency of Xpot ortholog Losp1 in *S. cerevisiae*, robustly extended its lifespan [155]. However, when extrapolated to higher organisms, the same correlation does not exist, and as is the case here, the opposite may occur.

Proteasomal adaptation to environmental stress links resistance to proteotoxicity with longevity in *C. elegans*. Aip1 was discovered to be induced under exposure to arsenicals, maintaining proteostasis through the degradation of misfolded protein by the UPS [40,41]. The ability of Aip1 to facilitate substrate access to the proteasome remains consistent under basal conditions, responding not only to the effects of arsenic stress but also effectively managing the expression of misfolding-prone proteins. Hence, its deficiency leads to the accumulation of misfolded proteins throughout the worms life, resulting in a diminished lifespan of the nematodes [39]. Mammals possess two genes encoding Aip1 proteins, with *ZFAND2A* encoding AIRAP and *ZFAND2B* encoding the constitutively expressed paralogue AIRAPL. While both proteins share the ability to promote substrate accessibility to the proteasome's catalytic site, AIRAPL exhibits additional features absent in AIRAP. These include the C-terminal CaaX motif, which facilitates membrane association and targets the protein to the ER, UIMs that recruit polyubiquitinated proteins to AIRAPL, and a capacity for regulated proteasomal association requiring yet uncharacterized features of the protein's C terminus. In *C.*

elegans, the *aip1* gene encodes a protein with the structural features of AIRAPL, featuring a measure of basal expression further induced by arsenite. The worm gene therefore incorporates features of both AIRAP and AIRAPL, a pattern observed in most other animal species. The splitting of the ancestral *aip1* gene into an inducible AIRAP and a constitutively expressed AIRAPL appears to be a relatively recent evolutionary feature, primarily limited to mammals.

In mice, the deficiency of *Zfand2b* results in premature death. Our studies shown an average lifespan of 567 days for AIRAPL deficient mouse model, compared to the 751 days observed in the control wild type mice. In contrast, *Zfand2a* deficiency does not causes a reduction in lifespan, being the average quite similar to the control. This difference may be attributed to the differences in the expression of both genes. As mentioned earlier, AIRAPL is constitutively expressed, and is deficiency results in proteostasis impairments. Conversely, AIRAP is expressed only under stress conditions, so its deficiency will not be as notable unless cellular stress is induced. No significant differences in lifespan were found in AIRAPL knockout mice compared to the double knockout. In a similar manner, it could be possible to explain the neoplastic phenotype characterizing AIRAPL deficient mouse, and the absence such a phenotype in the AIRAP deficient mouse. But when both proteostasis factors are lacking, the white blood cell count increases much more than when only AIRAPL is lacking.

Through this work we aimed to comprehensively characterize neoplastic transformation in the hematological context, providing a deeper understanding of the myeloproliferative neoplastic process in the mouse model. For this purpose, we conducted the generation of a cytometry panel to be performed on a spectral cytometer. Utilizing 20 markers, we were able to distinguish a total of 13 different progenitor cell populations, with a specific focus on the myeloid lineage due to the myeloproliferative phenotype of the subject of our study. Additionally, we identified a total of 10 effector cell populations.

Our study serves as a compelling demonstration of the oncogenic relevance of proteostasis deregulation in hematopoietic cells. While many studies on the molecular mechanisms controlling HSC homeostasis have focused on analyzing genetic and epigenetic alterations of key oncogenes and tumor suppressors, as well as assessing the signaling and transcriptional changes induced by these genomic damages, our findings present a different perspective. Specifically, our research reveals that the loss of not only the proteostasis factor AIRAPL but also, in conjunction with AIRAP, contributes to the transformation of myeloid cells. This provides causal evidence highlighting the crucial role of proteostatic processes in regulating the quiescence, proliferation and differentiation of HSCs, which finally contribute to maintain normal adult hematopoiesis.

Deletion of Losp1 in budding yeasts significantly increase their lifespan, due to the retention tRNAs in the nucleus. As molecules responsible for decoding the genetic code, tRNAs need to be located in the cytoplasm to be accessible to ribosomes, where protein synthesis occurs. In *S. cerevisiae,* if the principal transporter of tRNAs is lacking, most of these molecules remain trapped in the nucleus [155], making them inaccessible to ribosomes and consequently reducing protein synthesis. It is widely known that lowering translation, either through mutations or pharmacological agents, is a geroprotective mechanism that extends lifespan across taxa [201–203]. To illustrate this, the reduction of ribosomal proteins or translation-initiation factors levels has been shown to increase lifespan in *C. elegans* [204]. The precise mechanism through which reducing translation impacts lifespan remains unclear; one possibility is that attenuating protein synthesis extends lifespan because the normal process of translation may induce some type of damage that accelerates aging. While this is a conceivable explanation, it appears unlikely, given the strong selective pressure for the beneficial aspect of protein synthesis. Alternatively, it is plausible that the act of reducing translation triggers a cellular response that extends lifespan. Consequently, animals with reduced translation rates may live longer due to initiating a stress response, enhancing their ability to prevent or repair damage that normally accelerates aging [205]. Further investigation is needed to clarify this uncertainty. However it is known that not all translation perturbations exert their effects on lifespan in the same manner, so they should respond to different mechanism [204]. Towards the generation of Xpot null model, we aimed to further investigate whether the deficiency of XPOT in mice would have similar effects on lifespan as observed in budding yeast, either through the accumulation of tRNAs within the nucleus or via other mechanisms.

When we embarked on this project, we hypothesized that haploinsufficiency of *Xpot* in mice could have some impact on aging. We did not anticipate the generation of fully deficient Xpot animals due to the critical importance of this protein in translation, being Xpot the principal transporter of tRNAs, and high translation rates are necessary during embryonic development. Several studies underscore the significance of molecular trafficking through NPC for the proper organism development [58]. Diverse mouse models deficient in Nups have been reported to exhibit embryonic lethality. Examples include mouse models deficient in Nup155 [206] or Nup133 [207], key molecules involved in the nucleoplasmic transport of proteins and RNAs. Additionally, the model deficient in RanBP2 exhibits reduced size and impaired glucose metabolism when in heterozygosity, but when the deficiency affects both alleles, it results in embryonic lethality [208].

Taking this into consideration, it was surprising when we observed that Xpot null model was viable, although with a birth rate that did not correspond to the expected. Interestingly, we were able to observe differences within the small population of Xpot-deficient mice in term of sex, obtaining a significantly lower number of females compared to males. This observation may suggest a potential connection between this protein and hormonal development. From the day of birth and throughout their development, *Xpot*$^{-/-}$ mice are smaller than wild type, exhibiting generalized hypoplasia in all their organs,

highlighting the significance of Xpot in the proper development of the organism not only during embryogenesis but also during the adult stage, which ultimately translates into premature death characterizing this murine model. In support of the aforementioned, Xpot null mice exhibited an unhealthy appearance despite displaying seemingly normal behavior. Contrary to our initial hypothesis, no differences in terms of lifespan were observed when the protein deficiency occurred in heterozygosity. No differences in body weight or physical appearance were found, being impossible to visually distinguish a heterozygous mouse form a wild type one.

Biochemical studies revealed a potential relationship between Xpot and cholesterol as well as glucose metabolism, later supported by liver RNA sequencing. In *Xpot* $^{-/-}$ mice, glucose related pathways were found to be disrupted, with key genes *Rsc1a1,* or *Muc2* being upregulated. Upregulation of *Rsc1a1* is especially relevant as it plays a crucial role in the negative regulation of glucose transmembrane transport. Furthermore, a negative enrichment of genes involved in fatty acid metabolism was found in the liver of *Xpot*$^{-/-}$ mice through the GSEA analysis. This finding could explain the low levels of cholesterol in the serum of *Xpot*$^{-/-}$ mice.

The relevance of Xpot deficiency in hematological disorders was initially assessed through the results obtained from histopathological studies. Anatomical and histological examinations were performed in various organs, although alterations were only found in spleen and liver. Despite the fact that hematopoietically active areas should not be present in an adult spleen, several foci with hematopoietic activity were observed, along with a high number of megakaryocytes, indicating extramedullary hematopoiesis in *Xpot*$^{-/-}$ mice. Additionally, liver alterations were not associated with hepatocyte structure but, surprisingly diverse areas of inflammatory infiltration were identified. This was further supported by the information obtained from RNA sequencing, which highlighted inflammatory response-related pathways as the most altered in liver.

Flow cytometry analyses in peripheral blood, bone marrow, and spleen supported the observation that the Xpot deficient mouse model exhibited hematological abnormalities. Among the most affected populations in all three compartments were B lymphocytes, with a significant reduction in their numbers in the compartments studied. B lymphocytes play a pivotal role in adaptive immunity, contributing to antibody production, antigen presentation and the establishment of immunological memory. The RNA sequencing analysis in the liver, which encompassed not only hepatocyte transcriptomics but also information about all blood cells irrigating the organ, revealed a substantial reduction in the levels of several immunoglobulins such as IghM, Ighg3, Ighg2c, Ighkv3 and Ighv1. Additionally, key genes associated with B lymphocyte expansion were found to be altered in the liver transcriptomics analysis. If we extrapolate these data to the hematological context, it could be possible to understand better and generate hypothesis about the reduction in B cell population numbers. Notably, Bcl6 expression was observed to be significatively high, while Pax5 expression levels were drastically decreased. Bcl6 acts as a transcriptional repressor crucial for preventing

premature activation and differentiation of B cells in the germinal centers of lymphoid organs [179], while Pax5 is essential for committing lymphoid progenitors to the B lymphocyte lineage [180]. These alterations could explain the drastic reduction in B cells observed in the spleen, bone marrow and peripheral blood. However, transcriptomic analyses were not performed in these compartments, which would be essential to affirm the aforementioned findings. On the other hand, the *Xpot*$^{+/-}$ spleen and peripheral blood exhibit contrasting patterns, with elevated levels of B lymphocytes, suggesting a different role of the protein when in haploinsufficiency.

An elevation of the total CD3^{+} cell count was found in *Xpot*$^{-/-}$. We could attributethis increase in the three compartments studied to a rise in the CD4^{+} subgroup. This is supported by the observation that, also within the CD3^{+} cell population, the levels of CD8^{+} are diminished, while CD4^{+} cells are increased. This elevation of CD4^{+} could be explained by the increased expression of Bcl6, which is a master regulator of follicular CD4^{+} T cells [181]. The increase in NK cells in the peripheral blood of *Xpot* $^{-/-}$ mice may be associated with an elevated inflammatory response, along with the elevation of most myeloid cells in the spleen. It is noteworthy that nearly all studied myeloid populations are heightened in the spleen of Xpot null mice, emphasizing elevated levels of inflammatory and intermediate monocytes. Patrolling monocytes, which exhibit an anti-inflammatory profile, were found to be significantly reduced in the spleen of *Xpot*$^{-/-}$ mice, further supporting the idea that an elevated inflammatory response is occurring in the Xpot mouse model. Additionally, eosinophils are elevated, suggesting a potential autoimmune response, although further studies should be conducted to confirm this with certainty.

To gain better understanding of the developed murine model and to investigate the gene and protein expression profiles associated to *Xpot* loss, RNA sequencing and proteomic analysis were conducted. Liver samples were selected to carry out these studies due to the metabolic relevance of this organ to the entire organism. The colon was chosen to further validate the data obtained in the liver and because of the existence of patients with colon cancer and a loss of function in *Xpot* gene. Interestingly, the expression of various genes related with the inflammatory response was altered. This, as discussed earlier, along with the elevation of certain immune cells and the inflammatory infiltrate found in the liver, supports the idea that this mouse model exhibits generalized inflammation. This inflammation would not be limited to the liver but also extend to other organs such as colon. We observed elevated expression levels of *Tnfaip2* in both tissues. *Tnfaip2* which encodes the Tumor Necrosis Factor Alpha-Induced Protein 2, plays a pivotal role in the inflammatory process, as well as angiogenesis, cell differentiation and proliferation. This finding supports the notion that Xpot-deficient mice exhibit systemic inflammation.

Regarding the proteomic analyses, despite a limited number of peptide reads, a notable observation is the generalized overexpression of ribosome components, from both the large and small subunits. Ribosome biogenesis is the most energy consuming anabolic

process in cells. Typically, cells exhibiting heightened rates of ribosome production are associated with elevated protein synthesis, a characteristic observed in cancer cells or embryonic stem cells [209,210]. These cells require rapid proliferation, leading to an increased demand for ribosomes. In our context, where no direct association with cancer was identified, it is plausible that a disruption in protein synthesis may induce compensatory mechanisms, leading the cell to augment ribosome production. This compensatory response would aim to maintain protein synthesis at a comparable rate in the presence of the hypothetical disruption.

To delve deeper into the effects induced by Xpot deficiency on aging and further explore the phenotype of haploinsufficient mice, we established two groups of animals, one consisting of young mice and the other of adult mice. Using these groups, we employed various approaches to investigate age-related differences. Metabolic studies carried out with the Oxymax apparatus, supported the notion that *Xpot* $^{-/-}$ mice exhibit metabolic alterations. During life, *Xpot*-null animals require increased oxygen consumption and carbon dioxide production, displaying a significantly higher energy expenditure than normal. These findings may be correlated with the observed increase in gluconeogenesis and the decrease in blood glucose and cholesterol levels. Surprisingly, the opposite occurs in haploinsuficient mice, who exhibit lower rates of oxygen consumption and carbon dioxide production, as well as significantly reduced energy expenditure through their lifespan, being this phenomenon observed in both young and adult mice. Intriguingly, the observed trend of opposite results between *Xpot*$^{-/-}$ and *Xpot*$^{+/-}$ is also evident in the flow cytometry analysis, suggesting again a different role of the protein when in haploinsufficiency.

Neuromotor function and strength are two parameters that normally decay with age. To assess that, rotarod tests and a forelimb grip strength test were performed in these two age-groups. By using a rotarod apparatus we were able to observe that *Xpot*$^{-/-}$ animals exhibit a worse coordination when they are young, which persists throughout their lives. Interestingly, heterozygous mice exhibit normal coordination, similar to that found in wild type mice, but when they age, it declines, a decrease that was not observed in control mice. This may suggest a reduction in coordination, which deteriorates with age in *Xpot*$^{+/-}$ mice, albeit not at the same rate as in wild type mice. On the other hand, assessing forelimb grip strength test we could not observe differences between mice. To obtain more solid results, the strength should had been normalized to the length of the animal's tibia. However, to achieve this, the mice would have had to be sacrificed, a step that was not taken due to the need for the continuation of experiments in these animals. Nevertheless, these data are presented to show that *Xpot*$^{-/-}$ do not exhibit obvious reductions in strength, as their weakness phenotype might suggest.

One of the most distinctive features of this new mouse model is the low birth rate observed in mice deficient in Xpot in homozygosity. The deviation from Mendelian ratios led us to consider that a disruption in some point of embryonic development was occurring. Therefore, we conducted a prenatal study in which we examined embryos at

different days of their development to pinpoint the stage at which the proportions of mice deficient in *Xpot* deviated from the expected values. Firstly, we decide to study embryos at day 12.5 post coitus. When we achieved a sufficient number of E12.5 embryos, we observed that at this stage of embryonic development, the percentage of embryos was not as normally expected. While in a normal development, we should have obtained 25% of mice deficient in the gene of interest in homozygosity, we only observed a 12.9% of them. Subsequently, we decide to study earlier stages of fetal development, and embryos at day 10.5 were examined. At this point, we could observe that the proportion of all genotypes was as expected according to Mendelian laws. This suggests that a key process occurring between the development stages E10.5 and E12.5 prevented *Xpot* null mice from developing. Examining their morphology, the most noticeable feature of *Xpot* deficient embryo is their small size when compared to their corresponding *Xpot* $^{+/+}$ and *Xpot*$^{+/-}$ littermates. Additionally, at day 12.5 post coitus it can be observed that *Xpot* $^{-/-}$ exhibit a fetal liver with a less pronounced red color compared to the strong red color present in wild-type mice. The same was observed with heart. Even though E10.5 fetal liver in wild type is not really notorious, same differences in color were found between *Xpot*$^{+/+}$ and *Xpot*$^{-/-}$ embryos. No differences in color or size were observed for these to organs between wild-type and *Xpot*$^{+/-}$ embryos.

Fetal liver exhibits a prominent red color in the embryo because it is a really important hematopoietic organ during embryogenesis. During fetal development, hematopoiesis occurs in multiple waves throughout the developing embryo and fetus, including extraembryonic yolk sac, the para-aortic region of the embryo, fetal liver, and placenta before eventually homing to the bone marrow where it occurs just before birth. The first hematopoiesis in mice embryo is observed in the yolk sac as early as E8, often referred to as primitive hematopoiesis, producing embryonic type erythroblasts and primitive type macrophages. The following waves consist of yolk sac and embryo-derived adult type hematopoiesis that produces erythro-myeloid progenitors and lymphoid precursors. Finally, the first bone marrow-repopulating HSCs are produced in the aorta-gonad-mesonephros region at E10-E11. These *de novo* HSCs seed the fetal liver and the placenta around E11-E12 and expand to support hematopoiesis after birth [211,212]. In the meantime, yolk sac-derived erythro-myeloid progenitors are considered to seed the liver as well to support hematopoietic homeostasis during embryo development. The fetal liver is the major hematopoietic organ during development, supporting active erythron-myeloid hematopoiesis and HSC expansion [213]. To gain a deeper insight into the hematopoietic activity of the fetal liver at E10.5 and E12.5, histopathological studies were conducted. H&E staining revealed a decrease in hematopoietic progenitor cells in *Xpot* deficient embryos at both E10.5 and E12.5. Among three *Xpot*$^{-/-}$ embryos studied at E10.5, one exhibited a limited number of hematopoietic cells in the fetal liver, difficult to appreciate, while the other two showed a significantly reduced number compared to the normal count in wild-type embryos. Fetal livers of all of them exhibited hypoplasia. Regarding the four E12.5 embryos studied, two had a normal-sized fetal liver, proportionate to the rest of the body, while the other two exhibited hypoplasia. Those with a smaller fetal liver size had a lower number of hematopoietic progenitor cells. The

remaining *Xpot*$^{-/-}$ embryonic structures at both stages appeared to have normal development, except for the ocular structures at E12.5 which lacked pigmentation when compared to the pigmentation present in wild type embryos.

Considering the transition between these two stages, E10.5 and E12.5, as a crucial checkpoint for fetal hematopoiesis development, and noting the decline in the percentage of *Xpot*-null embryos between these specific points, we can infer a significant role of Xpot in hematopoiesis during embryonic development. Furthermore, given the observed absence of anomalies in the morphology of the rest of embryonic structures, we can attribute the lower number of *Xpot*$^{-/-}$ at birth to disruptions in fetal hematopoiesis. Additionally, those embryos that manage to develop will likely exhibit, as observed in our flow cytometry studies, dysregulation in the production of various hematopoietic cells, supporting the notion of the key role of Xpot in the hematopoietic compartment.

Given *Xpot* significant overexpression in a variety of tumors, we postulated that its deficiency may potentially play a protective role against tumorigenesis. To explore this possibility and considering that lung cancer is a tumor where *XPOT* is frequently overexpressed, we decide to implement a chemical carcinogenesis protocol in these mice. Additionally, as we had observed the presence of loss-of-function mutations in patients with colorectal cancer, we also conducted a chemical carcinogenesis protocol to investigate whether *Xpot* deficiency could promote tumor development in the colon. The study was carried out in *Xpot*$^{+/-}$ and *Xpot*$^{+/+}$ mice, with *Xpot*$^{-/-}$ not being utilized due to the limited number of mice available and the severity of the protocols involved. No differences were found in the number or size of adenomas between *Xpot*$^{+/-}$ and *Xpot*$^{+/+}$ mice, making it impossible to establish a correlation between the Xpot mouse model and the development of lung and colorectal tumors.

The deficiency of Losp1 in *S. cerevisiae* causes an accumulation of end-processed intron-containing tRNAs [155] because, in budding yeast, the splicing machinery for tRNA is located on the outer surface of the mitochondria. However, the Los1-deficient yeast strain is viable and present a robustly extended lifespan. Despite the accumulation of tRNAs in the nucleus, they need to reach the cytoplasm for protein synthesis to occur. Therefore, other tRNA-binding transporter proteins, such as Xpo5 [122], Crm1 (Xpo1 in humans) or Mex67-Mtr2 (NXF1 in humans), have to come into play to facilitate the transport of tRNAs to the cytoplasm. Due to the lack of information regarding Xpot and tRNA transport in vertebrates, we decided to investigate the trafficking of tRNAs from the nucleus to the cytoplasm to determine whether our mouse model exhibited, like budding yeast, an accumulation of tRNAs in the nucleus. To undertake this approach, we not only examined the Xpot-null cells but also generated cells deficient in Xpo5 and Xpo1 to study their roles in tRNA trafficking in our model. We can distinguish two major groups of tRNAs based on their maturation process: those undergoing splicing mediated by the TSEN complex and the tRNA ligase, and those that do not. Due to the distinct affinities of exportins in budding yeast for tRNAs undergoing or not splicing, bearing in mind that Xpo5 in *S. cerevisiae* only binds to tRNAs without introns and Xpot shows no

affinity differences in this context, we aimed to study the transport of tRNAs undergoing splicing and those not undergoing it.

For this approach, fibroblasts were extracted from the three genotypes of our mouse model and subsequently immortalized using lentiviral expression vector pLOX-Ttag-ires-TK. Following cell extraction, we conducted a meticulous separation of the nucleus and cytoplasm using various detergents. After confirming the absence of cross-contamination, we proceeded to study various tRNAs through Northern blot with specific probes. No tRNA nucleus arrest was observed in mice fibroblast cells lacking Xpot, neither in haploinsufficiency nor in homozygosity, in contrast to what happens in *S. cerevisiae.* In addition, no apparent differences were observed in the quantity of tRNAs in the cytoplasm of *Xpot*$^{-/-}$ or *Xpot*$^{+/-}$ when compared to the wild type controls. This observation confirms that, despite the loss of the main tRNA transporter in our mouse model, the trafficking of tRNAs from the nucleus to the cytoplasm is not being affected, at least for the studied tRNAs. Interestingly, through the study of the group of tRNAs that undergo splicing, we observed tRNAs in the cytoplasmic fraction that still contained the intron, indicating that they were transported without undergoing splicing in the nucleus. This phenomenon was found in all three different genotypes and could shed light on investigations suggesting that tRNA splicing not only occurs in the nucleus but also in the cytoplasm. This is supported by studies that revealed the presence of TSEN complex and the tRNA ligase complex in the cytoplasm, challenging the general notion that splicing of non-coding RNAs only occurs in the nucleus [124].

These results could substantiate that indeed tRNAs are being transported to the cytoplasm through other exportins. Therefore, utilizing fibroblasts obtained from the murine model via the CRISPR/Cas9 system, we sought to generate double knockout mice for *Xpot* and *Xpo1*, *Xpot* and *Xpo5*, as well to obtain single knockout of *Xpo1* and *Xpo5* from wild type mice fibroblast. Unfortunately, we were unable to obtain mice deficient in *Xpo1*, most likely due to its crucial role in cell function as a transporter of numerous proteins and RNAs through the NPC [64]. Regarding *Xpo5* knockout, we could not achieve a complete reduction of the exportin in cells, but a significant decrease sufficient for conducting tRNA transport studies through Northern blot was attained. Through the study of the tyrosine-tRNA, differences in tRNA concentration were observed. Interestingly, when both exportins, Xpo5 and Xpot, are absent, there is a higher accumulation of pre-tRNAs in the nucleus. Additionally, there is a higher number of mature tRNAs in the nucleus and lower number in the cytoplasm. Altogether, this indicates that Xpo5, along with Xpot, transport tRNAs in the cells of our murine model. In summary, the data obtained from the tRNA transport profile study do not allow us to confirm that a disruption in tRNA trafficking is occurring in our mice model, even more in-depth study in this field is needed. Therefore, despite Xpot's only known function being the transport of tRNAs through NPC, we have not been able to demonstrate alterations in this process. This suggests possible new functions of XPOT, paving the way for further investigations in the future.

In summary, in this Doctoral Thesis, we have explored the significance of maintaining proper protein during the aging process and tumor development. Building upon previous studies in lower organisms, we generated two new murine models to focus our investigation. Considering the lifespan reduction observed in *C. elegans* due to deficiency in the proteostasis factor Aip1, the deficiency of its ortholog, AIRAPL, was previously studied in mice, positioning this protein as a key factor in the development to MPNs. As deficiency in its homologous protein AIRAP in mice seemed to lack relevance, we decided to study it in a context where both factors were deficient. This approach demonstrated that AIRAP also plays a crucial role in the generation of MPNs. Additionally, guided by evidence of increased lifespan in *S. cerevisiae* lacking the main tRNA transporter protein Losp1, we generated a new murine model deficient in its orthologous Xpot. However, we did not find similar results in terms of lifespan or tRNA transporting, which could be associated with the low homology between Losp1 and Xpot or the distinct context in which these proteins are studied, because the complexity of a murine model differs from that of yeast. Nonetheless, the generation of Xpot deficient mouse model has highlighted the importance of Xpot in the proper development of hematopoiesis, a fact that had not been observed before. We hope that our studies shed light on the important antineoplastic and geroprotective functions of protein homeostasis, serving as a foundation for future research and contributing further knowledge to the scientific community and to future medicine.

CONCLUSIONS

1. AIRAP deficiency alone does not produce any hematological phenotype.

2. Myeloproliferative transformation triggered by AIRAPL deficiency is enhanced by the absence of AIRAP.

3. *Xpot*$^{-/-}$ mice exhibit a reduced lifespan, whereas *Xpot*$^{+/-}$ animals have a similar lifespan to their wild type littermates.

4. *Xpot*$^{-/-}$ animals are born at a frequency ten-fold lower than the expected Mendelian ratio.

5. *Xpot*$^{-/-}$ mice present reduced body weight, increased energy expenditure, low cholesterol, and glucose blood levels.

6. *Xpot*-deficient mice exhibit elevated levels of most myeloid cells in the spleen, bone marrow and peripheral blood, and reduced numbers of B cells, indicating systemic inflammation that exposes a crucial role of XPOT in the hematopoietic compartment.

7. Loss of *Xpot*$^{-/-}$ embryos starts at E12.5 concurring with a crucial checkpoint for fetal hematopoiesis.

8. A link between *Xpot* deficiency and tRNA retention in cell nuclei has not been found, hindering the association of the tRNA subcellular localization with the phenotype of *Xpot*-deficient mice, and suggesting potential new XPOT functions.

CONCLUSIONES

1. La deficiencia de AIRAP por sí sola no produce ningún fenotipo hematológico.

2. La transformación mieloproliferativa desencadenada por la deficiencia de AIRAPL se ve potenciada por la ausencia de AIRAP.

3. Los ratones *Xpot*$^{-/-}$ presentan una esperanza de vida reducida, mientras que los animales *Xpot*$^{+/-}$ tienen una esperanza de vida similar a la de sus compañeros de camada wild type.

4. Los ratones *Xpot*$^{-/-}$ nacen con una frecuencia diez veces menor a la esperada según la proporción mendeliana.

5. Los ratones *Xpot*$^{-/-}$ tienen un peso corporal reducido, un aumento en el gasto energético y niveles bajos de colesterol y glucosa en sangre.

6. Los ratones deficientes en Xpot presentan niveles elevados de la mayoría de las células mieloides en el bazo, la médula ósea y la sangre periférica, además de una reducción en el número de células B, lo que indicaría presencia de inflamación sistémica y pone de manifiesto un papel crucial de XPOT en el compartimento hematopoyético.

7. La pérdida de embriones *Xpot*$^{-/-}$ comienza en E12.5 coincidiendo con un punto de control crucial para la hematopoyesis fetal

8. No se ha encontrado una conexión entre la deficiencia de *Xpot* y la retención de ARNts en los núcleos de las células, lo cual dificulta la asociación entre la localización subcelular de ARNts con el fenotipo de los ratones deficientes en *Xpot*, sugiriendo posibles nuevas funciones de XPOT.

BIBLIOGRAPHY

1. Bernard, C., Wolf, S. & Copley Greene, H. An Introduction to the Study of Experimental Medicine. in *Experimental Medicine* (2018). doi:10.4324/9781351320764-1

2. Cannon, W. B. *The wisdom of the body, 2nd ed. The wisdom of the body, 2nd ed.* (1939).

3. Davies, K. J. A. Adaptive homeostasis. *Molecular Aspects of Medicine* **49**, (2016).

4. Conti, A. A. Historical evolution of the concept of health in Western medicine. *Acta Biomed.* **89**, (2018).

5. World Health Organisation. Constitution of WHO: principles. *WHO* (2016).

6. López-Otín, C. & Kroemer, G. Hallmarks of Health. *Cell* **184**, (2021).

7. Hanahan, D. Hallmarks of Cancer: New Dimensions. *Cancer Discovery* **12**, (2022).

8. López-Otín, C., Blasco, M. A., Partridge, L., Serrano, M. & Kroemer, G. Hallmarks of aging: An expanding universe. *Cell* **186**, (2023).

9. Tyedmers, J., Mogk, A. & Bukau, B. Cellular strategies for controlling protein aggregation. *Nature Reviews Molecular Cell Biology* **11**, (2010).

10. Miles, J., Scherz-Shouval, R. & van Oosten-Hawle, P. Expanding the Organismal Proteostasis Network: Linking Systemic Stress Signaling with the Innate Immune Response. *Trends in Biochemical Sciences* **44**, (2019).

11. Van Oosten-Hawle, P., Porter, R. S. & Morimoto, R. I. Regulation of organismal proteostasis by transcellular chaperone signaling. *Cell* **153**, (2013).

12. Williams, K. W. *et al.* Xbp1s in pomc neurons connects ER stress with energy balance and glucose homeostasis. *Cell Metab.* **20**, (2014).

13. Feldman, D. E. & Frydman, J. Protein folding in vivo: The importance of molecular chaperones. *Current Opinion in Structural Biology* **10**, (2000).

14. Söti, C. & Csermely, P. Chaperones and aging: Role in neurodegeneration and in other civilizational diseases. *Neurochemistry International* **41**, (2002).

15. Walker, G. A. & Lithgow, G. J. Lifespan extension in C. elegans by a molecular chaperone dependent upon insulin-like signals. *Aging Cell* **2**, (2003).

16. Chen, X. Q. *et al.* Protein homeostasis in aging and cancer. *Frontiers in Cell and Developmental Biology* **11**, (2023).

17. Ciocca, D. R. & Calderwood, S. K. Heat shock proteins in cancer: Diagnostic, prognostic, predictive, and treatment implications. *Cell Stress and Chaperones* **10**, (2005).

18. Albakova, Z., Mangasarova, Y., Albakov, A. & Gorenkova, L. HSP70 and HSP90 in Cancer: Cytosolic, Endoplasmic Reticulum and Mitochondrial Chaperones of Tumorigenesis. *Frontiers in Oncology* **12**, (2022).

19. Mariño, G., Madeo, F. & Kroemer, G. Autophagy for tissue homeostasis and neuroprotection. *Current Opinion in Cell Biology* **23**, (2011).

20. Kaushik, S. & Cuervo, A. M. The coming of age of chaperone-mediated autophagy. *Nature Reviews Molecular Cell Biology* **19**, (2018).

21. Madeo, F., Zimmermann, A., Maiuri, M. C. & Kroemer, G. Essential role for autophagy in life span extension. *Journal of Clinical Investigation* **125**, (2015).

22. Levy, J. M. M., Towers, C. G. & Thorburn, A. Targeting autophagy in cancer. *Nature Reviews Cancer* **17**, (2017).

23. Gomes, L. R., Menck, C. F. M. & Cuervo, A. M. Chaperone-mediated autophagy prevents cellular transformation by regulating MYC proteasomal degradation. *Autophagy* **13**, (2017).

24. Meyer-Schwesinger, C. The ubiquitin–proteasome system in kidney physiology and disease. *Nature Reviews Nephrology* **15**, (2019).

25. Pickart, C. M. Mechanisms underlying ubiquitination. *Annual Review of Biochemistry* **70**, (2001).

26. Dong, Y. *et al.* Cryo-EM structures and dynamics of substrate-engaged human 26S proteasome. *Nature* **565**, (2019).

27. Collins, G. A. & Goldberg, A. L. The Logic of the 26S Proteasome. *Cell* **169**, (2017).

28. Xia, S. W. *et al.* Endoplasmic reticulum stress and protein degradation in chronic liver disease. *Pharmacological Research* **161**, (2020).

29. Kaushik, S. & Cuervo, A. M. Proteostasis and aging. *Nature Medicine* **21**, (2015).

30. Moreau, P. *et al.* Isatuximab, carfilzomib, and dexamethasone in relapsed multiple myeloma (IKEMA): a multicentre, open-label, randomised phase 3 trial. *Lancet* **397**, (2021).

31. Ito, S. Proteasome inhibitors for the treatment of multiple myeloma. *Cancers* **12**,

(2020).

32. Ren, J., Bi, Y., Sowers, J. R., Hetz, C. & Zhang, Y. Endoplasmic reticulum stress and unfolded protein response in cardiovascular diseases. *Nature Reviews Cardiology* **18**, (2021).

33. Lebeaupin, C. *et al.* Endoplasmic reticulum stress signalling and the pathogenesis of non-alcoholic fatty liver disease. *Journal of Hepatology* **69**, (2018).

34. Walter, P. & Ron, D. The unfolded protein response: From stress pathway to homeostatic regulation. *Science* **334**, (2011).

35. Liu, X. & Green, R. M. Endoplasmic reticulum stress and liver diseases. *Liver Research* **3**, (2019).

36. Hwang, J. & Qi, L. Quality Control in the Endoplasmic Reticulum: Crosstalk between ERAD and UPR pathways. *Trends in Biochemical Sciences* **43**, (2018).

37. Ron, D. & Walter, P. Signal integration in the endoplasmic reticulum unfolded protein response. *Nature Reviews Molecular Cell Biology* **8**, (2007).

38. Cubillos-Ruiz, J. R., Bettigole, S. E. & Glimcher, L. H. Tumorigenic and Immunosuppressive Effects of Endoplasmic Reticulum Stress in Cancer. *Cell* **168**, (2017).

39. Yun, C. *et al.* Proteasomal adaptation to environmental stress links resistance to proteotoxicity with longevity in Caenorhabditis elegans. *Proc. Natl. Acad. Sci. U. S. A.* **105**, (2008).

40. Sok, J. *et al.* Arsenite-inducible RNA-associated protein (AIRAP) protects cells from arsenite toxicity. *Cell Stress Chaperones* **6**, (2001).

41. Stanhill, A. *et al.* An Arsenite-Inducible 19S Regulatory Particle-Associated Protein Adapts Proteasomes to Proteotoxicity. *Mol. Cell* **23**, (2006).

42. Osorio, F. G. *et al.* Loss of the proteostasis factor AIRAPL causes myeloid transformation by deregulating IGF-1 signaling. *Nat. Med.* **22**, (2016).

43. Osorio, F. G., Freije, J. M. P. & López-Otín, C. The novel tumor suppressor AIRAPL regulates IGF1R proteostasis. *Cell Cycle* **15**, (2016).

44. Moran-Crusio, K., Reavie, L. B. & Aifantis, I. Regulation of hematopoietic stem cell fate by the ubiquitin proteasome system. *Trends in Immunology* **33**, (2012).

45. Rathinam, C., Thien, C. B. F., Langdon, W. Y., Gu, H. & Flavell, R. A. The E3 ubiquitin ligase c-Cbl restricts development and functions of hematopoietic stem cells. *Genes Dev.* **22**, (2008).

46. Mittelbrunn, M. & Kroemer, G. Hallmarks of T cell aging. *Nature Immunology* **22**, (2021).

47. Jerry L. Spivak, M. D. Myeloproliferative Neoplasms. *N. Engl. J. Med.* **376**, 2168–2181 (2017).

48. Thiele, J. *et al.* The international consensus classification of myeloid neoplasms and acute Leukemias: myeloproliferative neoplasms. *American Journal of Hematology* **98**, (2023).

49. Bahr, G. F. & Beermann, W. The fine structure of the nuclear membrane in the larval salivary gland and midgut of Chironomus. *Exp. Cell Res.* **6**, 519–522 (1954).

50. Watson, M. L. THE NUCLEAR ENVELOPE. *J. Biophys. Biochem. Cytol.* **1**, (1955).

51. Gay, S. & Foiani, M. Nuclear Envelope and Chromatin, Lock and Key of Genome Integrity. *Int. Rev. Cell Mol. Biol.* **317**, (2015).

52. Maeshima, K., Iino, H., Hihara, S. & Imamoto, N. Nuclear size, nuclear pore number and cell cycle. *Nucleus* **2**, (2011).

53. Schwartz, T. U. The Structure Inventory of the Nuclear Pore Complex. *Journal of Molecular Biology* **428**, (2016).

54. Beck, M. & Hurt, E. The nuclear pore complex: Understanding its function through structural insight. *Nature Reviews Molecular Cell Biology* **18**, (2017).

55. Schleicher, K. D. *et al.* Selective transport control on molecular velcro made from intrinsically disordered proteins. *Nat. Nanotechnol.* **9**, (2014).

56. Cho, K. I. *et al.* Loss of Ranbp2 in motoneurons causes disruption of nucleocytoplasmic and chemokine signaling, proteostasis of hnRNPH3 and Mmp28, and development of amyotrophic lateral sclerosis-like syndromes. *DMM Dis. Model. Mech.* **10**, (2017).

57. Cho, K. I., Searle, K., Webb, M., Yi, H. & Ferreira, P. A. Ranbp2 haploinsufficiency mediates distinct cellular and biochemical phenotypes in brain and retinal dopaminergic and glia cells elicited by the Parkinsonian neurotoxin, 1-methyl-4-phenyl-1,2,3,6-tetrahydropyridine (MPTP). *Cell. Mol. Life Sci.* **69**, (2012).

58. Sakuma, S. & D'Angelo, M. A. The roles of the nuclear pore complex in cellular dysfunction, aging and disease. *Seminars in Cell and Developmental Biology* **68**, (2017).

59. CALLAN, H. G. & TOMLIN, S. G. Experimental studies on amphibian oocyte nuclei. I. Investigation of the structure of the nuclear membrane by means of the electron microscope. *Proc. R. Soc. Lond. B. Biol. Sci.* **137**, (1950).

60. Franke, W. W. On the universality of nuclear pore complex structure. *Zeitschrift für Zellforsch. und Mikroskopische Anat.* **105**, (1970).

61. Raices, M. & D'Angelo, M. A. Nuclear pore complex composition: A new regulator of tissue-specific and developmental functions. *Nature Reviews Molecular Cell Biology* **13**, (2012).

62. Köhler, A. & Hurt, E. Exporting RNA from the nucleus to the cytoplasm. *Nature Reviews Molecular Cell Biology* **8**, (2007).

63. Mattaj, I. W. & Englmeier, L. Nucleocytoplasmic transport: The soluble phase. *Annual Review of Biochemistry* **67**, (1998).

64. Wing, C. E., Fung, H. Y. J. & Chook, Y. M. Karyopherin-mediated nucleocytoplasmic transport. *Nature Reviews Molecular Cell Biology* **23**, (2022).

65. O'Reilly, A. J., Dacks, J. B. & Field, M. C. Evolution of the karyopherin-β family of nucleocytoplasmic transport factors; ancient origins and continued specialization. *PLoS One* **6**, (2011).

66. Izaurralde, E., Kutay, U., Von Kobbe, C., Mattaj, L. W. & Görlich, D. The asymmetric distribution of the constituents of the Ran system is essential for transport into and out of the nucleus. *EMBO J.* **16**, (1997).

67. Görlich, D. & Kutay, U. Transport between the cell nucleus and the cytoplasm. *Annual Review of Cell and Developmental Biology* **15**, (1999).

68. Rexach, M. & Blobel, G. Protein import into nuclei: association and dissociation reactions involving transport substrate, transport factors, and nucleoporins. *Cell* **83**, (1995).

69. Matsuura, Y. Mechanistic Insights from Structural Analyses of Ran-GTPase-Driven Nuclear Export of Proteins and RNAs. *Journal of Molecular Biology* **428**, (2016).

70. Singh, G., Pratt, G., Yeo, G. W. & Moore, M. J. The clothes make the mRNA: Past and present trends in mRNP fashion. *Annual Review of Biochemistry* **84**, (2015).

71. Hieronymus, H. & Silver, P. A. Genome-wide analysis of RNA-protein interactions illustrates specificity of the mRNA export machinery. *Nat. Genet.* **33**, (2003).

72. Neville, M. & Rosbash, M. The NES-Crm1p export pathway is not a major mRNA export route in Saccharomyces cerevisiae. *EMBO J.* **18**, (1999).

73. Clouse, N. K., Luo, M. juan, Zhou, Z. & Reed, R. A Ran-independent pathway for export of spliced mRNA. *Nat. Cell Biol.* **3**, (2001).

74. Gallouzi, I. E. & Steitz, J. A. Delineation of mRNA export pathways by the use of cell-permeable peptides. *Science (80-.).* **294**, (2001).

75. Cullen, B. R. Nuclear mRNA export: Insights from virology. *Trends in Biochemical Sciences* **28**, (2003).

76. Azmi, A. S., Uddin, M. H. & Mohammad, R. M. The nuclear export protein XPO1 — from biology to targeted therapy. *Nature Reviews Clinical Oncology* **18**, (2021).

77. Delaleau, M. & Borden, K. L. B. Multiple export mechanisms for mRNAs. *Cells* **4**, (2015).

78. Segref, A. *et al.* Mex67p, a novel factor for nuclear mRNA export. Binds to both poly(A)+ RNA and nuclear pores. *EMBO J.* **16**, (1997).

79. Grüter, P. *et al.* TAP, the human homolog of Mex67p, mediates CTE-dependent RNA export from the nucleus. *Mol. Cell* **1**, (1998).

80. Pacheco-Fiallos, B. *et al.* mRNA recognition and packaging by the human transcription–export complex. *Nature* **616**, (2023).

81. Faza, M. B., Chang, Y., Occhipinti, L., Kemmler, S. & Panse, V. G. Role of Mex67-Mtr2 in the Nuclear Export of 40S Pre-Ribosomes. *PLoS Genet.* **8**, (2012).

82. Oeffinger, M., Dlakić, M. & Tollervey, D. A pre-ribosome-associated HEAT-repeat protein is required for export of both ribosomal subunits. *Genes Dev.* **18**, (2004).

83. Gadal, O. *et al.* Nuclear Export of 60S Ribosomal Subunits Depends on Xpo1p and Requires a Nuclear Export Sequence-Containing Factor, Nmd3p, That Associates with the Large Subunit Protein Rpl10p. *Mol. Cell. Biol.* **21**, (2001).

84. Karijolich, J. & Yu, Y. T. Spliceosomal snRNA modifications and their function. *RNA Biology* **7**, (2010).

85. Yong, J., Wan, L. & Dreyfuss, G. Why do cells need an assembly machine for RNA-protein complexes? *Trends in Cell Biology* **14**, (2004).

86. Fornerod, M., Ohno, M., Yoshida, M. & Mattaj, I. W. CRM1 is an export

receptor for leucine-rich nuclear export signals. *Cell* **90**, (1997).

87. Izaurralde, E. *et al.* A cap-binding protein complex mediating U snRNA export. *Nature* **376**, (1995).

88. Ohno, M., Segref, A., Bachi, A., Wilm, M. & Mattaj, I. W. PHAX, a mediator of U snRNA nuclear export whose activity is regulated by phosphorylation. *Cell* **101**, (2000).

89. Bartel, D. P. MicroRNAs: Genomics, Biogenesis, Mechanism, and Function. *Cell* **116**, (2004).

90. Kim, V. N. MicroRNA biogenesis: Coordinated cropping and dicing. *Nature Reviews Molecular Cell Biology* **6**, (2005).

91. Wu, K., He, J., Pu, W. & Peng, Y. The Role of Exportin-5 in MicroRNA Biogenesis and Cancer. *Genomics, Proteomics and Bioinformatics* **16**, (2018).

92. Li, J. *et al.* Pin1 impairs microRNA biogenesis by mediating conformation change of XPO5 in hepatocellular carcinoma. *Cell Death Differ.* **25**, (2018).

93. HOAGLAND, M. B., STEPHENSON, M. L., SCOTT, J. F., HECHT, L. I. & ZAMECNIK, P. C. A soluble ribonucleic acid intermediate in protein synthesis. *J. Biol. Chem.* **231**, (1958).

94. Holley, R. W. *et al.* Structure of a ribonucleic acid. *Science (80-.).* **147**, (1965).

95. Crick, F. H. C. Codon—anticodon pairing: The wobble hypothesis. *J. Mol. Biol.* **19**, (1966).

96. Chan, P. P. & Lowe, T. M. GtRNAdb 2.0: An expanded database of transfer RNA genes identified in complete and draft genomes. *Nucleic Acids Res.* **44**, (2016).

97. Orellana, E. A., Siegal, E. & Gregory, R. I. tRNA dysregulation and disease. *Nature Reviews Genetics* **23**, (2022).

98. Goodenbour, J. M. & Pan, T. Diversity of tRNA genes in eukaryotes. *Nucleic Acids Res.* **34**, (2006).

99. Jarrous, N. Roles of RNase P and Its Subunits. *Trends in Genetics* **33**, (2017).

100. Huang, Y., Intine, R. V., Mozlin, A., Hasson, S. & Maraia, R. J. Mutations in the RNA Polymerase III Subunit Rpc11p That Decrease RNA 3′ Cleavage Activity Increase 3′-Terminal Oligo(U) Length and La-Dependent tRNA Processing. *Mol. Cell. Biol.* **25**, (2005).

101. Weiner, A. M. tRNA maturation: RNA polymerization without a nucleic acid template. *Current Biology* **14**, (2004).

102. Lund, E. & Dahlberg, J. E. Proofreading and aminoacylation of tRNAs before export from the nucleus. *Science (80-.).* **282**, (1998).

103. Gerber, J. L., Köhler, S. & Peschek, J. Eukaryotic tRNA splicing-one goal, two strategies, many players. *Biological Chemistry* **403**, (2022).

104. Paushkin, S. V., Patel, M., Furia, B. S., Peltz, S. W. & Trotta, C. R. Identification of a human endonuclease complex reveals a link between tRNA splicing and pre-mRNA 3′ end formation. *Cell* **117**, (2004).

105. Popow, J. *et al.* HSPC117 is the essential subunit of a human tRNA splicing ligase complex. *Science (80-.).* **331**, (2011).

106. Sekulovski, S. *et al.* Assembly defects of human tRNA splicing endonuclease contribute to impaired pre-tRNA processing in pontocerebellar hypoplasia. *Nat. Commun.* **12**, (2021).

107. O'Donoghue, P. & Luthey-Schulten, Z. On the Evolution of Structure in Aminoacyl-tRNA Synthetases. *Microbiol. Mol. Biol. Rev.* **67**, (2003).

108. Boccaletto, P. *et al.* MODOMICS: A database of RNA modification pathways. 2021 update. *Nucleic Acids Res.* **50**, (2022).

109. Lorenz, C., Lünse, C. E. & Mörl, M. Trna modifications: Impact on structure and thermal adaptation. *Biomolecules* **7**, (2017).

110. Suzuki, T. The expanding world of tRNA modifications and their disease relevance. *Nature Reviews Molecular Cell Biology* **22**, (2021).

111. F. Anderson, J., Siller, E. & M. Barral, J. Disorders of Protein Biogenesis and Stability. *Protein Pept. Lett.* **18**, (2011).

112. Zasloff, M. tRNA transport from the nucleus in a eukaryotic cell: Carrier-mediated translocation process. *Proc. Natl. Acad. Sci. U. S. A.* **80**, (1983).

113. Arts, G. J., Fornerod, M. & Mattaj, I. W. Identification of a nuclear export receptor for tRNA. *Curr. Biol.* **8**, (1998).

114. Kutay, U. *et al.* Identification of a tRNA-specific nuclear export receptor. *Mol. Cell* **1**, (1998).

115. Kuersten, S., Arts, G.-J., Walther, T. C., Englmeier, L. & Mattaj, I. W. Steady-State Nuclear Localization of Exportin-t Involves RanGTP Binding and Two Distinct Nuclear Pore Complex Interaction Domains. *Mol. Cell. Biol.* **22**, (2002).

116. Rodriguez, M. S., Dargemont, C. & Stutz, F. Nuclear export of RNA. *Biology of the Cell* **96**, (2004).

117. Cook, A. G., Fukuhara, N., Jinek, M. & Conti, E. Structures of the tRNA export factor in the nuclear and cytosolic states. *Nature* **461**, (2009).

118. Wolin, S. L. & Matera, A. G. The trials and travels of tRNA. *Genes and Development* **13**, (1999).

119. Chatterjee, K., Marshall, W. A. & Hopper, A. K. Three tRNA nuclear exporters in S. cerevisiae: parallel pathways, preferences, and precision. *Nucleic Acids Res.* **50**, (2022).

120. Arts, G. J., Kuersten, S., Romby, P., Ehresmann, B. & Mattaj, I. W. The role of exportin-t in selective nuclear export of mature tRNAs. *EMBO J.* **17**, (1998).

121. Grosshans, H., Hurt, E. & Simos, G. An aminoacylation-dependent nuclear tRNA export pathway in yeast. *Genes Dev.* **14**, (2000).

122. Calado, A., Treichel, N., Müller, E. C., Otto, A. & Kutay, U. Exportin-5-mediated nuclear export of eukaryotic elongation factor 1A and tRNA. *EMBO J.* **21**, (2002).

123. Chen, M. *et al.* Nucleoporin TPR promotes tRNA nuclear export and protein synthesis in lung cancer cells. *PLoS Genet.* **17**, (2021).

124. Akiyama, Y., Lyons, S. M., Abe, T., Anderson, P. J. & Ivanov, P. Cytoplasmic processing of human transfer RNAs. *bioRxiv* (2022).

125. Bohnsack, M. T. *et al.* Exp5 exports eEF1A via tRNA from nuclei and synergizes with other transport pathways to confine translation to the cytoplasm. *EMBO J.* **21**, (2002).

126. Fu, S. C., Huang, H. C., Horton, P. & Juan, H. F. ValidNESs: A database of validated leucine-rich nuclear export signals. *Nucleic Acids Res.* **41**, (2013).

127. Okamura, M., Inose, H. & Masuda, S. RNA export through the NPC in eukaryotes. *Genes (Basel).* **6**, (2015).

128. Wu, J., Bao, A., Chatterjee, K., Wan, Y. & Hopper, A. K. Genome-wide screen uncovers novel pathways for tRNA processing and nuclear–cytoplasmic dynamics. *Genes Dev.* **29**, (2015).

129. Hopper, A. K., Pai, D. A. & Engelke, D. R. Cellular dynamics of tRNAs and their genes. *FEBS Letters* **584**, (2010).

130. Maraia, R. J., Mattijssen, S., Cruz-Gallardo, I. & Conte, M. R. The La and related

RNA-binding proteins (LARPs): structures, functions, and evolving perspectives. *Wiley Interdisciplinary Reviews: RNA* **8**, (2017).

131. Blewett, N. H. & Maraia, R. J. La involvement in tRNA and other RNA processing events including differences among yeast and other eukaryotes. *Biochimica et Biophysica Acta - Gene Regulatory Mechanisms* **1861**, (2018).

132. Chafe, S. C. & Mangroo, D. Scyl1 facilitates nuclear tRNA export in mammalian cells by acting at the nuclear pore complex. *Mol. Biol. Cell* **21**, (2010).

133. Frenkel-Morgenstern, M. *et al.* Genes adopt non-optimal codon usage to generate cell cycle-dependent oscillations in protein levels. *Mol. Syst. Biol.* **8**, (2012).

134. Gingold, H. *et al.* A dual program for translation regulation in cellular proliferation and differentiation. *Cell* **158**, (2014).

135. Torrent, M., Chalancon, G., De Groot, N. S., Wuster, A. & Madan Babu, M. Cells alter their tRNA abundance to selectively regulate protein synthesis during stress conditions. *Sci. Signal.* **11**, (2018).

136. Blanco, S. *et al.* Aberrant methylation of tRNAs links cellular stress to neuro-developmental disorders. *EMBO J.* **33**, 2020–2039 (2014).

137. Zhang, Z. *et al.* Global analysis of tRNA and translation factor expression reveals a dynamic landscape of translational regulation in human cancers. *Commun. Biol.* **1**, (2018).

138. Rapino, F. *et al.* Codon-specific translation reprogramming promotes resistance to targeted therapy. *Nature* **558**, (2018).

139. Pavon-Eternod, M. *et al.* tRNA over-expression in breast cancer and functional consequences. *Nucleic Acids Res.* **37**, (2009).

140. Richter, J. D. & Coller, J. Pausing on Polyribosomes: Make Way for Elongation in Translational Control. *Cell* **163**, (2015).

141. Pereira, M. *et al.* Impact of tRNA modifications and tRNA-modifying enzymes on proteostasis and human disease. *International Journal of Molecular Sciences* **19**, (2018).

142. Çağatay, T. & Chook, Y. M. Karyopherins in cancer. *Current Opinion in Cell Biology* **52**, (2018).

143. Jardin, F. *et al.* Recurrent mutations of the exportin 1 gene (XPO1) and their impact on selective inhibitor of nuclear export compounds sensitivity in primary mediastinal B-cell lymphoma. *Am. J. Hematol.* **91**, (2016).

144. Maracaja, D. L. V. *et al.* EBV-Positive Primary Large B-Cell Lymphoma: The Role of Immunohistochemistry and XPO1 in the Diagnosis of Mediastinal Lymphomas. *Appl. Immunohistochem. Mol. Morphol.* **28**, (2020).

145. Rai, K. R. & Jain, P. Chronic lymphocytic leukemia (CLL)-Then and now. *Am. J. Hematol.* **91**, (2016).

146. Wen, J. *et al.* Association of microRNA-related gene XPO5 rs11077 polymorphism with susceptibility to thyroid cancer. *Med. (United States)* **96**, (2017).

147. Osuch-Wojcikiewicz, E. *et al.* Association of Polymorphic Variants of miRNA Processing Genes with Larynx Cancer Risk in a Polish Population. *Biomed Res. Int.* **2015**, (2015).

148. Pan, L. J., Chen, J. L., Wu, Z. X. & Wu, Y. M. Exportin-T: A Novel Prognostic Predictor and Potential Therapeutic Target for Neuroblastoma. *Technol. Cancer Res. Treat.* **20**, (2021).

149. Lin, J. *et al.* Exportin-T promotes tumor proliferation and invasion in hepatocellular carcinoma. *Mol. Carcinog.* **58**, (2019).

150. Chen, L. *et al.* Prognostic roles of the transcriptional expression of exportins in hepatocellular carcinoma. *Biosci. Rep.* **39**, (2019).

151. Mehmood, R., Jibiki, K., Shibazaki, N. & Yasuhara, N. Molecular profiling of nucleocytoplasmic transport factor genes in breast cancer. *Heliyon* **7**, (2021).

152. Guo, C. *et al.* Comprehensive analysis of the functions and prognostic significance of RNA-binding proteins in bladder urothelial carcinoma. *Am. J. Transl. Res.* **12**, (2020).

153. Vaidyanathan, S., Thangavelu, P. U. & Duijf, P. H. G. Overexpression of Ran GTPase Components Regulating Nuclear Export, but not Mitotic Spindle Assembly, Marks Chromosome Instability and Poor Prognosis in Breast Cancer. *Target. Oncol.* **11**, (2016).

154. Melaiu, O. *et al.* Expression status of candidate genes in mesothelioma tissues and cell lines. *Mutat. Res. - Fundam. Mol. Mech. Mutagen.* **771**, (2015).

155. McCormick, M. A. *et al.* A Comprehensive Analysis of Replicative Lifespan in 4,698 Single-Gene Deletion Strains Uncovers Conserved Mechanisms of Aging. *Cell Metab.* **22**, (2015).

156. Sanjana, N. E., Shalem, O. & Zhang, F. Improved vectors and genome-wide libraries for CRISPR screening. *Nature Methods* **11**, (2014).

157. Suzuki, K., Bose, P., Leong-Quong, R. Y., Fujita, D. J. & Riabowol, K. REAP: A two minute cell fractionation method. *BMC Res. Notes* **3**, (2010).

158. Fraile, J. M., Campos-Iglesias, D., Rodríguez, F., Español, Y. & Freije, J. M. P. The deubiquitinase USP54 is overexpressed in colorectal cancer stem cells and promotes intestinal tumorigenesis. *Oncotarget* **7**, (2016).

159. Folgueras, A. R., Freitas-Rodríguez, S., Español, Y. & Velasco, G. Cancer susceptibility models in protease-deficient mice. in *Methods in Molecular Biology* **1731**, (2018).

160. Dobin, A. *et al.* STAR: Ultrafast universal RNA-seq aligner. *Bioinformatics* **29**, (2013).

161. Love, M. I., Huber, W. & Anders, S. Moderated estimation of fold change and dispersion for RNA-seq data with DESeq2. *Genome Biol.* **15**, (2014).

162. Korotkevich, G., Sukhov, V., Budin, N., Atryomov, M. N. & Sergushichev, A. Fast gene set enrichment analysis. bioRxiv. *bioRxiv* (2021).

163. López-Otín, C., Pietrocola, F., Roiz-Valle, D., Galluzzi, L. & Kroemer, G. Meta-hallmarks of aging and cancer. *Cell Metabolism* **35**, (2023).

164. Haas, S., Trumpp, A. & Milsom, M. D. Causes and Consequences of Hematopoietic Stem Cell Heterogeneity. *Cell Stem Cell* **22**, (2018).

165. Stone, A. P., Nascimento, T. F. & Barrachina, M. N. The bone marrow niche from the inside out: how megakaryocytes are shaped by and shape hematopoiesis. *Blood* **139**, (2022).

166. Yang, L. *et al.* Identification of Lin-Sca1+kit+CD34 +Flt3- short-term hematopoietic stem cells capable of rapidly reconstituting and rescuing myeloablated transplant recipients. *Blood* **105**, (2005).

167. Sommerkamp, P. *et al.* Mouse multipotent progenitor 5 cells are located at the interphase between hematopoietic stem and progenitor cells. *Blood* **137**, (2021).

168. Osorio, F. G. *et al.* Hutchinson-Gilford progeria: Splicing-directed therapy in a new mouse model of human accelerated aging. *Sci. Transl. Med.* **3**, (2011).

169. Santiago-Fernández, O. *et al.* Development of a CRISPR/Cas9-based therapy for Hutchinson–Gilford progeria syndrome. *Nat. Med.* **25**, (2019).

170. Koblan, L. W. *et al.* In vivo base editing rescues Hutchinson–Gilford progeria syndrome in mice. *Nature* **589**, (2021).

171. Skarnes, W. C. *et al.* A conditional knockout resource for the genome-wide study

of mouse gene function. *Nature* **474**, (2011).

172. Westcott, P. M. K. *et al.* The mutational landscapes of genetic and chemical models of Kras-driven lung cancer. *Nature* **517**, (2015).

173. Neufert, C., Becker, C. & Neurath, M. F. An inducible mouse model of colon carcinogenesis for the analysis of sporadic and inflammation-driven tumor progression. *Nat. Protoc.* **2**, (2007).

174. Chintalapati, C. *et al.* Protein RS1 (RSC1A1) downregulates the exocytotic pathway of glucose transporter SGLT1 at low intracellular glucose via inhibition of ornithine decarboxylase. *Mol. Pharmacol.* **90**, (2016).

175. Schäfer, N. *et al.* A modified tripeptide motif of RS1 (Rsc1a1) down-regulates exocytotic pathways of human Na1-D-glucose cotransporters SGLT1, SGLT2, and Glucose Sensor SGLT3 in the Presence of Glucose. *Mol. Pharmacol.* **95**, (2019).

176. Azzopardi, E., Lloyd, C., Teixeira, S. R., Conlan, R. S. & Whitaker, I. S. Clinical applications of amylase: Novel perspectives. *Surgery (United States)* **160**, (2016).

177. Ling, M. & Murali, M. Analysis of the Complement System in the Clinical Immunology Laboratory. *Clinics in Laboratory Medicine* **39**, (2019).

178. Hansson, G. C. Mucins and the Microbiome. *Annual Review of Biochemistry* **89**, (2020).

179. Basso, K. & Dalla-Favera, R. Roles of BCL6 in normal and transformed germinal center B cells. *Immunol. Rev.* **247**, (2012).

180. Cobaleda, C., Schebesta, A., Delogu, A. & Busslinger, M. Pax5: The guardian of B cell identity and function. *Nature Immunology* **8**, (2007).

181. Nurieva, R. I. *et al.* Bcl6 mediates the development of T follicular helper cells. *Science (80-.).* **325**, (2009).

182. Liu, D. *et al.* BCL6 controls contact-dependent help delivery during follicular T-B cell interactions. *Immunity* **54**, (2021).

183. Jia, L. *et al.* The roles of TNFAIP2 in cancers and infectious diseases. *Journal of Cellular and Molecular Medicine* **22**, (2018).

184. Bhowmik, K. K., Barek, M. A., Aziz, M. A. & Islam, M. S. Susceptibility of TNFAIP8, TNFAIP8L1, and TNFAIP2 Gene Polymorphisms on Cancer Risk: A Comprehensive Review and Meta-Analysis of Case–Control Studies. *Technol. Cancer Res. Treat.* **21**, (2022).

185. Guo, F. & Yuan, Y. Tumor necrosis factor alpha-induced proteins in malignant tumors: Progress and prospects. *OncoTargets and Therapy* **13**, (2020).

186. Adlanmerini, M. & Lazar, M. A. The REV-ERB Nuclear Receptors: Timekeepers for the Core Clock Period and Metabolism. *Endocrinology* **164**, (2023).

187. Li, M. D. *et al.* Circadian Clock-Controlled Checkpoints in the Pathogenesis of Complex Disease. *Frontiers in Genetics* **12**, (2021).

188. Ran, F. A. *et al.* Genome engineering using the CRISPR-Cas9 system. *Nat. Protoc.* **8**, (2013).

189. Duncan, W., Best, J., Golubitsky, M., Nijhout, H. F. & Reed, M. Homeostasis despite instability. *Math. Biosci.* **300**, (2018).

190. Ayres, J. S. The Biology of Physiological Health. *Cell* **181**, (2020).

191. Hoppe, T. & Cohen, E. Organismal protein homeostasis mechanisms. *Genetics* **215**, (2020).

192. Tsakiri, E. N. *et al.* Diet-derived advanced glycation end products or lipofuscin disrupts proteostasis and reduces life span in Drosophila melanogaster. *Free Radic. Biol. Med.* **65**, (2013).

193. Gordon, L. B., Rothman, F. G., López-Otín, C. & Misteli, T. Progeria: A paradigm for translational medicine. *Cell* **156**, (2014).

194. Shcherbakov, D. *et al.* Premature aging in mice with error-prone protein synthesis. *Sci. Adv.* **8**, (2022).

195. Bobkova, N. V. *et al.* Exogenous Hsp70 delays senescence and improves cognitive function in aging mice. *Proc. Natl. Acad. Sci. U. S. A.* **112**, (2015).

196. Munkácsy, E. *et al.* Neuronal-specific proteasome augmentation via Prosβ5 overexpression extends lifespan and reduces age-related cognitive decline. *Aging Cell* **18**, (2019).

197. Hance, M. W. *et al.* Secreted Hsp90 is a novel regulator of the epithelial to mesenchymal transition (EMT) in prostate cancer. *J. Biol. Chem.* **287**, (2012).

198. Li, X., He, S. & Ma, B. Autophagy and autophagy-related proteins in cancer. *Molecular Cancer* **19**, (2020).

199. Pohl, C. & Dikic, I. Cellular quality control by the ubiquitin-proteasome system and autophagy. *Science* **366**, (2019).

200. Kenyon, C. J. The genetics of ageing. *Nature* **464**, (2010).

201. Harrison, D. E. *et al.* Rapamycin fed late in life extends lifespan in genetically heterogeneous mice. *Nature* **460**, (2009).

202. Kaeberlein, M. *et al.* Cell biology: Regulation of yeast replicative life span by TOR and Sch9 response to nutrients. *Science (80-.).* **310**, (2005).

203. Kapahi, P. *et al.* Regulation of lifespan in Drosophila by modulation of genes in the TOR signaling pathway. *Curr. Biol.* **14**, (2004).

204. Hansen, M. *et al.* Lifespan extension by conditions that inhibit translation in Caenorhabditis elegans. *Aging Cell* **6**, (2007).

205. Syntichaki, P. & Tavernarakis, N. Signaling pathways regulating protein synthesis during ageing. *Exp. Gerontol.* **41**, (2006).

206. Zhang, X. *et al.* Mutation in Nuclear Pore Component NUP155 Leads to Atrial Fibrillation and Early Sudden Cardiac Death. *Cell* **135**, (2008).

207. Lupu, F., Alves, A., Anderson, K., Doye, V. & Lacy, E. Nuclear Pore Composition Regulates Neural Stem/Progenitor Cell Differentiation in the Mouse Embryo. *Dev. Cell* **14**, (2008).

208. Aslanukov, A. *et al.* RanBP2 modulates Cox11 and hexokinase I activities and haploinsufficiency of RanBP2 causes deficits in glucose metabolism. *PLoS Genet.* **2**, (2006).

209. Ni, C. & Buszczak, M. Ribosome biogenesis and function in development and disease. *Development (Cambridge)* **150**, (2023).

210. Pelletier, J., Thomas, G. & Volarevi, S. Ribosome biogenesis in cancer: New players and therapeutic avenues. *Nature Reviews Cancer* **18**, (2017).

211. Ema, H. & Nakauchi, H. Expansion of hematopoietic stem cells in the developing liver of a mouse embryo. *Blood* **95**, (2000).

212. Gekas, C., Dieterlen-Lièvre, F., Orkin, S. H. & Mikkola, H. K. A. The placenta is a niche for hematopoietic stem cells. *Dev. Cell* **8**, (2005).

213. Lewis, K., Yoshimoto, M. & Takebe, T. Fetal liver hematopoiesis: from development to delivery. *Stem Cell Research and Therapy* **12**, (2021).